Master thesis : CFD Modelling of Floating Offshore Wind Turbine Dynamics

CFD Modelling of Floating Offshore Wind Turbine Dynamics

Submitted on : January 28, 2022

By : Bharat Chandra Alla

Address : R.Filinto Elísio 21,1300-285 Lisbon, Portugal | bharatchandraalla@gmail.com

Student ID : S194104

Supervisors : MSc Manuel Rentschler & Dr. Guilherme Vaz

WavEC - Offshore Renewables, Lisbon, Portugal

Reviewers:

1. Prof RIGO Philippe, UNIVERSITY of LIEGE, ANAST, Quartier POLYTECH 1 Bat. B52/3, Allée de la Découverte 9, 4000 LIEGE, BELGIUM

2. Dr. Simone Saettone, Postdoctoral Research Associate, CEHINAV-ETSIN, Universidad Politécnica de Madrid, Spain.

3. Dr. Javier Calderón Sánchez, PhD Researcher, Graduate Teaching Assistant, CEHINAV-ETSIN, Universidad Politécnica de Madrid, Spain

ACKNOWLEDGEMENT

Contents

Declaration of Authorship

I declare that this thesis and the work presented in it are my own and have been generated by me as my original research.

Where I have consulted the published work of others, this is always clearly attributed.

Where I have quoted from the work of others, the source is always given. Except for such quotations, this thesis is entirely my work.

I have acknowledged all main sources of help.

Where the thesis is based on work done by myself jointly with others, I have clarified exactly what others did and what I have contributed to myself.

This thesis contains no material that has been submitted previously, in whole or in part, for the award of any other academic degree or diploma.

I cede copyright of the thesis in favor of the University of Liège and Polytechnic University of Madrid.

Date: January 28, 2022

Signature

ABSTRACT

In the far-shore environment, Floating Offshore Wind Turbines(FOWT) are subjected to the critical loading of wind, current, and waves. Current methodologies for describing the dynamics of fixed-bottom offshore turbines may be insufficient for accurately describing the dynamics of floating systems due to the combination of harsh environmental loads and large rotor & platform motions. The full description of FOWT dynamics is usually divided into three main parts: wind turbine aerodynamics, supporting platform hydrodynamics, and mooring system dynamics. This makes FOWT's design and analysis a technically difficult and computational problem. Due to the lack of computational power in the past, aerodynamic and hydrodynamic factors were frequently considered separately, potentially neglecting coupled effects.

The present study focuses on aerodynamic performance of the NREL 5MW wind turbine using high-fidelity viscous-flow CFD code ReFRESCO with the following objectives:

- Steady aerodynamic analysis of the turbine (blades only) with RANS turbulence models

- Unsteady Aerodynamic analysis of the turbine using sliding grid methodology

- Study of the flow around turbine in rotational motion

This work also involved thorough verification and validation against obtained numerical results over a wide range of Tip speed ratios(TSRs).

In addition, the current research work also involves advanced sensitivity studies for obtaining better results due to unsteady flow behaviour of the wind turbine. The sensitivity analysis are performed on domain studies, time-step studies, iterative convergence, Numerical uncertainty studies involving iterative error and discretization error, selection of turbulence model.

List of Figures

List of Tables

1 Introduction

The current section introduces the overview of wind turbine technology, and also this chapter is also divided into three sub-sections. In section 1.1 a situation analysis is given with the current scenario and developments of the floating wind technology. Section 1.2 and Section 1.3 deals with objectives and overview of the report.

1.1 Motivation

The world's biggest problem for people is energy scarcity. Nowadays, energy is being drawn from various sources such as coal, fossil fuels, and other renewable sources. There is a considerable gap since there are fewer coal resources, and new technology is indeed needed. So, it started Wind technology, i.e., extracting power from a wind turbine. From the last 20 years, there has been a usage of 300 GW wind power in the entire world[1]. Also, an increase of 22% can be seen in the production rate of wind power[1]. However, worldwide, it has a requirement of 72 TW wind power[1]. Although, most of the wind turbines are installed in onshore environments.

Already most of the wind turbines are placed on mountains and hilly areas. But this is not an optimized solution for the global energy transition. Since many problems persist from the turbines, noise propagation is not practical.

Offshore wind turbines replace this gap, and they also have some limitations concerning installation, transportation, manufacturing, marine location. Also, more wind turbines could be installed in the marine environment. In particular, Europe offshore has more number of offshore wind farms due to the reason that those areas are densely populated. Also, the offshore region has more very harsh marine environment. In these regions, the wind blows very fast, making less wear and producing more electricity. Compared to onshore and offshore wind turbines, the earlier ones are installed in remote places.

The blooming of an offshore wind project involves huge capital investment. At the same time, there are additional reasons like rough sea conditions, corrosion effects, fatigue problems, strong loads from waves, and the icing on turbine blades. This makes offshore construction very difficult.

Some offshore wind farms are already in possession, and the energy is being extracted

via high voltage substations placed in the marine environment(almost near). However, the installed wind turbines are of bottom-fixed and gravity-based foundations at not less than 50 meters, and new technology is needed to install wind turbines with more than 50 meters depth.

The new technology is derived from offshore oil rigs. The wind turbine is placed on a floating platform. Some floating platforms are Barge, Semi-submersible, Spar, and Tension-leg(TLP) as shown in the figure 1. Europe has huge potential to research new wind turbine technologies.

All the researchers came up with an idea to use existing deepwater technology. Then
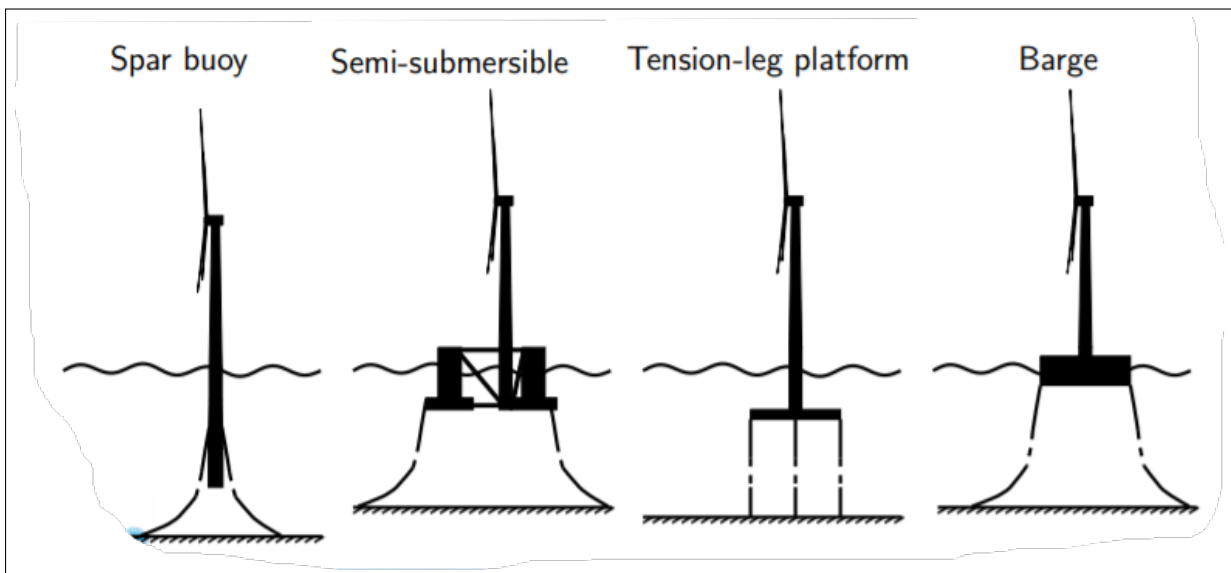
Figure 1: Floating Wind Concepts[2]

it came into existence, Floating offshore wind turbines a new era for the green energy transition. Each research institution came up with a unique floater design, and some of the innovative projects are Hywind [3], Goto-FOWT [4] and WindFloat at full-scale. While small-scale, a FOWT named VolturnUS has been developed by the University of Maine, an NREL 5MW wind turbine has been installed in the floater[5].

Some of the breakthroughs on floating offshore wind technology(FOWT) are given below:

- In December 2007, a TLP based FOWT was installed on the coast of Eastern Italy at a water depth of 115m. It transferred the wind & sea environment data to shore.

- In September 2009, a Spay buoy structure named Hywind was installed in offshore

Norway at 220 meters deep. This project was said to be the first in large capacity FOWT to be installed. The turbine has a total height of 120meters & each turbine has a capacity of 2.3MW. This wind turbine tried to withhold at harsh marine environments.

- In November 2011, a second FOWT was launched on the coast of Portugal. It is a semi-submersible type.

- In November 2013, Japan entered into developing its offshore wind farm at Fukushima. It is the semi-submersible type, and it is still in possession.

- In October 2017, a spar buoy FOWT type was installed on the coast of Scotland.

- In October 2017, a barge-type FOWT was installed on the coast of France.

- In July 2020, a 25MW wind farm was installed on the coast of Portugal containing three wind turbines. It is the semi-submersible type, and it supplies energy to 50,000 customers,

Although there are a lot of FOWT prototypes, this technology contains some limitations. The FOWT is a coupled system, i.e., aerodynamics response due to wind affects the motions of the hydrodynamics of the floating platform and vice versa. It needs an advanced study to study those coupled effects[2]. A research team is already formed with guidelines from the International Energy Agency(IEA), headed by National Renewable Energy Laboratory(NREL). Those tasks include the Offshore Code Comparison Collaboration (OC3) and the Offshore Code Comparison Collaboration, Continuation (OC4) projects[6]. The main aim of these two projects is to compare code-code dynamics responses of different offshore platforms.

Some of the tools are based on Blade-Element Momentum-Theory (BEMT), FAST(Fatigue, Aerodynamics, Structures, and Turbulence) code[7] is capable of finding dynamics response of wind turbines. But these tools consider its input only in 2D flow for prediction of 3D flow, and these codes are beneficial for initial calculations. Advanced computer resources are used to study the three-dimensional flow of the wind turbine, called High Performing Clusters(HPC). These clusters can perform calculations for Computational Fluid Dynamics(CFD) codes. The dynamics of a wind turbine includes:

- Aerodynamics

- Hydrodynamics

- Mooring systems

It is also visible in the figure 2 Wind turbines work at high loadings and those flows are
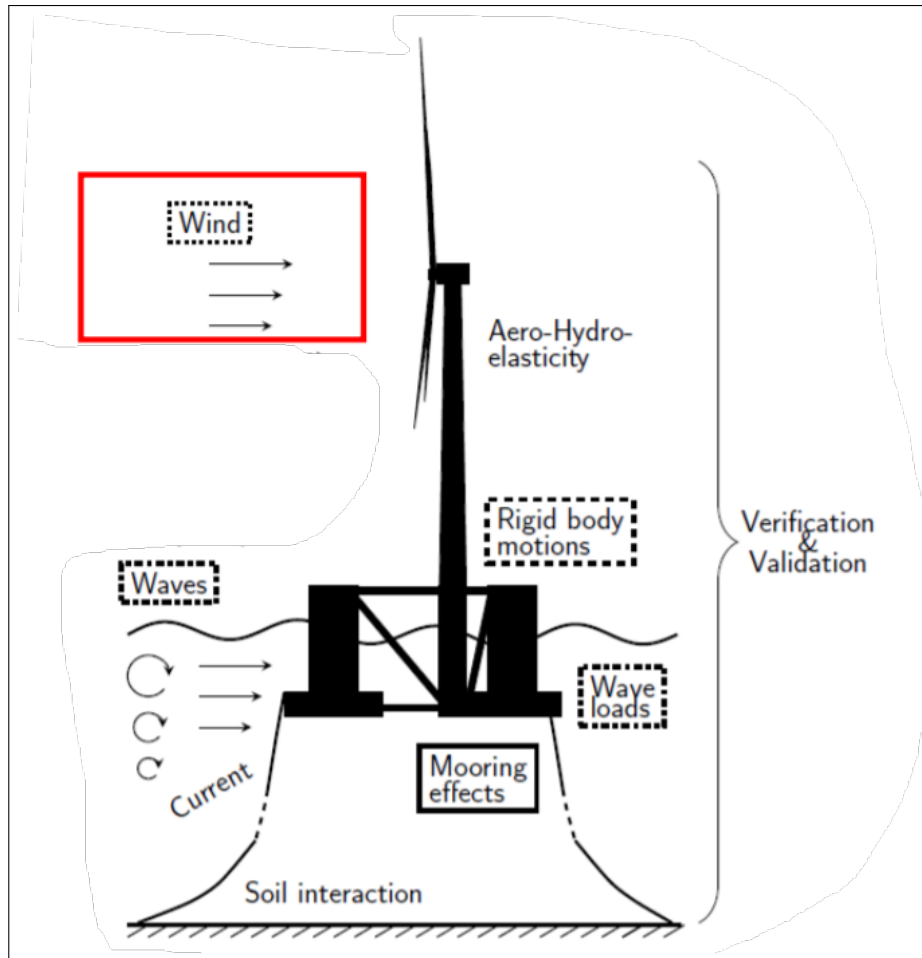
Figure 2: Wind Turbine Dynamics[8]

quite quasi rotating bi-dimensional (high AR). But similarities are established between propellers, current turbines and wind turbines. There are several super-tuned classical low-fidelity tools for wind turbine design and analysis. Therefore, the late application of CFD methods to these devices is a part of this work.

1.2   Objectives

This present work aims to perform numerical computations on non-floating turbines(rotor fixed) using a viscous flow code: *ReFRESCO*. The rotational motion of the turbine is imposed by the Absolute Formulation Method(AFM) and Sliding Grid methodology(SG).

Moreover, this research outcomes on performing CFD calculations for two different Wind Turbines at Model and Full-Scale.

1.3 Report Outline

The report is described as follows. The entire report is divided into ten chapters. The theoretical background required for the current study is discussed in chapter 2. The theory related to rotor blade, coordinate system, scaling methodology is explained. The flow characteristics of the wind turbine are explained in chapter 3. The governing laws for the motion of a fluid are explained in chapter 4. Detailed information about the software used in this work is discussed in 5. The setup required for performing numerical computations is detailly described in 6. Chapters 7 and 8 presents the final results of the thesis. Finally, the concluding remarks are discussed in chapter 9.

2 Theoretical Background

The theory associated with designing a wind turbine blade is described in this section. The rotor blade properties & reference system of the turbine is explained in 2.1 and 2.2.

2.1 Turbine Rotor Blade Geometry

NREL 5MW Baseline Wind Turbine: The NREL 5MW wind turbine is developed by NREL(US) is considered for this work. For detailed information and essential particulars of the wind turbine can be found in [9].

The model-scale experimental test is performed at MARIN. The Froude scaling is applied for the NREL 5MW wind turbine with a scaling parameter of $\lambda = 50$. The model-scale wind turbine blade geometry was described at [9, 10]. Also, the CAD model is generated using SolidWorks and Rhino 3D software.

2.2 Reference System

From the figure 3, the point of intersection of positive X, Y, Z-axis is stated as the origin of the reference system. Also, the turbine is rotated around x-axis(can be depicted in the figure 3), and in turn, wind velocity is opposite to it as shown from the exact figure. Similarly, the z-axis is considered as in vertical direction. The inflow speed and imposed rotational motion of the turbine are also depicted in the above figure by the vectors V_{inflow} and Ω.

2.3 Scaling Law

The experimental tests are based on Froude-scaling, and the scaling procedure is explained here[11, 12]. The dynamic marine environment needs to be studied before performing scaled experiments. The procedure adopted by MARIN is used for the current research work. An detailed information can be found in [11, 12].

2.3.1 Froude Similitude

The Froude number (Fr) is used to measure flow characteristics, and it is defined as the ratio of gravitational and inertial forces. The Froude number's main aim is to see how well a scaled model works with a full-scale or actual model. [13].
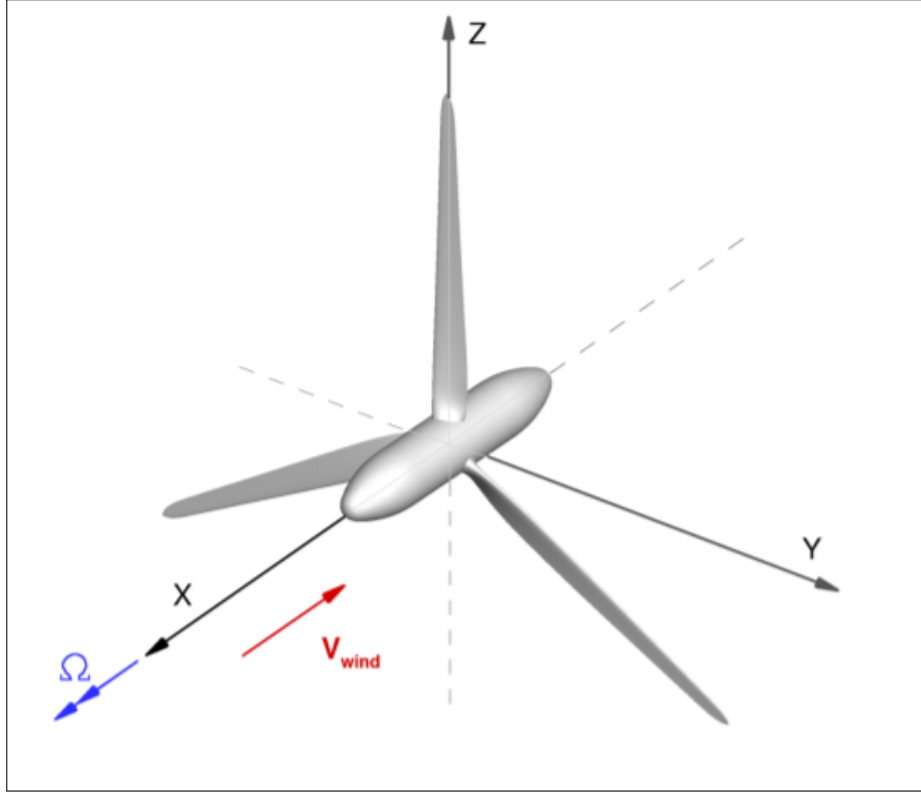
Figure 3: Reference system

It is given by the below equation (1)

$$Fr = \frac{V_o}{\sqrt{L_o g}} \tag{1}$$

Where V_o is the characteristic velocity, g the acceleration due to gravity, and L_o is the characteristic dimension,The relationship between model-scale and full-scale is given by,

$$\frac{V_m}{\sqrt{g L_m}} = \frac{V_p}{\sqrt{g L_p}}, \tag{2}$$

In the above equation, m and p denote model and prototype, respectively.

2.3.2 Tip Speed Ratio

It is the ratio of rotor speed and the inflow wind velocity [27]. It is given by,

$$TSR = \frac{\Omega R}{V} \tag{3}$$

where Ω is the angular velocity, R the blade tip radius of the rotor, and V the wind inflow velocity,

3   Wind Turbine Aerodynamics

3.1   Power Coefficient

The power and thrust coefficients, which are derived next, are a typical way to represent the performance characteristics of a wind turbine.

The differences in pressure across the disc cause a change in momentum and thereby resulting in net force, and it is represented by:

$$(P_d^+ - P_d^-)A_d = (U_\infty - U_w)\rho A_d U_\infty (1 - a) \tag{4}$$

where P_d^+ and P_d^- denote the upstream and downstream pressures at the actuator disc, the constant a is known as the axial-flow induction factor, inflow velocity U_∞, wake-field velocity U_w and A_d represents swept rotor's area.

The equation 4 gives the force created by the rotor on the air and the final power is given by .

$$\text{Power} = FU_d = U_\infty (1 - a) 2\rho A_d U_\infty^2 a (1 - a) \tag{5}$$

By dividing the above equation 5 by power available in stream flow gives the power can be made dimensionless, yielding the following expression:

$$C_P = \frac{Power}{\frac{1}{2}\rho A_d U_\infty^3} = \frac{2\rho A_d U_\infty^3 a (1 - a)^2}{\frac{1}{2}\rho A_d U_\infty^3} \tag{6}$$

Finally,

$$C_P = 4a(1 - a)^2 \tag{7}$$

The above equation 7 represents the fraction of power extracted from the wind is the power coefficient C_P

3.2 Thrust Coefficient

When the force in equation 4 is normalized by available thrust in the stream-line flow and it is obtained by the following expression:

$$C_T = \frac{Thrust}{\frac{1}{2}\rho A_d U_\infty^2} = \frac{2\rho A_d U_\infty^2 a(1-a)}{\frac{1}{2}\rho A_d U_\infty^2} \tag{8}$$

Finally,

$$C_T = 4a(1-a) \tag{9}$$

The C_T and C_P are the principal parameters defining the performance of a wind turbine which vary with the tip speed ratio(TSR) [10].

3.3 Beltz Limit

The highest value of C_P occurs when the following conditions are met:

$$\frac{dP}{da} = 4(1-a)^2 - 8a(1-a) = 0 \tag{10}$$

By solving. a can take the value of 0.333 and substituting the value of a into equation 7 will give the maximum achievable power coefficient,

$$C_{P_{max}} = 4.\frac{1}{3}(1-\frac{1}{3})^2 = \frac{16}{27} \approx 0.5926 \tag{11}$$

The is the most significant feasible power coefficient. No wind turbines have been designed to date that can reach this limit.

4 Governing Equations

This section will describe the viscous flow's theoretical assumptions and governing equations.

4.1 Navier-Stokes Equations

We consider the viscous turbulent flow around/inside an arbitrary hydrodynamic body, also have translational and rotational motions. A multi-phase flow approach is considered where the flow domain may consist of different fluids or species. A free surface may also exist between these fluids, and the flow's scalar properties (as temperature or species concentration) may also be essential to be tracked. The fluids are considered Newtonian, isothermal, and in-compressible.

For Cartesian coordinates and considering the space-fixed reference system the mass conservation equations and the momentum conservation equations can be written in differential form, for example,[14, 15],

$$\frac{\partial \rho}{\partial t} + \nabla \cdot (\rho \text{V}) = 0 \tag{12}$$

$$\frac{(\partial \rho \text{V})}{\partial t} + \nabla \cdot (\rho \text{VV}) = \nabla \cdot \text{T} + \rho \text{B} \tag{13}$$

B being a body-force vector, T being the stress tensor for a Newtonian fluid and D the deformation tensor defined by

$$\text{T} = \left(p + \frac{2}{3}\mu \nabla \cdot \text{V} \right) \text{I} + 2\mu \text{D} \tag{14}$$

$$\text{D} = \frac{1}{2} \left(\nabla \text{V} + \nabla \text{V}^T \right) \tag{15}$$

where I is the unit tensor. These are the Navier-Stokes equations which govern the fluid flow.

4.2 Reynolds-Averaged Navier-Stokes (RANS) Equations

The current model is designed to consider turbulent flows for the present work. But these flows are unsteady(time-dependent) in nature. In actual cases, most of the models are scaled by DNS(Direct Numerical Simulation). Another approach is said to be Reynolds Averaged Navier Stokes(RANS), reattaining the most relevant terms and modeling the turbulence effect by additional closure models, so-called turbulence model.

For most of the solutions, an average flow is considered. Here, the flow quantities are now divided into two components. They are time-averaged and fluctuating components (Reynolds decomposition). Those fluctuating components can be decomposed into Navier-Stokes equations(equations 12 and 13) to form Reynolds Averaged Navier Stokes(RANS) equations. The mass conservation equation can be represented as follows:

$$\nabla \cdot \overline{V} = 0, \quad \text{and,} \tag{16}$$

$$\nabla \cdot V' = 0 \tag{17}$$

At the same time equation 13 is written as.

$$\rho \frac{\partial \bar{V}_i}{\partial t} + \rho \frac{\partial \bar{V}_i \bar{V}_j}{\partial x_j} = \rho \bar{f}_i + \frac{\partial}{\partial x_j} \left[\bar{p} \delta_{ij} + \mu \left(\frac{\partial \bar{V}_i}{\partial x_j} + \frac{\partial \bar{V}_j}{\partial x_i} \right) - \rho \overline{V_i' V_j'} \right] \tag{18}$$

The above equation 18 is called as RANS equations and it contains an extra term $\rho \overline{V_i' V_j'}$ known as Reynolds Stresses [16, 17]. Here the indices i, $j = 1$, 2, 3 refer to the x, y, or z direction.

4.3 Unsteady Reynolds-Averaged Navier-Stokes (URANS) Equations

Unsteady flows are possible to be modelled with this approach, for instance when the unsteadiness comes from the flow pattern (vortex shedding, cavitation, etc) or even for some cases of imposed motions (roll-damping, Vortex-induced motion(VIM), Vortex-induced vibration(VIV))([18]). The three-dimensional velocity field is represented by the equation 19

$$u_i = \overline{u_i}(x, y, z, t) + u_i{'}(x, y, z, t) \tag{19}$$
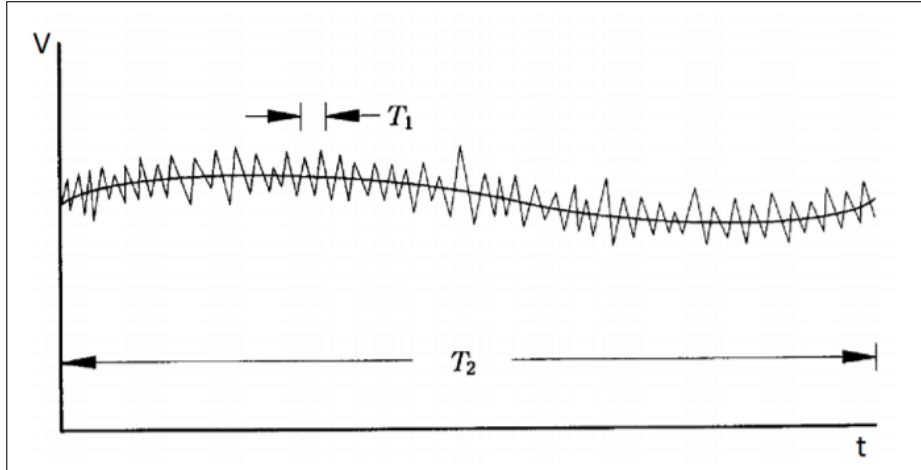
Figure 4: Time averaging[18]

From the figure 4, cyclic variation's time scale is unrelated.

4.4   Turbulence Modeling

The turbulence models are fundamental inflow modeling and in closure the problem. In the present work, 3 turbulence models are used. They are:

- Spalart-Allmaras model

- K - $\sqrt{KL}$ model

- K - ω shear stress model(2003)

The selection of turbulence model for the present work is based on the results and can be seen in section 7.3.

5   Numerical Background

This chapter presents the numerical tools used for the entire work. The basic idea of these tools is also described in this section. First, tools required for grid generation code $HEXPRESS$ followed by CFD code $ReFRESCO$ are explained. Finally, post-processing software for CFD results $PARAVIEW$ and $TEC360$ are used.

5.1   Hexpress

$HEXPRESS$ software [19] is used to generate grids for the present work. It is a fully un-structured hexahedral meshing with hex dominant mesh options for complex geometries. No matter how complicated, the code may handle any possible geometry. Refinements of superior quality may be created and get faster to two orders of magnitude quicker than any other software. The software is said to be user-friendly. $HEXPRESS$ takes lesser time to generate grids[20], and we decided to use this code for the present work.
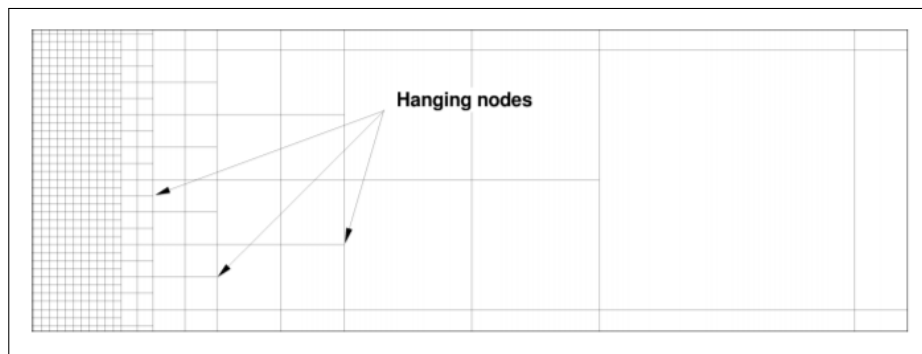
Figure 5: Hanging nodes

The only disadvantage is that the grid quality decreases, and this is the reason to refine the grid(which increases grid quality). From the figure 5, the grid generation code contains hanging nodes which are found at the boundary region located at the edges. The refinements are performed and depicted in the same figure in this region. Because of the increased geometric eccentricity, bad experiences with code are possible.

The CAD model is refined on the edges of the blade and also its surface. The quality characteristics can be checked within the code itself. The orthogonality and equi-angular skewness are two crucial parameters. The following expressions are used to calculate these

parameters in $HEXPRESS$,

$$\text{Equiangular skewness} = max\left(\frac{(T_{max} - T_e)}{180 - T_e}, \frac{(T_e - T_{min})}{T_e}\right), \tag{20}$$

$$\text{Orthogonality} = 90 - acos(min(\Gamma_{ijk})), \tag{21}$$

These parameters are used to predict grid's minimum orthogonality and maximum equiangular.

5.2   ReFRESCO

ReFRESCO is a in-house CFD solver for WaVEC that uses the RANS equations to solve multiphase (unsteady) incompressible flows in combination with turbulence models[21]. With cell-centered collocated variables, the equations are discretized using a finite-volume approach. The CFD features such as moving, sliding and deforming grids, as well automatic grid refinement are also available in the code.

5.3   Paraview

ParaView [22] is a multi-platform, open-source data visualization and analysis program. Users of ParaView may easily create visuals to examine data using qualitative and quantitative methods. Data exploration may be done in 3D interactively or programmatically utilizing ParaView's batch processing features.

Using distributed memory computing resources, ParaView was created to analyze large datasets. It has become a vital tool in many national laboratories, universities, and corporations and has received multiple honors connected to high-performance computation. It can be run on supercomputers to analyze datasets of petascale size and on laptops for relatively modest data.

5.4   Tec360

With integrated XY, 2D, and 3D charting, Tecplot 360[23] EX is a visual data analysis tool that enhances comprehension of computational fluid dynamic (CFD) outcomes and promotes productivity.

6 Numerical Setup

The entire chapter is divided into 2 sub-sections. The 1st sub-section deals with numerical modelling of fixed rotor position performing steady computations(Absolute-Formulation Approach) where as the 2nd sub-section deals with numerical modelling of Sliding Grid interfaces performing unsteady computations.(section 6.1 and 6.2 respectively.)

6.1 Absolute Formulation Approach

The numerical setup for rotor fixed position case performing steady computation describes:

- Rotor blade geometry

- Computational Domain

- Modelling of turbine motion(rotation)

- Boundary conditions

- Grid Network

- Steady computations overview

- Determining flow Characteristics(C_P & C_T)

The rotor blade geometry of the NREL 5MW Wind turbine is already discussed in section 2.1. As explained in the previous section, the model-scale experiments are performed at MARIN offshore basin testing as part of combined research with NREL, USA, without considering the hub for the wind turbine. For the numerical analysis, a new hub is designed as shown in the figure 6. The hub is intended to be a cylindrical shape containing spherical tangents on both ends. The objective of the hub is to decrease curvature variation, which in turn induces flow separation, and this phenomenon will be explained in the section 7.2.1.

6.1.1 Domain Dimensions

As shown in figure 7, the computational domain for rotor fixed position case performing steady calculations contains a cylinder(horizontal shape). In which the NREL 5MW wind turbine is placed. The turbine's position is located at the origin of the coordinate system(which is 1/5 the length of the cylinder).
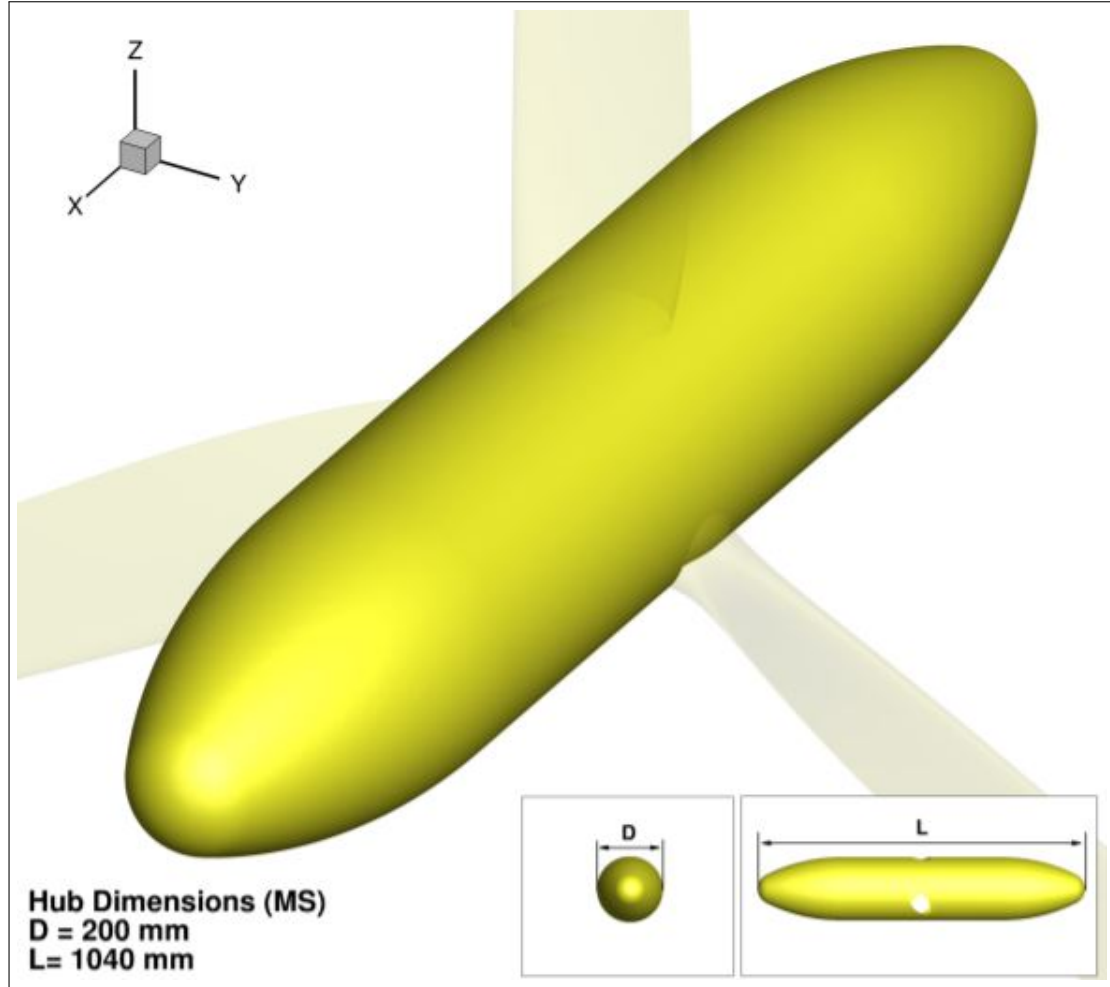
Figure 6: Overview of Hub.

6.1.2 Modelling of turbine motion

Let us consider the particle position in the absolute reference frame (X, Y, Z) as

$$X = x + x_0 \qquad (22)$$

where x_o being the origin of the relative reference frame (x, y, z). Also, the total derivative of the equation 22 gives, Velocity V on the absolute reference frame is then related to its counterpart on the relative reference frame by

$$V = U + \frac{dx_0}{dt} + \Omega \times x = U + V_g \qquad (23)$$
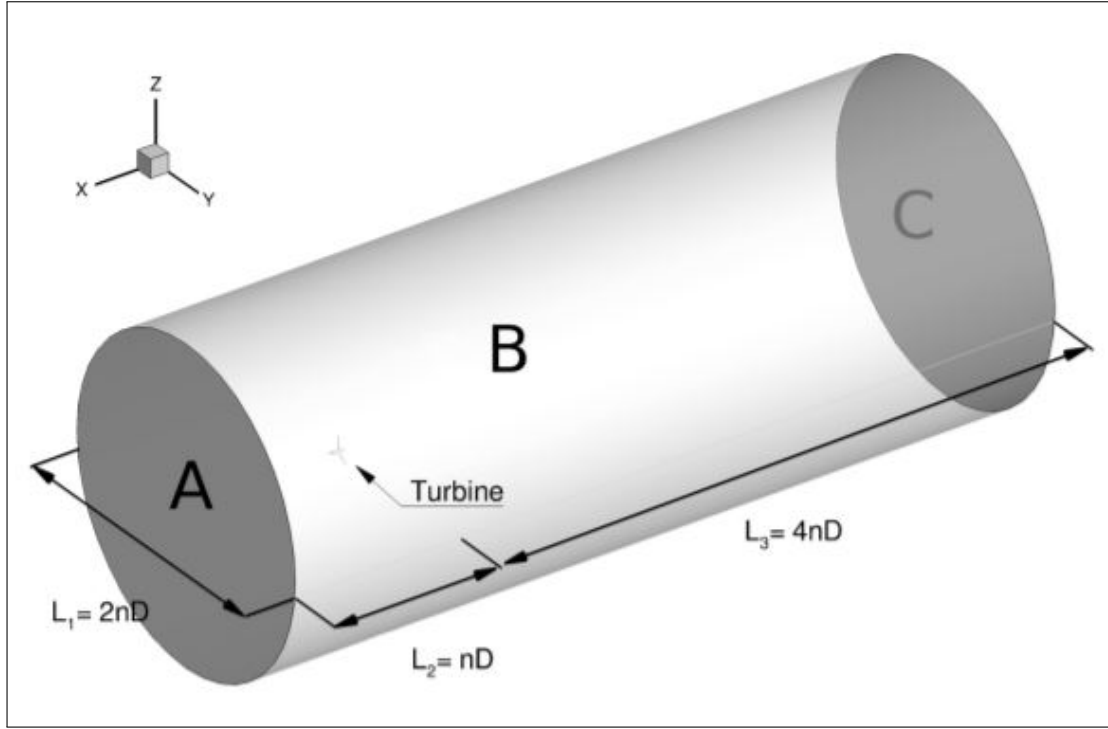
Figure 7: Three-Dimensional Domain(horizontal shaped).

where $\frac{dx_0}{dt}$ and Ω are, respectively, the translational and rotational velocity of the relative reference frame origin x_o. The total derivative of the equation 23 gives acceleration

$$\frac{DV}{Dt} = \frac{U}{Dt} + \frac{d^2 x_0}{dt} + \frac{d\Omega}{dt} \times x + 2\Omega \times U + \Omega \times (\Omega \times x), . \tag{24}$$

From the above equation 24, it can be understand that it contains four new additional terms which have to be into account

- $\frac{d^2 x_0}{dt}$ is the acceleration of the non-inertial reference frame origin.

- $\frac{d\Omega}{dt}$ is the angular acceleration effect.

- $2\Omega \times U$ is the Coriolis acceleration.

- $\Omega \times (\Omega \times x)$ is the centripetal acceleration, directed from the particle position normal rotational axes.

For modelling a general rigid-body motion (translation and/or rotation) of one object within RANS, the above approaches are possible: [24],

- Using special boundary-conditions, BC, whenever possible.

- Relative-Formulation (RFM) or body-forces-approach

- Absolute-Formulation (AFM)

- Moving-Grid-Formulation (MVG)

For the rotor fixed position performing steady computations, the Absolute Formulation Method(AFM) is adopted and the governing equations of mass conservation becomes,

$$\int_s (V - V_{x_0}) \cdot n dS = 0, \tag{25}$$

and the momentum equation,

$$\int_s \frac{\partial V}{\partial t} d\mathcal{V} + \int_s [\rho V(V - V_{x_0}) \cdot n] dS = \int_s (\nu + \nu_t)[(\nabla \mathcal{V} + \nabla \mathcal{V}^T)] \cdot dS + \cdots \tag{26}$$

$$- \int_\nu \nabla(p + \frac{2}{3}\rho k) d\mathcal{V} + \cdots \tag{27}$$

$$- \int_\nu \rho(\Omega \times V) d\mathcal{V} + \cdots \tag{28}$$

$$+ \int_\nu \rho B d\mathcal{V}, \tag{29}$$

One should make sure that $\int_s V_{x_0} \cdot n dS$ or $\nabla \cdot V_{x_0} = 0$, since we are only dealing by rigid-body motions. Boundary conditions may be defined both in body and earth-fixed reference system. An nonslip condition is to be enforced on the solid surface(rotor and hub), which is a coordinate line in the orthogonal body-fitted reference system., $V = V_{x_0}$ in the earth-fixed reference system or $U = 0$ in the body fixed. For detailed information [24]. From this assumptions, steady computations can be performed.

The relation of grid layout with AFM approach contains:

- Entire domain "rotates"

- Mostly cylindrical domains

- Cheaper computational costs

6.1.3 Boundary Conditions

For the steady state analysis, 4 boundary conditions are used. They are:

- BCWALL: Boundary wall condition applied at the surface of the turbine.

- BCINFLOW: Inflow velocity(wind) applied at domain inlet(A in figure 7)

- BCOUTFLOW: Neumann boundary conditions are applied(C in figure 7)

- BCPRESSURE: Pressure boundary condition(region B in figure 7)

The boundary conditions applied to the turbine can be shown in the figure 8
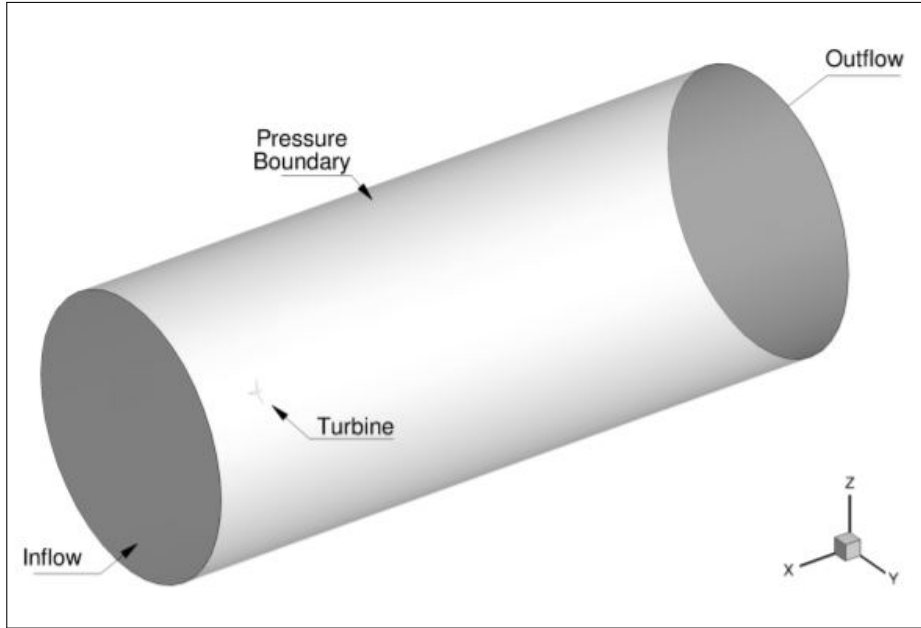
Figure 8: Boundary conditions for rotor fixed position case.

6.1.4 Grid Topology

As defined in the domain dimensions section, the size of each cell depends on the diameter of the turbine and then after the grid is refined until it reaches the required size on the surface of the rotor blade. The importance of refining the grid is to model the viscous layer inserted by the grid generation code $HEXPRESS$. The refinements are used at the whole surface of the rotor blade. The level of refinements, i.e., resolution on the surface, can be found by a parameter y^+, which is supposed to be less than 1. Also, $y^+ < 1$ means the viscous sublayer. From the earlier statement, the size of each cell(y^+) on the rotor parts is calculated by using the below formulation,

$$\Delta S = \frac{y^+ \mu}{\rho V_{fric}}. \tag{30}$$

Also, there exists an link between turbulence model and y^+. ΔS a stretching ratio, an input can be given to grid generation code for determining refinements. The refinements are added at Curvature areas like Leading Edge, Trailing Edge, Tip, Wake and Boundary Layer and the same can de depicted in the figure 9.
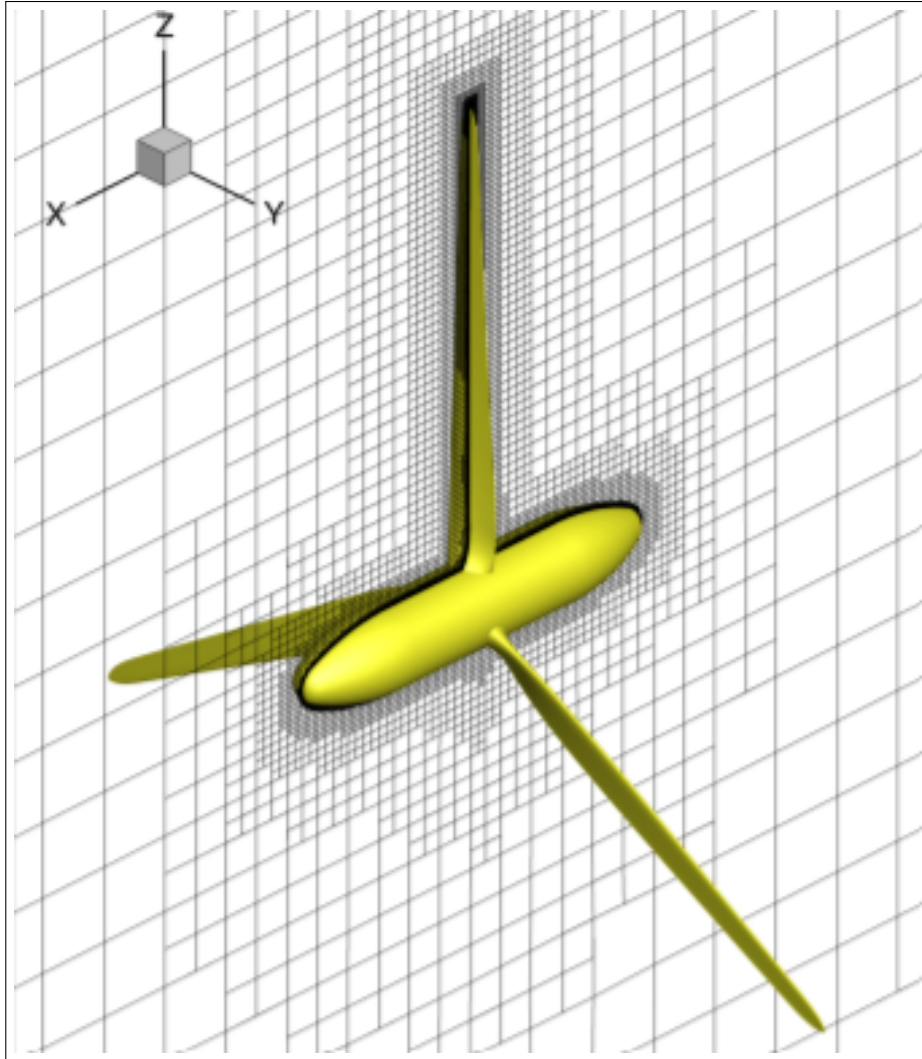
Figure 9: Refinements around wind turbine.

6.1.5   Steady Computations Overview

Table 1 describes the total calculations performed using Absolute Formulation Method.

6.1.6   Post-Processing

Velocity and pressure fields around the wind turbine obtained from the steady computations for rotor fixed position case could be visualized from the CFD data post-processing using software such as $PARAVIEW$ & $TEC360$. In this thesis work, $TEC360$ software is used extensively for visualizing the data, and the flow fields are explained in the section

7.3.

The above are the results of the three-dimensional steady computations(velocity and pressure-flow fields). In addition to these quantities, the objective of this thesis work is to calculate the thrust forces(F_x) and moments(M_x) acting on the rotor blade of the wind turbine. These quantities could determine the thrust(C_T) and power(C_P) coefficients of the turbine as follows:

$$C_T = \frac{F_x}{\frac{1}{2}\rho V^2 A}, \tag{31}$$

$$C_P = \frac{M_x \Omega}{\frac{1}{2}\rho V^3 A}, \tag{32}$$

where Ω is the angular velocity and A the rotor swept area of the turbine given by $A = \pi D^2/4$.

Table 1: Steady computations overview.

V_{inflow}(MS) $[m/s]$	V_{inflow}(FS) $[m/s]$	TSR [-]	Domain [-]	N_{cells}	Turbulence model
Size variation					
1.61	11.4	7	A	22.15	k - ω SST (2003)
			B	22.4	
			C	22.4	
Grids study					
1.61	11.4	7	C	14.1	k - ω SST (2003)
				19.2	
				25.9	
				31.6	
				35.4	
				51.9	
Turbulence modeling					
1.61	11.4	7	C	51.9	k - ω SST (2003)
				51.9	k - $\sqrt{KL}$ (SAS)
				51.9	Spalart-Allmaras (SA)
Calculations at different TSRs(MS)					
1.61	11.4	3	C	51.9	k - ω SST (2003)
		4		51.9	
		5		51.9	
		6		51.9	
		7		51.9	
		8		51.9	
Calculations at different TSRs(FS)					
1.61	11.4	3	C	46.6	k - ω SST (2003)
		4		46.6	
		5		46.6	
		6		46.6	
		7		46.6	
		8		46.6	

6.2 Sliding Grid Technology

In the previous section, the steady computations setup is explained. Here in this section a new methodology has been used to perform unsteady computations i.e., *Sliding grid interfaces.*

6.2.1 Domain Dimensions

Move-Grid Approach is selected, unlike the AFM approach used for steady computations discussed in the previous section. To perform unsteady computations. But a new way of generating CFD grids is adopted, which is the Sliding grid methodology(SG).

Sliding interfaces are considered non-conformal interfaces between two subgrids(static and dynamic), each having different motions. The static part larger domain(larger domain) and the active part(smaller domain, and it is in motion). The treatment of sliding interfaces is similar to for non-conformal interfaces, being the associated operations (interpolation, searching, and face values reconstruction) done more often. The quantities (face, cells, fluxes) at the different sides of these sliding interfaces have different values, some containing V_g related quantities (in a rotating domain, for instance), others not (in a non-rotating domain, for example).

The larger domain(length of the cylinder) has the same dimensions as the previous case, and it is shown in figure 10,

6.2.2 Modelling of turbine motion(Sliding Mesh Interfaces)

The turbine motion modeling for sliding-interfaces implementation needs different ingredients for imposing rotational motion. The three features that have been implemented in *ReFRESCO* are moving-grid (MVG) capability, non-conformal interfaces, special sliding-interfaces treatment.

In this study, the MVG formulation is used, and the RANS equations are rewritten as

$$\int_s (\mathrm{V} - \mathrm{V_{x_0}}) \cdot \mathrm{n} dS = 0, \tag{33}$$
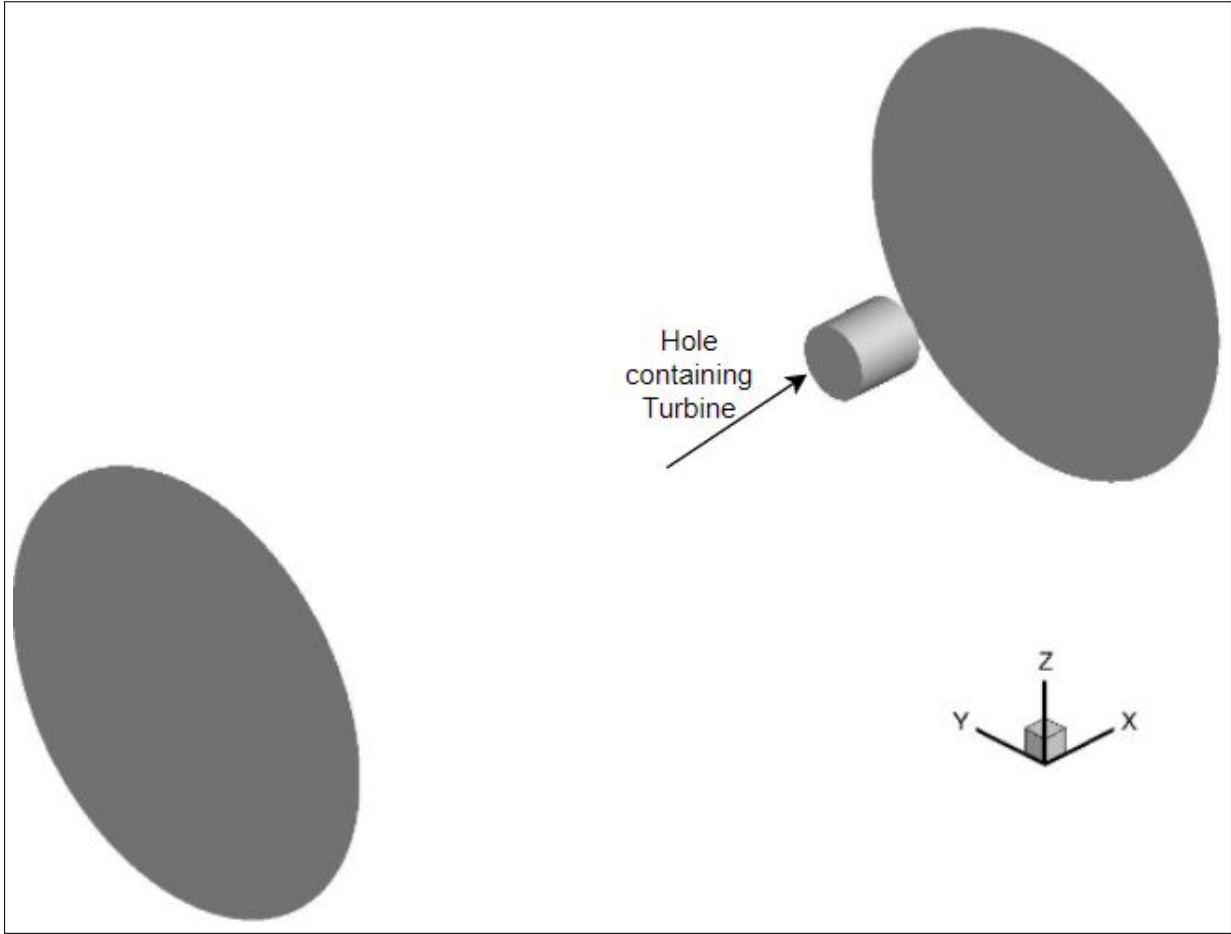
Figure 10: Sliding Grid setup.

and the momentum equation is with equation 25, Boundary conditions are always defined in the earth-fixed reference system. For instance for a `BCWALL` nonslip condition of a moving body, $V = V_{x_0}$. Equations and associated simulations are always unsteady due to the motion of the grid. The velocity field's initialization should also be done in the inertial earth-fixed reference frame.

The grid can be split into subgrids where each subgrid reference system origin (x_0, θ_0) may have a rigid-body motion defined by:

$$V_{x_0} = \frac{dx_0}{dt} + \Omega \times x \tag{34}$$

i.e. may have a translation motion with velocity $V_t = \frac{dx_0}{dt}$ and a rotation velocity $\Omega = \frac{d\theta_0}{dt}$. For each time-step the position of these subgrids has to be updated. The relation of grid layout with sliding grids contains:

- Only rotating parts "rotate"

- high practical

- Unsteady calculations and it requires more computational costs.

6.2.3 Boundary Conditions(Sliding Mesh Interfaces)

The boundary conditions `BCINFLOW`, `BCOUTFLOW` and `BCPRESSURE` are applied exactly like steady case for the static domain((see section 6.1.3).). But, for the cylindrical hole which is inside the larger domain takes a new boundary condition `BCINTERFACE` on the sliding interfaces. This new boundary condition mirrors the rotating domain(smaller domain) and non-rotating domain(larger domain).

Table 2: Unsteady computations overview.

V_{inflow}(MS) $[m/s]$	V_{inflow}(FS) $[m/s]$	TSR [-]	Domain [-]	N_{cells}	Turbulence model
Grids study					
1.61	11.4	7	C + Subgrid	14.1 19.2 25.9	k - ω SST (2003)
Calculations at different TSRs(MS)					
1.61	11.4	3 4 5 6 7 8	C + Subgrid	51.9	k - ω SST (2003)
Calculations at different TSRs(FS)					
1.61	11.4	3 4 5 6 7 8	C + Subgrid	46.6	k - ω SST (2003)

6.2.4   Unsteady Calculation Overview

Table 2 describes the total calculations performed using Move-Grid Approach(Sliding grid methodology)

7 Numerical Study on NREL 5MW Wind Turbine at Model-Scale(without imposed motion)

This is the most important section of the present work, and it is divided into four sections. The numerical results for the rotor fixed position performing steady simulations on the NREL 5MW Wind turbine will be discussed. In section 7.1, the selection of domain size is explained. Section 7.2 is dedicated to performing advanced studies on verification of the simulations. Section 7.3 deals with studies on finalizing turbulence models. In section, 7.4 the NREL 5MW Wind Turbine model-scale computations are validated against numerical results.

7.1 Domain Size Variation

The size of the Domain plays a key role in the flow analysis, and also it could dominate the solution. It is very much important to ensure the domination of the solution to be negligible to obtain accurate flow data for the NREL 5MW Wind Turbine geometry. To do so, a number of computations with different computational domain size are performed (see section 6.1).

The flow condition for all the simulations performed and obtained in this present work is given below in the table 3.

Table 3: Flow condition for entire work.

TSR	7
$V_{inflow}(model-scale)$	1.61 m/s
$V_{inflow}(full-scale)$	11.4 m/s

For the selection of domain size, three domains are considered with different dimensions, namely A, B, and C, and they are represented in table 4

Table 4: Domain overview.

Identifier	Upstream Length: nD	Wake Length: nD	Radius: nD
Domain **A**	5	20	10
Domain **B**	10	40	20
Domain **C**	15	60	30

The numerical computations are performed for domains A, B & C for the same flow condition to finalize the domain size. Now, the normalized velocity fields for the three

domains are extracted from the post-processing software $TEC360$, and they can be depicted from the figures 11, 12 and 13. In $TEC360$ software, there is an inbuilt option called "$Blanking$" where one could blank inflow velocities. The normalized velocity fields are obtained by dividing Velocity field by axial velocity(In X-direction, i.e., V_{inflow}). From the figures 11, 12 and 13, the blanked regions can be visualized.

In comparison between all the normalized velocity plots, the axial flow of Domain A reaches the boundaries. At the same time, this phenomenon cannot be depicted for domains B & C(see figures 12 and 13). Since the effected flow region is decelerated less than 0.1% of the $V_{inflow} = 1.61 \ m/s$ near external boundaries, the influence on its solution is considered to be negligible. In the normalized velocity field of domain B, an issue with the grid is seen, i.e., the flow is not smooth in the axial direction. This is due to the domain size and numerical uncertainty of the grid generated by the Hexpress tool. Also, looking at the dimensions; Domain A is said to be smaller than Domain B & Domain C.
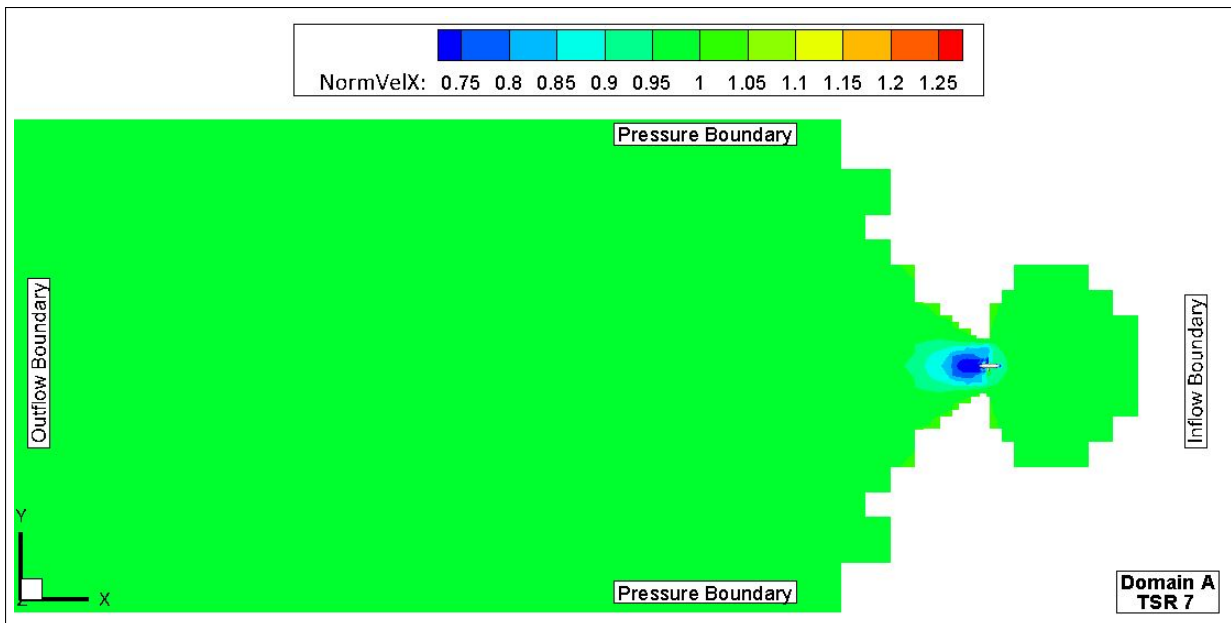
Figure 11: Plot of Normalized velocity field for Domain **A**
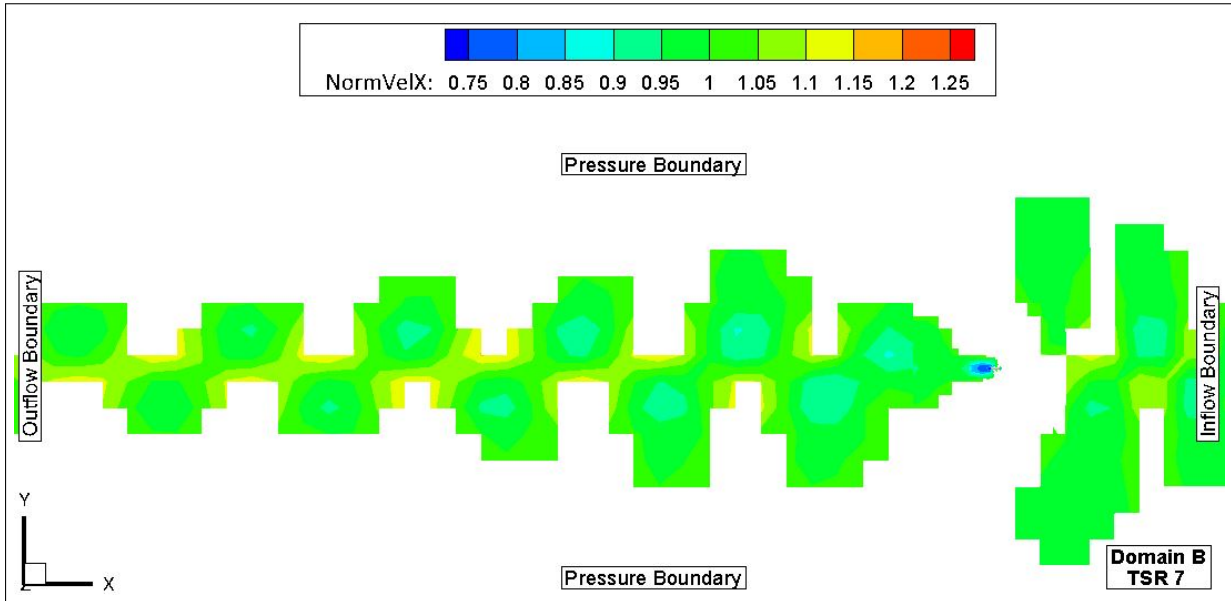
Figure 12: Plot of Normalized velocity field for Domain **B**
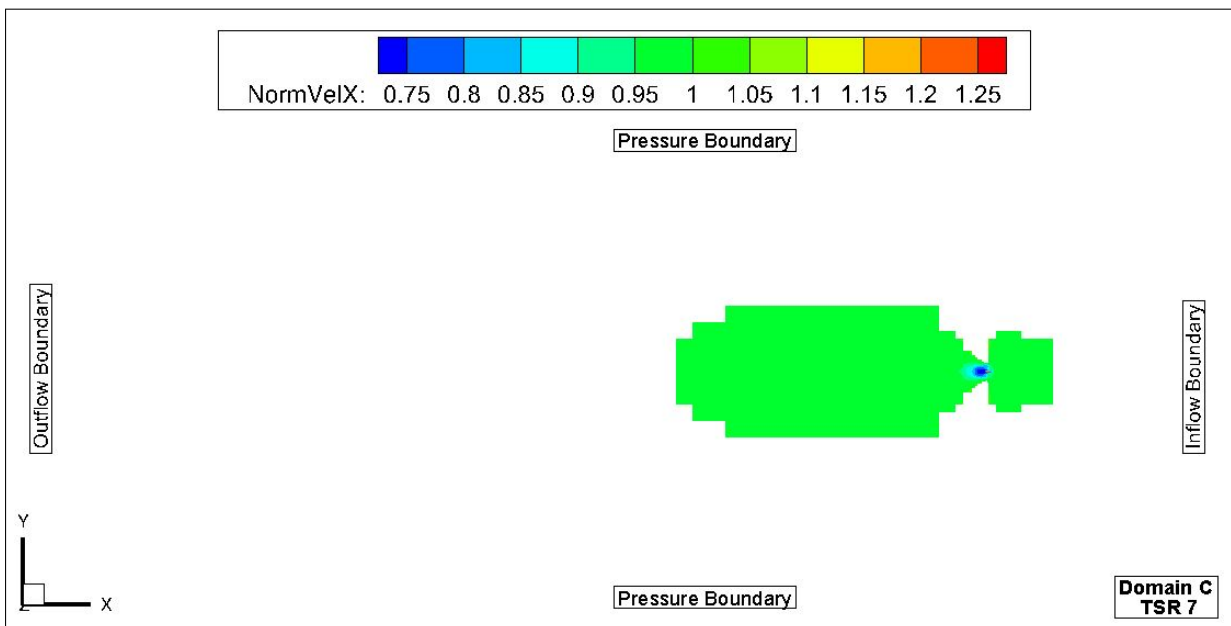
Figure 13: Plot of Normalized velocity field for Domain **C**

The flow characteristics are presented in table 5 and the same can be depicted in figure 14. Although, an increasing trend is found in C_T, whereas a decreasing trend is found in C_P.

Also, the differences in C_T and C_P are presented relative to the largest Domain (C) are shown in the figure 15. Also, the maximum difference is found to be 2.2% for C_T and 2.5% for C_P, and the same came can be predicted in the figure 16. For the rest of the project work, the size of **Domain C** will be used.

Table 5: Thrust and Power coefficients.

Identifier	$C_T[-]$	[%]	$C_P[-]$	[%]
Domain **A**	0.3995	2.2	0.1463	2.5
Domain **B**	0.4076	0.22	0.1533	0.4
Domain **C**	0.4085	-	0.1427	-
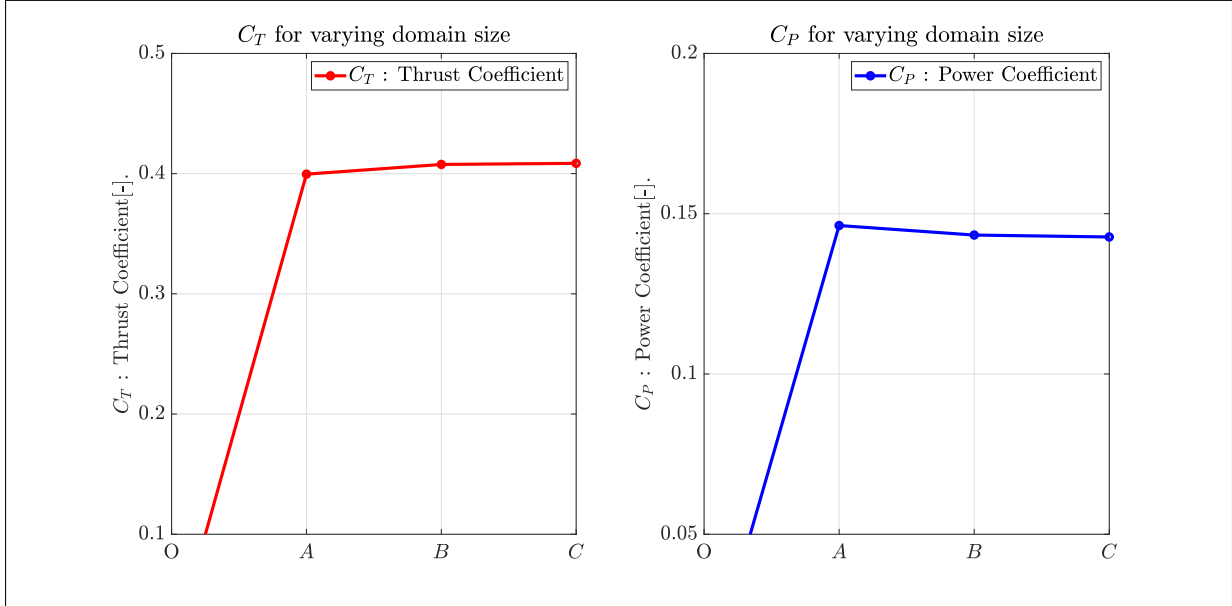
Figure 14: Thrust(in left) and Power(in right) coefficients.
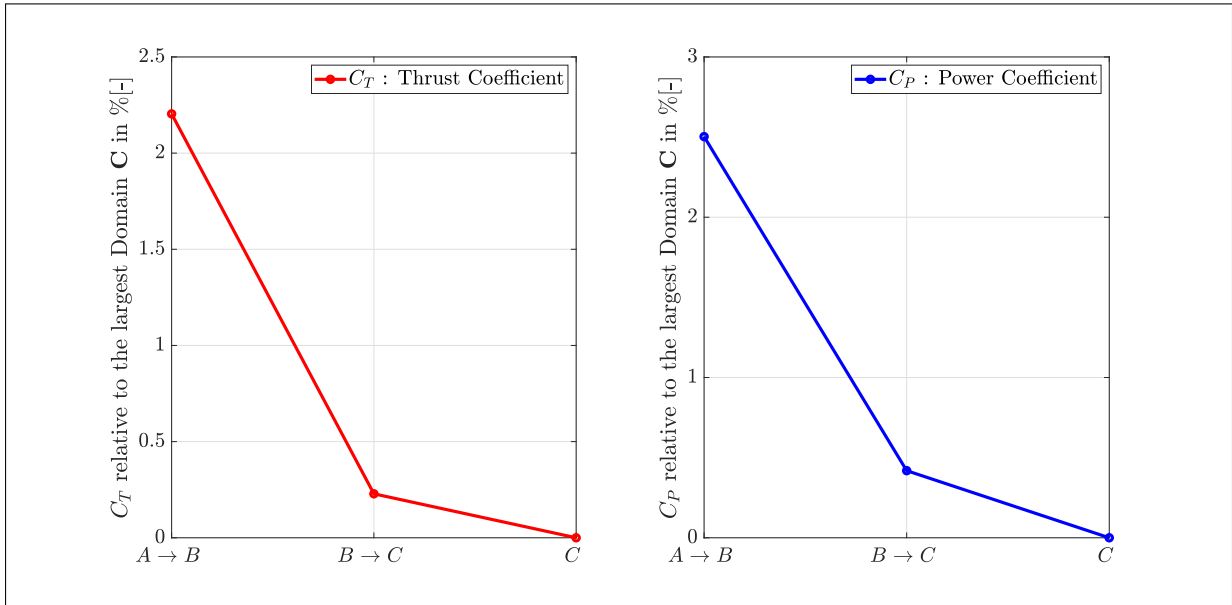
Figure 15: Relative difference with respect to Domain C in percentage.
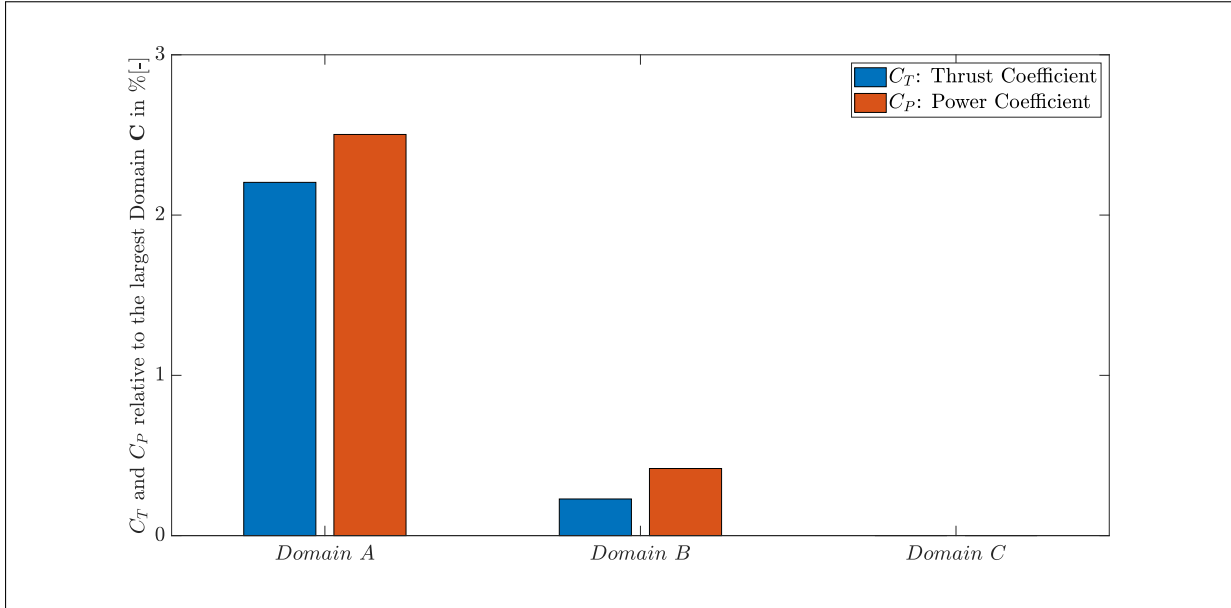
Figure 16: Relative difference with respect to Domain C in percentage

7.2   Numerical Uncertainty Study

A total of 6 grids with several cells varying between 14.06M to 51.8M are analyzed to estimate the uncertainty initiated from numerical errors for the performed numerical computations. Table 6 shows the properties of the grids. The grids are generated to keep as geometric a similarity as possible.

Table 6: Refinement study

Grid Refinement	1	2	3	4	5	6
Total no.of Cells	14068097	19222832	25835054	31569288	35401787	51881535
Min Orthogonality	10.421	13.567	15.492	12.58	11.723	11.56
Avg Orthogonality	77.89	78.194	78.43	78.156	77.88	78.32
Max Skewness	0.905	0.867	0.878	0.861	0.852	0.893
Grid ref. ratio	1.54	1.39	1.26	1.18	1.14	1.00

7.2.1   Iterative Error

The iterative error associated within these computations is explained in this section. These type of errors are occurred due to difference between converged solution and not fully converged solution for a given number of finite grid points. The maximum L_2- and L_∞-norm residuals for all the 6 grids are shown in tables 7 & 8 and they are at the range of 10^{-5} & 10^{-2} respectively. For this present case, the numerical computations are run for 6000 iterations and the same can be depicted in tables 7 & 8.

Table 7: Maximum L_2 Residuals

Grid no	Grid ref. $\frac{h_i}{h_1}$	n_{iter}	L_2 **Residuals** Max(u,v,w,p)
1	1.54	6000	$3.266 \cdot 10^{-5}$
2	1.39	6000	$4.131 \cdot 10^{-5}$
3	1.26	6000	$5.464 \cdot 10^{-5}$
4	1.18	6000	$7.832 \cdot 10^{-5}$
5	1.14	6000	$2.114 \cdot 10^{-4}$
6	**1.00**	**6000**	$\mathbf{2.77 \cdot 10^{-5}}$

Table 8: Maximum L_∞ Residuals

Grid no	Grid ref. $\frac{h_i}{h_1}$	n_{iter}	L_∞ **Residuals** Max(u,v,w,p)
1	1.54	6000	$4.20 \cdot 10^{-2}$
2	1.39	6000	$4.96 \cdot 10^{-2}$
3	1.26	6000	$9.36 \cdot 10^{-2}$
4	1.18	6000	$8.58 \cdot 10^{-2}$
5	1.14	6000	$3.66 \cdot 10^{-2}$
6	**1.00**	**6000**	$\mathbf{3.36 \cdot 10^{-2}}$
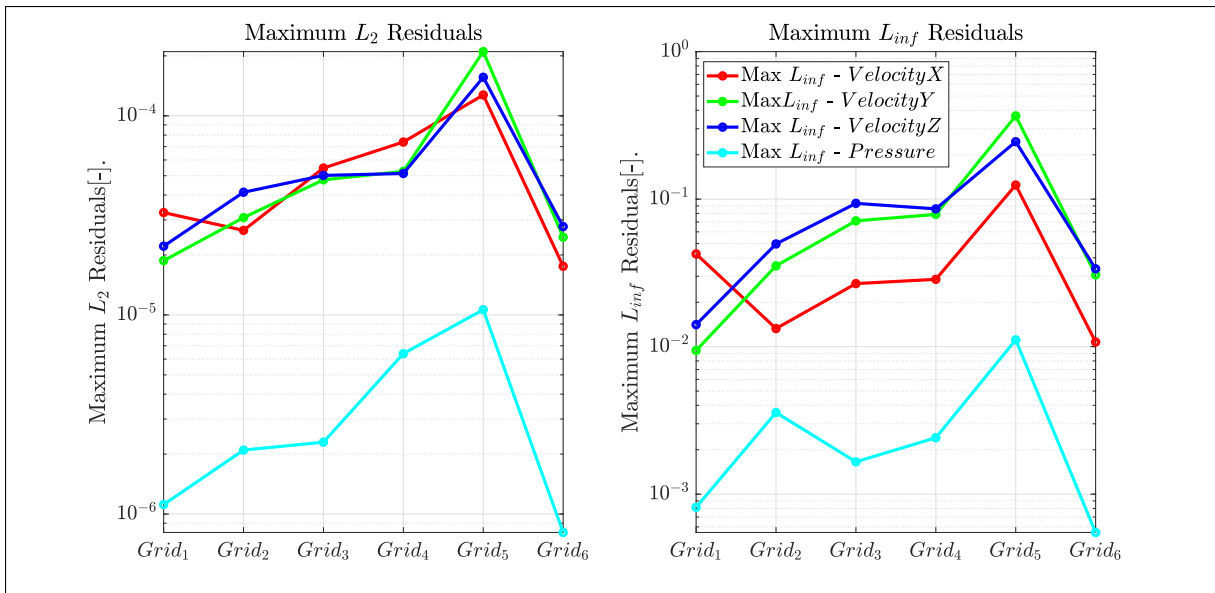
Figure 17: Maximum L_2 and L_∞-norms of the residuals for grid no.6.

The figures 18, 19 and 20 represents the convergence plots for L_2-norms residuals, Thrust coefficient(C_T) and Pressure coefficient(C_P) for grid no. 6(refined grid). These plots are very much useful for estimating errors against number of iterations(6000 in this case).
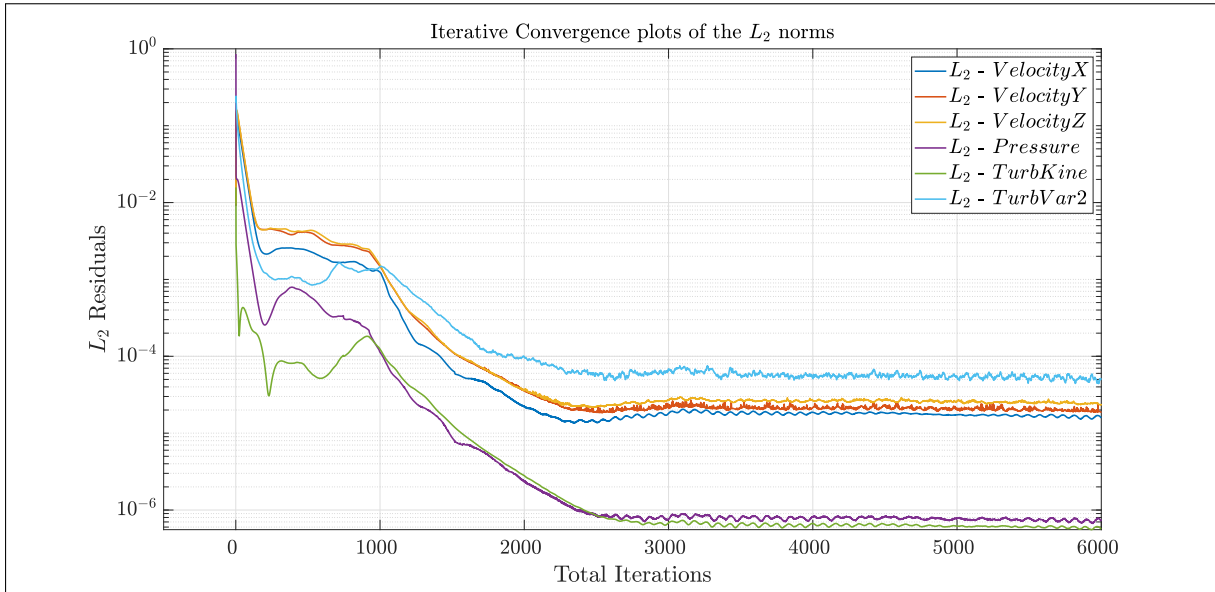
Figure 18: Plot of monitoring residuals of flow quantities at each iteration.
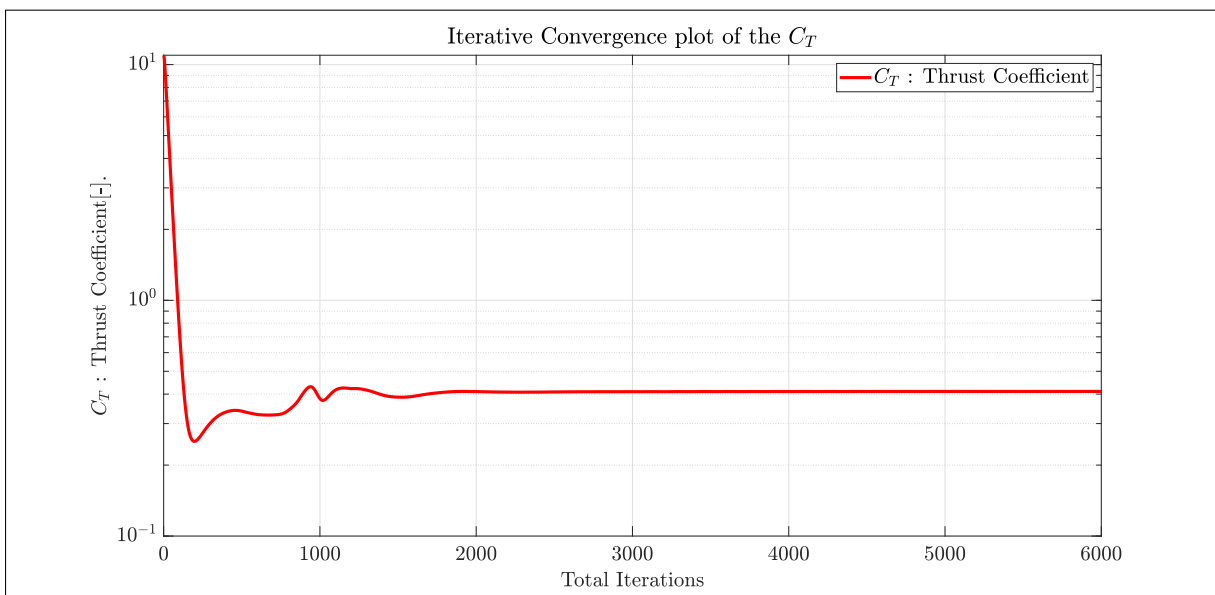
Figure 19: Plot of monitoring magnitude of thrust coefficient at each iteration.

Since the maximum residuals are already found in the previous studies and can be depicted in tables 7 and 8, those values can be used as input for plotting in the flow domain. When looking at the flow domain in the 21, those strict residuals are because of inconsistent behavior, and the same can be observed near the blade root obtained from the iso-surfaces of the Q-factor 22. The main reason for the flow to be unsteady is due to the shape of the hub, and the same phenomenon can be found in [25].

The maximum difference of C_T between two grids has reached 0.05 % for the finer grid, and it is depicted in the figure 23 and whereas for the maximum difference of C_P between
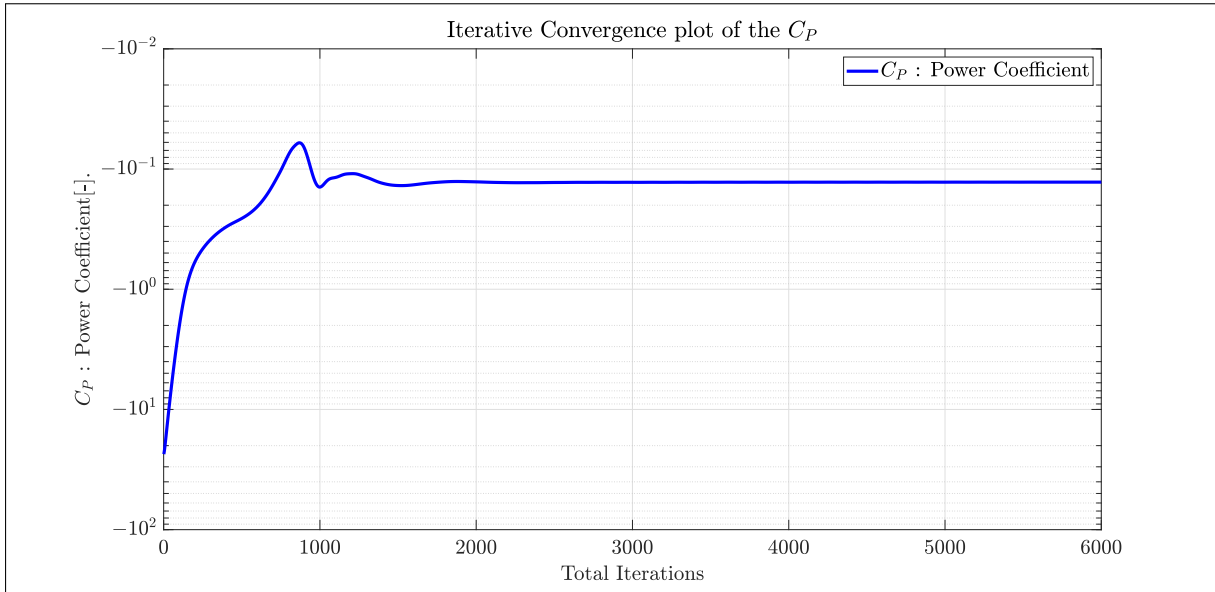
Figure 20: Plot of monitoring magnitude of power coefficient at each iteration.
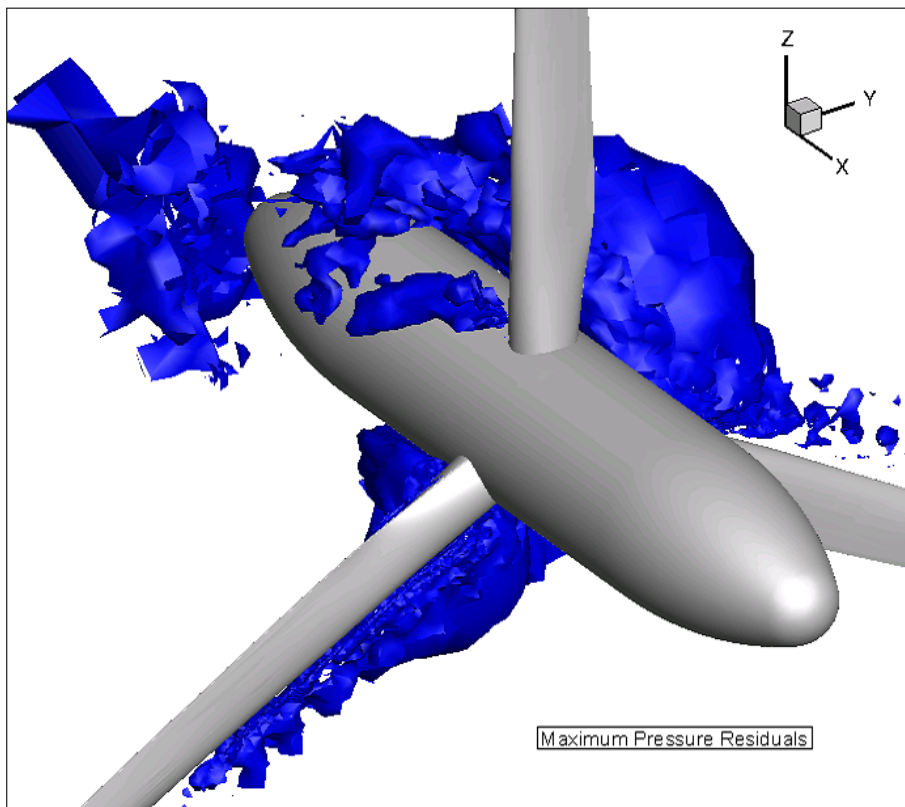
Figure 21: Identifying residuals.

two grids has reached 5 % and it is depicted in the figure 24. Here, a sudden increase in indifference is seen for C_P, which is due to the bad quality of grid no. 5 results in more significant differences.

A sensitivity analysis is performed for both Thrust coefficient(C_T) and Power coefficient(C_P),
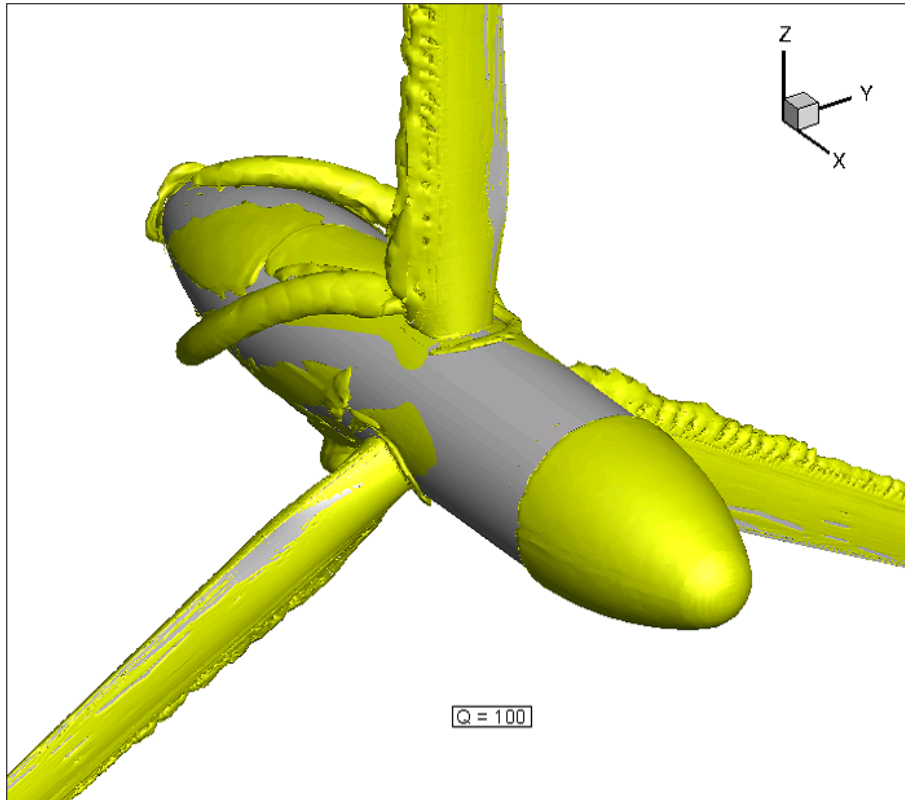
Figure 22: Iso-surfaces
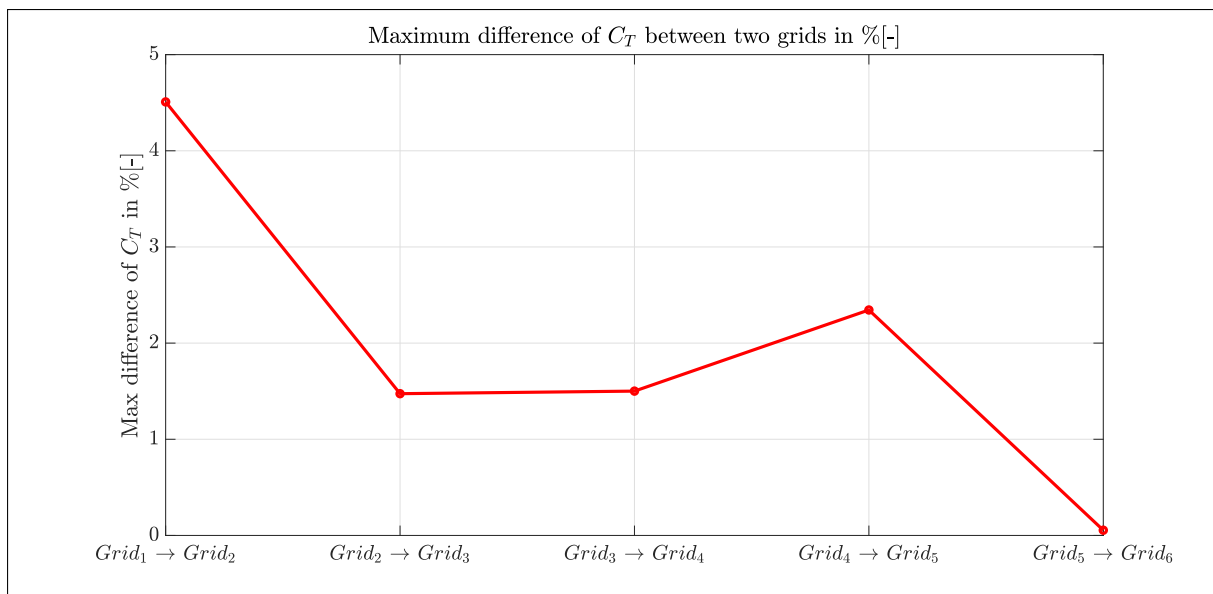
Figure 23: Changes of C_T in percentage

and only end 200 iterative quantities are considered. It was found that the changes between quantities are the range of 10^{-3} percent(almost negligible) as shown in table 9 and this gives a clear idea that obtained large residuals almost tends to zero.
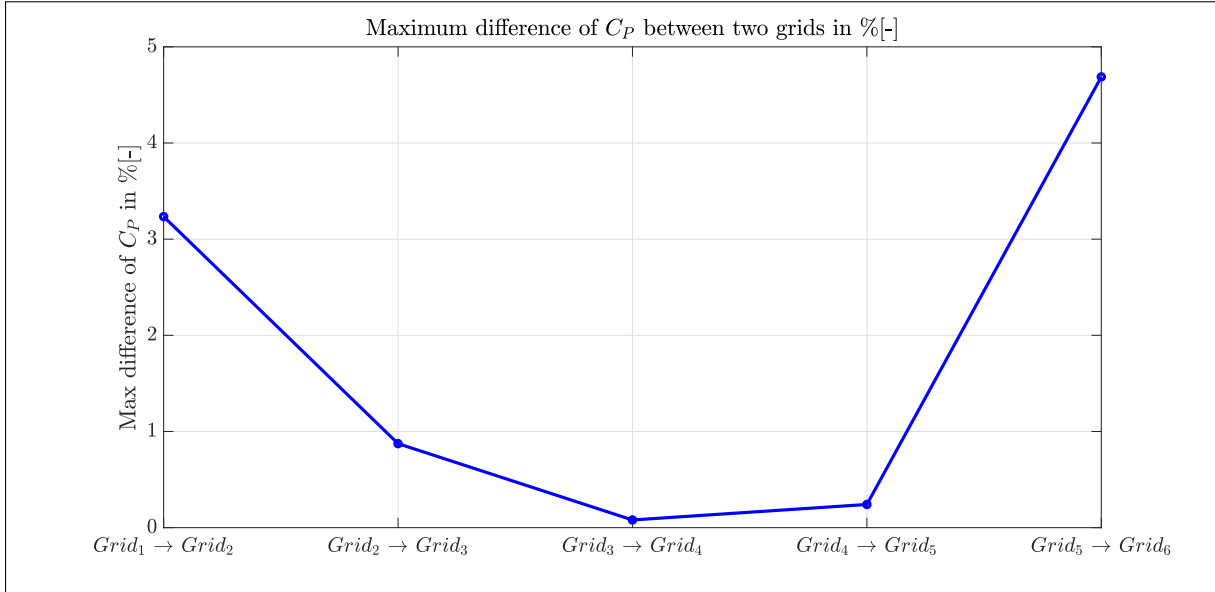
Figure 24: Changes of C_P in percentage

Table 9: Fluctuation studies of flow quantities

Grid no	Grid ref. $\frac{h_i}{h_1}$	n_{iter}	Fluct. last 200 iterations $100 \times max\left(\left|\phi_i - \phi_{end}\right| / \left|\phi_{end}\right|\right)$	
			C_T	C_P
1	1.54	6000	0.001	0.001
2	1.39	6000	0.001	0.001
3	1.26	6000	0.001	0.001
4	1.18	6000	0.001	0.001
5	1.14	6000	0.001	0.001
6	**1.00**	**6000**	**0.001**	**0.001**

7.2.2 Discretization Error

The numerical uncertainty estimation is discussed in this section. Many methods are available for estimating uncertainty in CFD. The strategy used in [26] will be used in this study. This study aims to construct a 95% confidence interval that contains an exact solution.

The final estimations are represented in the table 10 for all the 6 grids. The numerical uncertainty of Thrust coefficient(C_T) and Power coefficient(C_P) is found to be 9.7% and 28.6% for grid no. 6(refined grid). The plots for uncertainty estimation are shown in figure 25.

From coarse to fines grids, the magnitude of C_T and C_P follows increasing and decreasing trends, respectively. The relative difference between two grids for C_T and C_P in percent

is shown in the same table 10(fourth and seventh columns), and the same can be depicted in 26. The relative difference is negligible for C_T, and considerable differences are found for C_P. The maximum relative difference was less than 1 percent and 25.59 percent(found in the coarse grid) for C_T and C_P, respectively.

Table 10: Error estimation

Grid	Grid ref.	C_T		U_ϕ	C_P		U_ϕ
no	$\frac{h_i}{h_1}$	$[-]$	$[\%]$	$[-]$	$[-]$	$[\%]$	$[-]$
		Flow case $V_{inflow} = 1.61\ m/s$ and TSR $= 7.0$					
1	1.54	0.3934	-4.18	21.8%	0.1613	25.59	60.6%
2	1.39	0.4051	-1.3	18.1%	0.1510	17.56	50.7%
3	1.26	0.4073	-0.81	14.7%	0.1430	11.32	42.7%
4	1.18	0.3953	-3.7	15.7%	0.1386	7.90	38.4%
5	1.14	0.4089	-0.31	11.7%	0.1328	3.39	37.9%
6	**1.00**	**0.4106**	**-**	**9.7%**	**0.1284**	**-**	**28.6%**

However, The relative difference between C_T and C_P is very high because C_P is derived by using a moment about the turbine's rotor. The incorporated distance from the rotating axis results in changes in lift(C_l) & drag(C_d) near the blade tip to significantly impact C_P. Also (C_T) is derived from thrust force(In axial direction), hence any changes in C_l/C_d could impact C_T. Moreover, the inflow velocity, $V_{inflow} = 1.61\ m/s$ is used for all the computations and flow domain around the wind turbine is found to be not stable. An better numerical uncertainty or convergence could be achieved if the inflow velocity increased to 2 m/s or so.

From the above studies, it can be clear that obtaining an exact solution is challenging when performing steady calculations. The most refined grid is used for the rest of the work. Also, the numerical uncertainty is 9.7 and 28.6 percent for C_T and C_P, respectively. In contrast, the relative difference for the two most refined grids is 0.31 and 3.39 percent C_T and C_P, respectively.
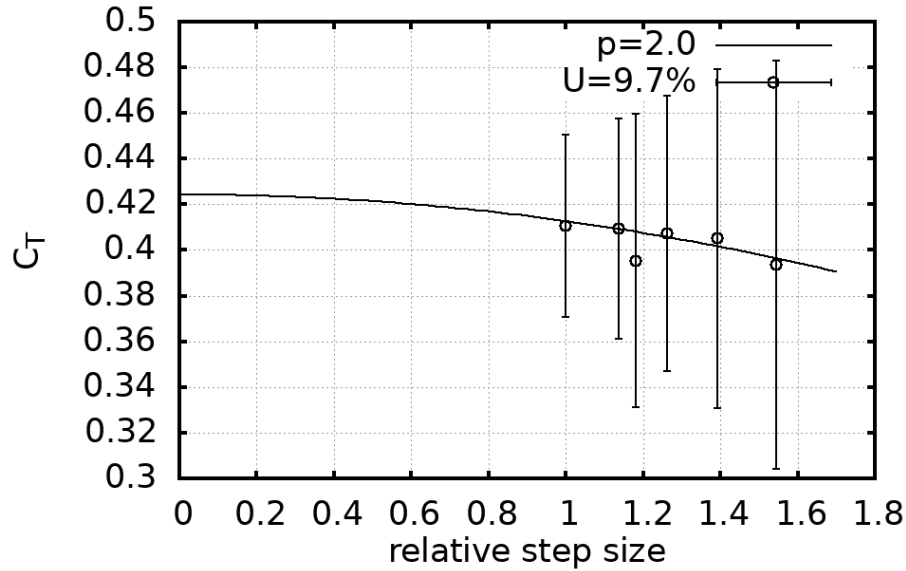
(a) Uncertainty estimation C_T.
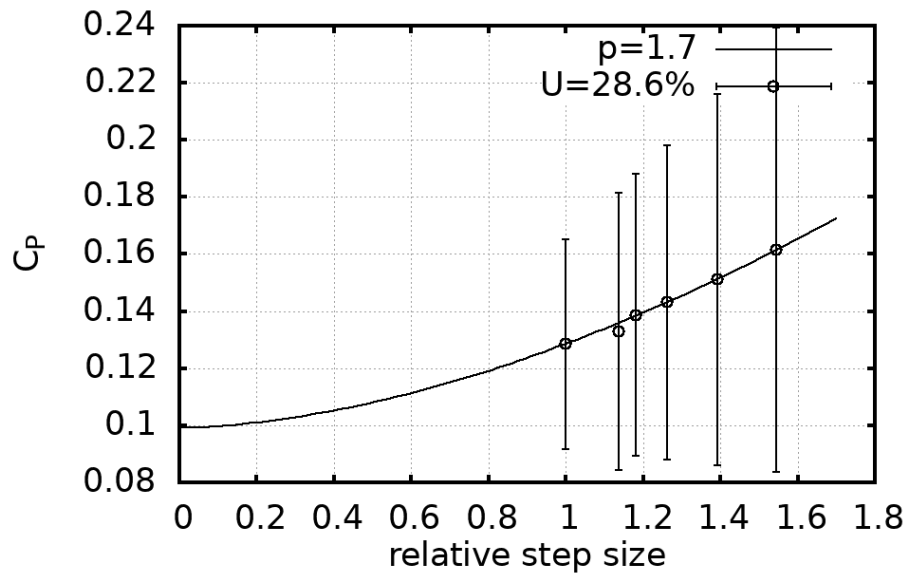
(b) Uncertainty estimation C_P.

Figure 25: Plot of error estimation for both C_T and C_P as a function of relative step size.

7.3   Turbulence Modeling

The numerical computations are performed with k - ω Shear Stress Turbulence(SST) (2003) model, Spalart-Allmaras model and k - $\sqrt{K}L$ Scale-Adaptive-Simulation Model (SAS).

The flow characteristics(C_T and C_P) are obtained for the above turbulence models(at the same flow condition) and are presented in table 11 and the same can be depicted in figure 27.
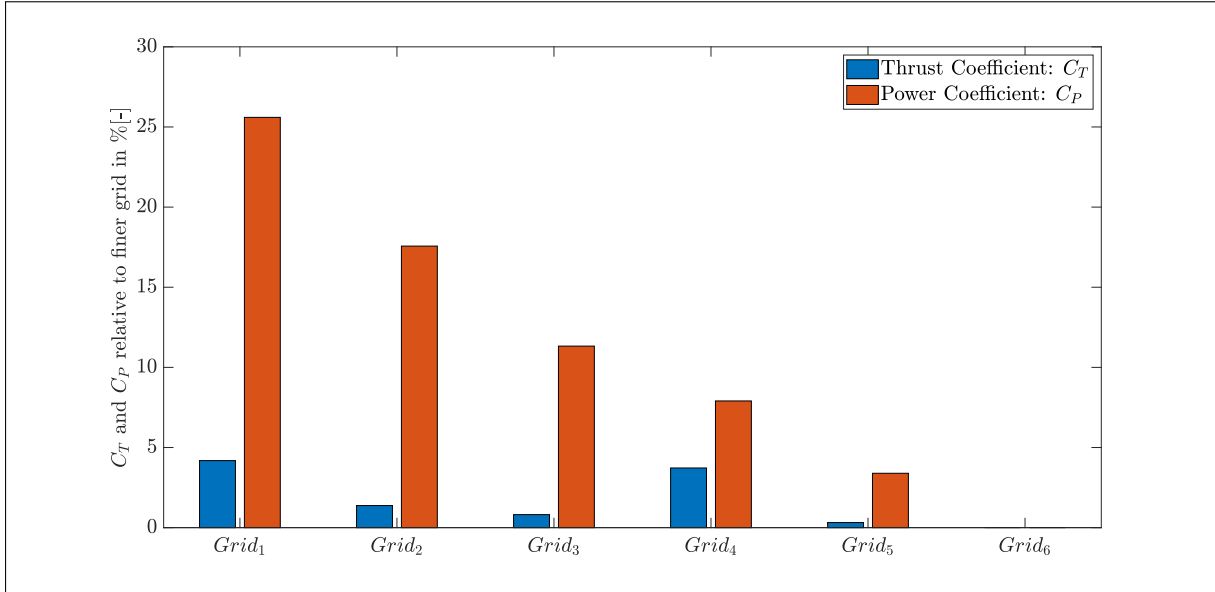
Figure 26: Power and thrust coefficient as percentage of the finest grid solution.

Table 11: Flow characteristics(C_T and C_P) for three turbulence models

S.No	Turbulence Model	C_T	[%]	C_P	[%]
1	Spalart-Allmaras	0.3902	-4.97	0.1181	8.05
2	k - $\sqrt{K}L$	0.3973	-3.25	0.1202	6.44
3	k - ω SST (2003)	0.4106	-	0.1284	-

From the table 11, the magnitude of C_T associated with k - ω SST model is high in comparison with the Spalart-Allmaras model and k - $\sqrt{K}L$ Scale-Adaptive-Simulation Model (SAS). Whereas, C_P is found to be having large sensitivity. The fourth and sixth column in the table 11 represents the relative difference of C_T and C_P coefficients as a percentage of third turbulence model for the finer grid and the same can be predicted both in figures 28 and 29.

Since we already discussed in the previous section 7.2.2, C_P is derived by using a moment about the turbine's rotor. The incorporated distance from the rotating axis results in changes in lift(C_l) & drag(C_d) near the blade tip to significantly impact C_P. So, each turbulence model varies with the flow region on the blade surface and the amount of lift generated. Whereas the axial force acting on the turbine, on the other hand, is used to calculate C_T. Also, C_l and C_d contribute equally across the rotor blade surface. The normalized turbulence viscosity in the axial direction of the rotor blade is plotted at r/R = 0.3, 0.5, 0.7 and 0.9 as shown in figure 33 for model-scale conditions. An iso-curve of
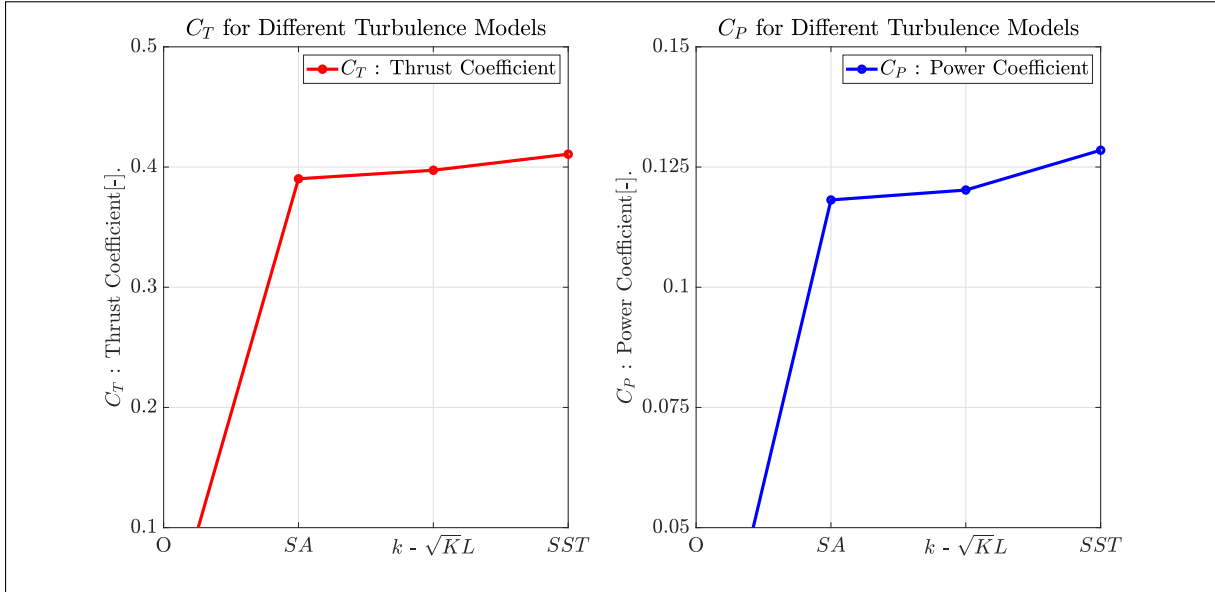
Figure 27: Thrust and Power coefficient for different turbulence models.
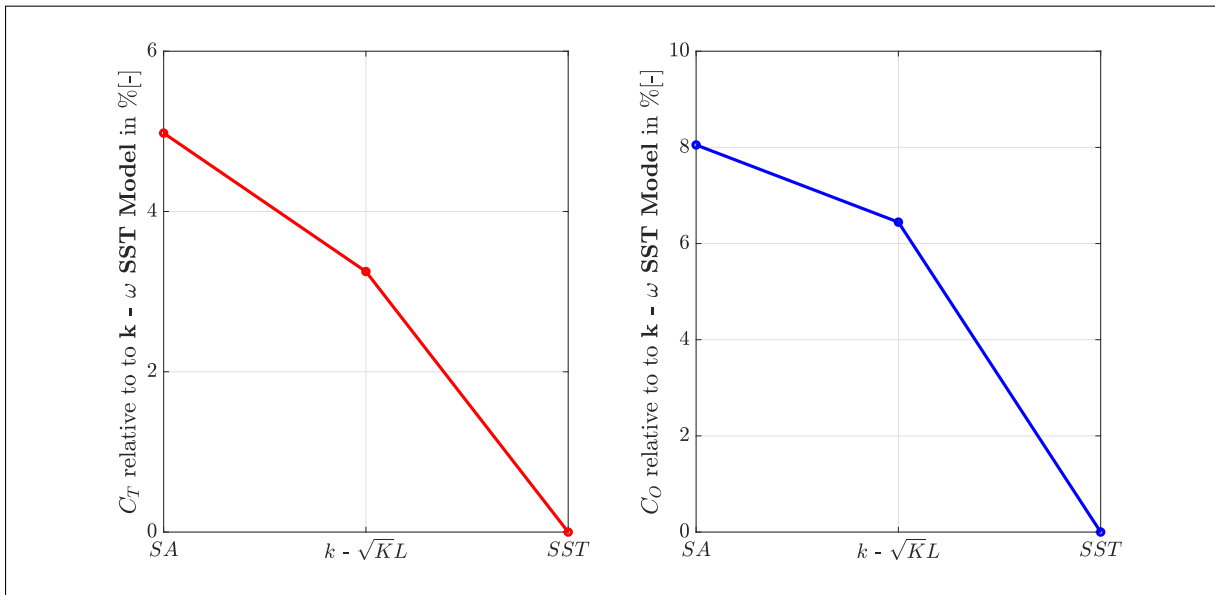
Figure 28: Thrust and Power coefficient as a percentage of k - ω SST (2003) model.

turbulence viscosity for $\mu_t = 1$ is given in this figure. The turbulence viscosity generated by the k - ω SST model is much higher for all areas along the turbine blade When compared to the Spalart-Allmaras and $K - \sqrt{K}L$(SAS) solution. The separated flow region can be depicted in the figure 33 with k - ω SST model and the other turbulence model solutions can also be compared here. Also, thereafter velocity plots(see figures 36 and 37. The difference in turbulence viscosity production between the three models is clearly visible. From the previous study, the performance of three turbulence models, i.e., k - ω Shear Stress Turbulence(SST) (2003) model, Spalart-Allmaras model, and k - $\sqrt{K}L$ Scale-
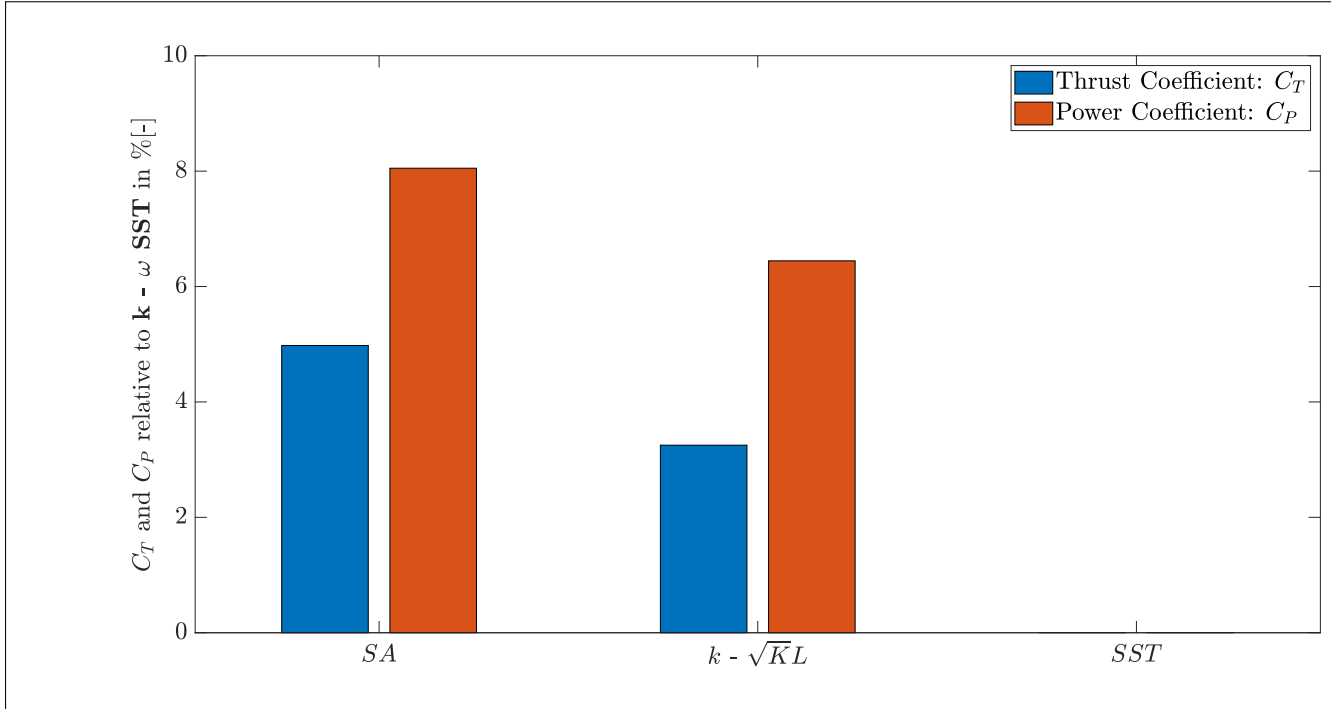
Figure 29: Thrust and Power coefficient for different turbulence models.

Adaptive-Simulation Model (SAS) works distinct from each other at model scale conditions. All the models greatly influence the pressure side of the rotor surface, and the size of this region has a significant impact on C_P. As a result, there are substantial differences in the models for C_P, whereas they are significantly smaller for C_T. The k - ω SST model is used for further simulations.

7.4 Results and Discussion

This section is dedicated to comparing the final results. Also, the experimental results are not available for the present flow case. So, a different validation of results is considered for the present work. In section 7.2, the error associated with numerical computations is estimated using the least-squares approach(LS). The relative difference(RD) between the two most refined grids for both C_T and C_P and the same can be depicted in table 10(4th, 5th, 7th & 8th columns) So, here in this work, and the results are compared between them. Along with them, the full-scale results are also presented. With reference to [27], it was decide to consider an safety factor(F_s) = 3.0 for the posterior approach.

In the present work, only one flow condition is considered for all the numerical computations, and It is depicted in the table 3. For validation part, the numerical computations
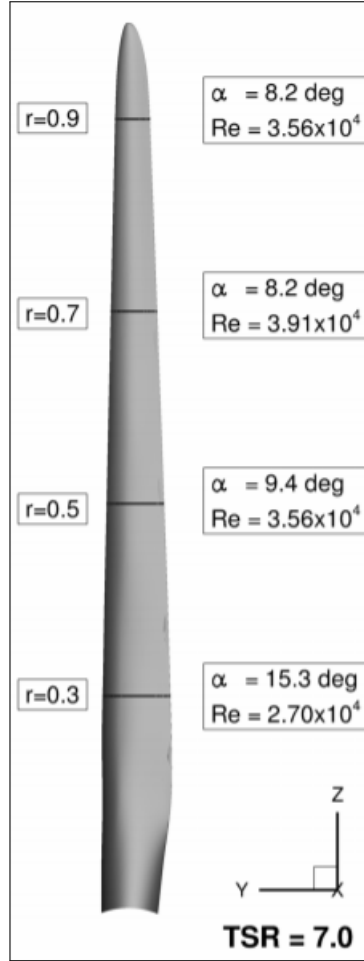
Figure 30: Rotor blade

are performed with different TSRs(3,4,5,6,7,8) and with same $V_{inflow} = 1.61m/s$. The uncertainty estimated for TSR = 7 is assumed for other TSRs.

The uncertainty estimation for both approaches($U_{\phi_{LS}}$ & $U_{\phi_{RD}}$) for all TSRs can be found in the table 12. At the same time, $U_{\phi_{RD}}$ is included with $F_s = 3.0$. .

Table 12: NREL model-scale numerical uncertainty obtained using relative difference of two finest grids and uncertainty estimation based on least-squares method.

	C_T	C_P
$U_{\phi_{LS}}$	9.7%	28.6%
$U_{\phi_{rel}}(F_s = 3.0)$	0.93%	10.17%

The figures 31 and 32 represents the comparison of C_T(Thrust coefficient) and C_P(Power coefficient) plots calculated with both approaches(LS & RD). The plots include full-scale and model-scale predictions computed with CFD code ReFRESCO. The towing tank test results performed at MARIN, Netherlands, are also added.

In this thesis work, all the calculations(model and full scale) are performed at 0^0 blade pitch. Whereas the tank results are conducted at 6.4^0 and inflow speed of $V_{inflow} = 2.94$ m/s.

The simulations are not conducted at 6.4^0 blade pitch because it requires a new domain and grid. The magnitude of C_T and C_P at TSRs $= 3$ to 8 are presented in tables 13 and 14. When comparing the C_T curves(shown in figure 31), the model-scale predictions of CFD computations between least-squares approach($U_{\phi_{LS}}$) and the relative difference($U_{\phi_{RD}}$) are aligned perfectly. The C_P curve showed huge differences between both approaches because the error estimated for C_P was very high as it depends on the moment and the quantity or amount of the flow region on the rotor surface. This works like more region, more power extracted from the turbine. As we already in the previous section, the flow is laminar at model-scale, and it is turbulent at full-scale(It is based on Reynolds number(Re)). This is why full-scale results are not aligned with model-scale results. The differences between both approaches in percentage are calculated and can be seen in the fourth column of tables 13 and 14.

Table 13: Percentage difference between both approaches for C_T

TSR	Least-Scale Approach	Relative Difference	[%]
1	0.058	0.055	-6.2
2	0.117	0.110	-6.3
3	0.128	0.165	22.1
4	0.172	0.220	22.0
5	0.234	0.275	14.8
6	0.328	0.331	0.7
7	**0.410**	**0.386**	**-6.3**
8	0.484	0.441	-9.7

Table 14: Percentage difference between both approaches for C_P

TSR	Least-Scale Approach	Relative Difference	[%]
1	0.020	0.011	45
2	0.041	0.023	45
3	0.062	0.034	45
4	0.083	0.064	23.1
5	0.104	0.087	16.5
6	0.125	0.088	29.6
7	**0.146**	**0.128**	**12.4**
8	0.167	0.197	-17.5
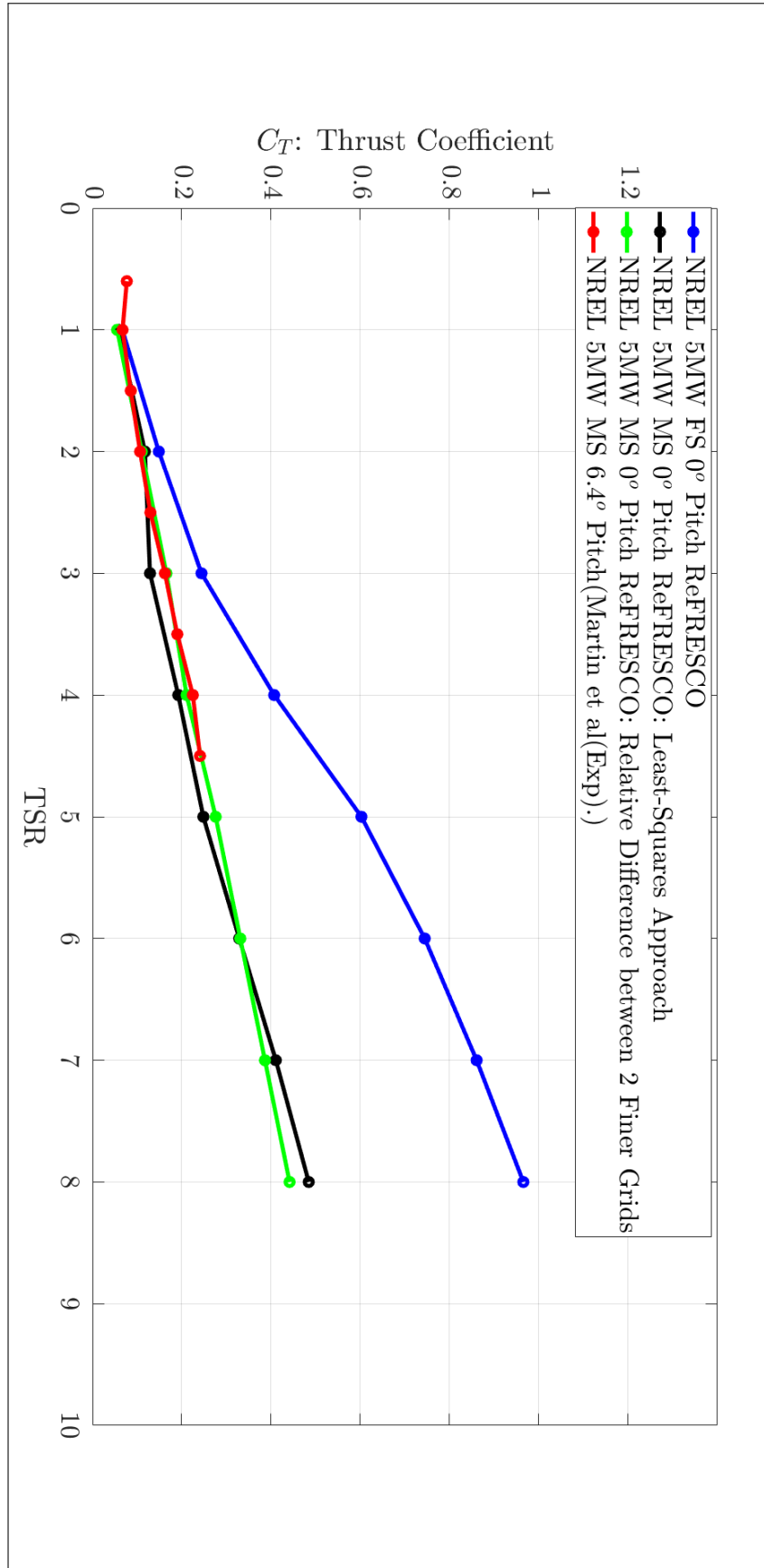
Figure 31: C_T curves of model-scale NREL including uncertainties.
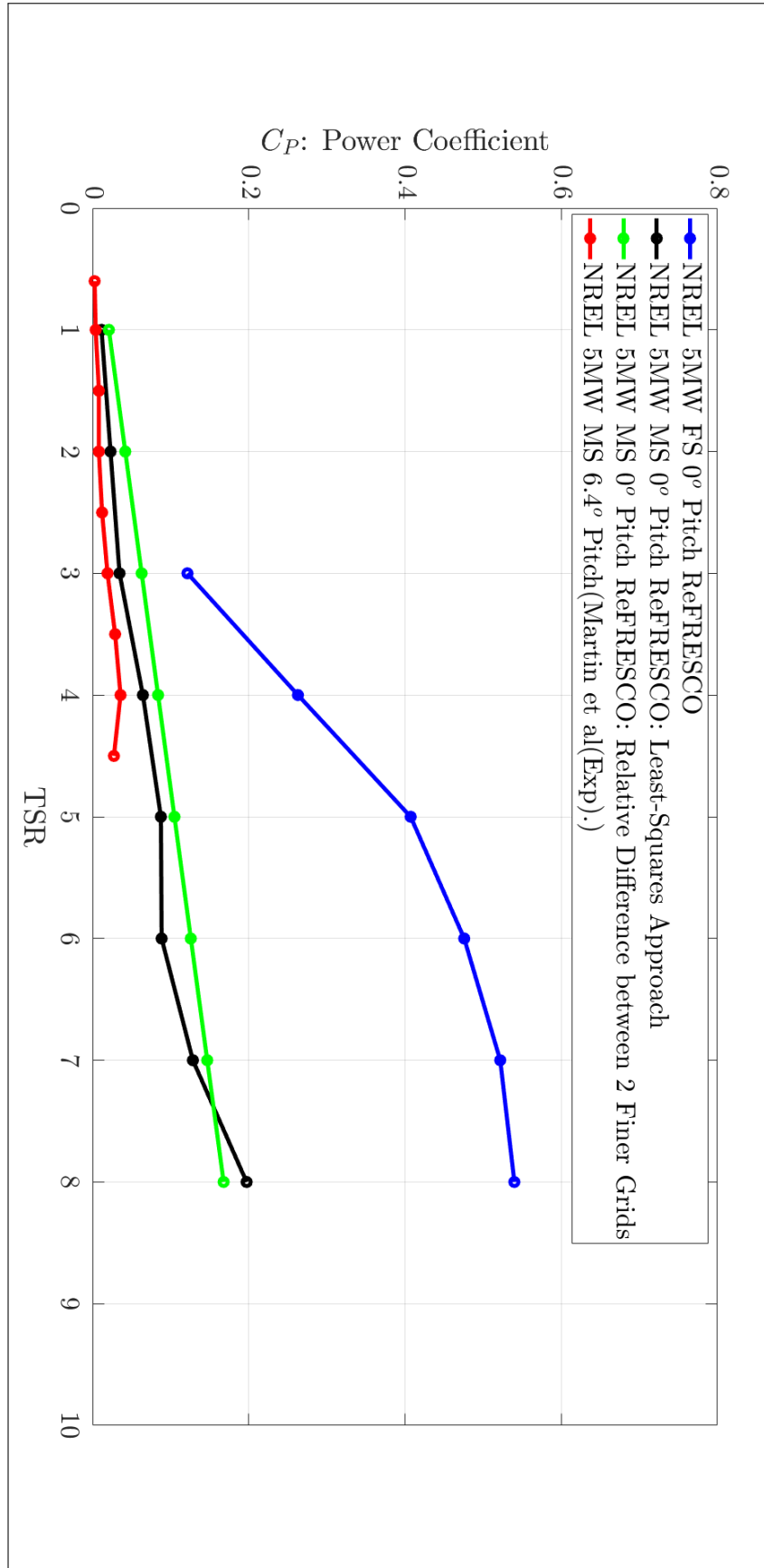
Figure 32: C_P curves of model-scale NREL including uncertainties.

(a) k - ω SST (2003)   **(b)** Spalart-Allmaras   **(c)** k - $\sqrt{K}L$(SAS)

(d) k - ω SST (2003)   **(e)** Spalart-Allmaras   **(f)** k - $\sqrt{K}L$(SAS)

(g) k - ω SST (2003)   **(h)** Spalart-Allmaras   **(i)** k - $\sqrt{K}L$(SAS)

(j) k - ω SST (2003)   **(k)** Spalart-Allmaras   **(l)** k - $\sqrt{K}L$(SAS)
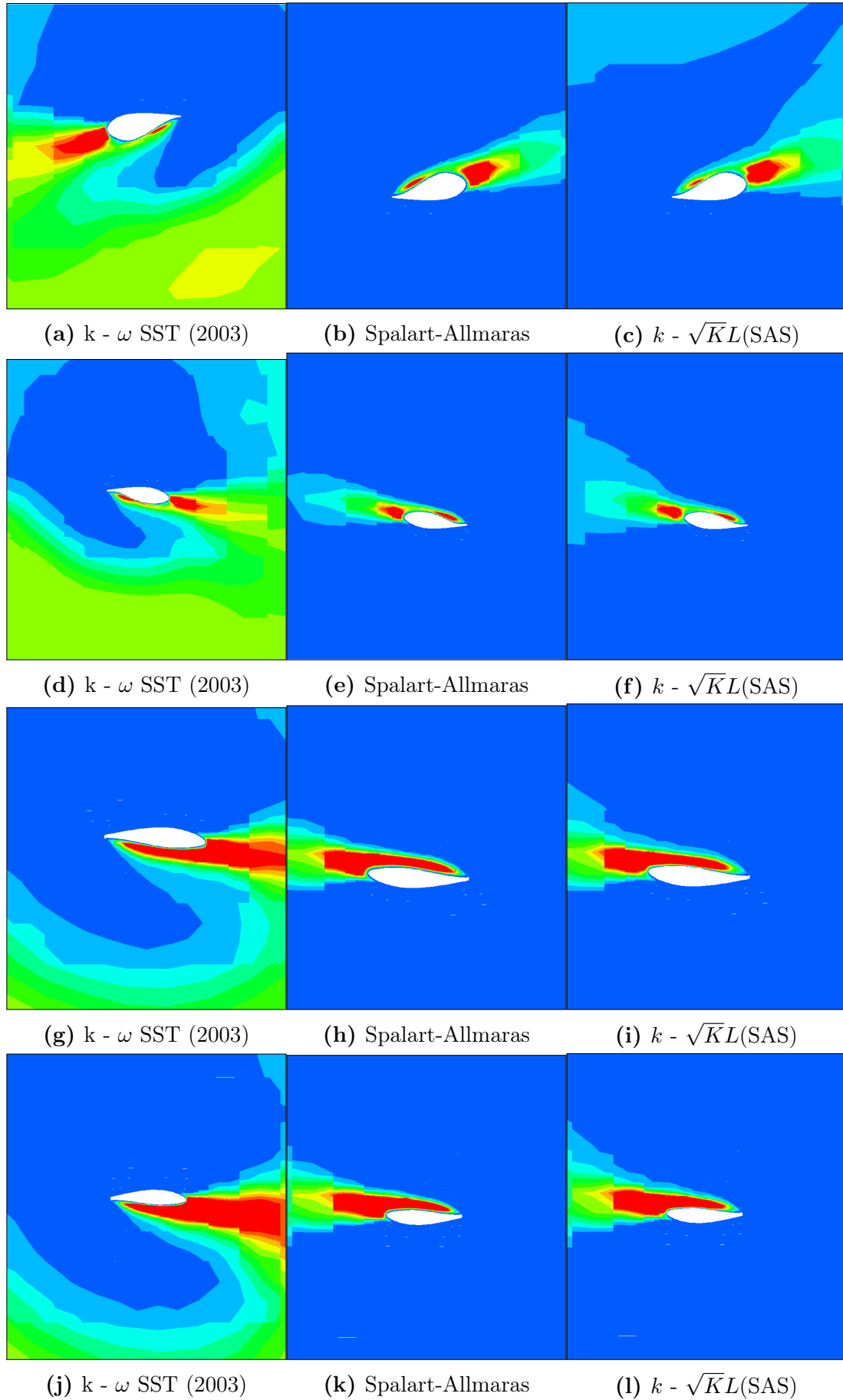
Figure 33: Plot of Normalized turbulence viscosity at different section(r= 0.3, 0.5, 0.7 and 0.9) for all three turbulence models

(a) r = 0.30

(b) r = 0.50

(c) r = 070

(d) r = 090

(e) r = 095

(f) r = 0.099
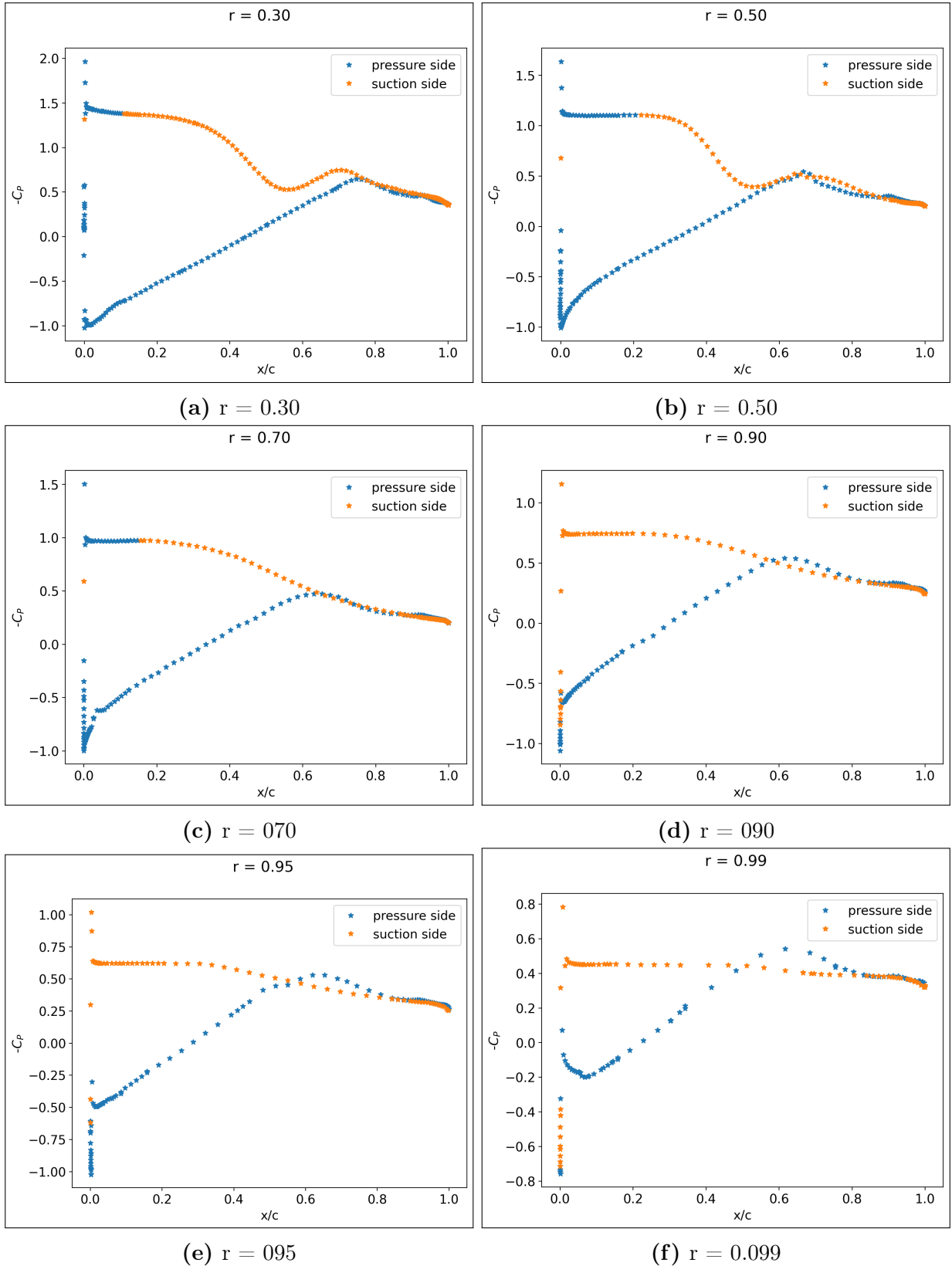
Figure 34: Pressure Coefficient(C_P) along blade span

(a) r = 0.30

(b) r = 0.50

(c) r = 070

(d) r = 090

(e) r = 095

(f) r = 0.099
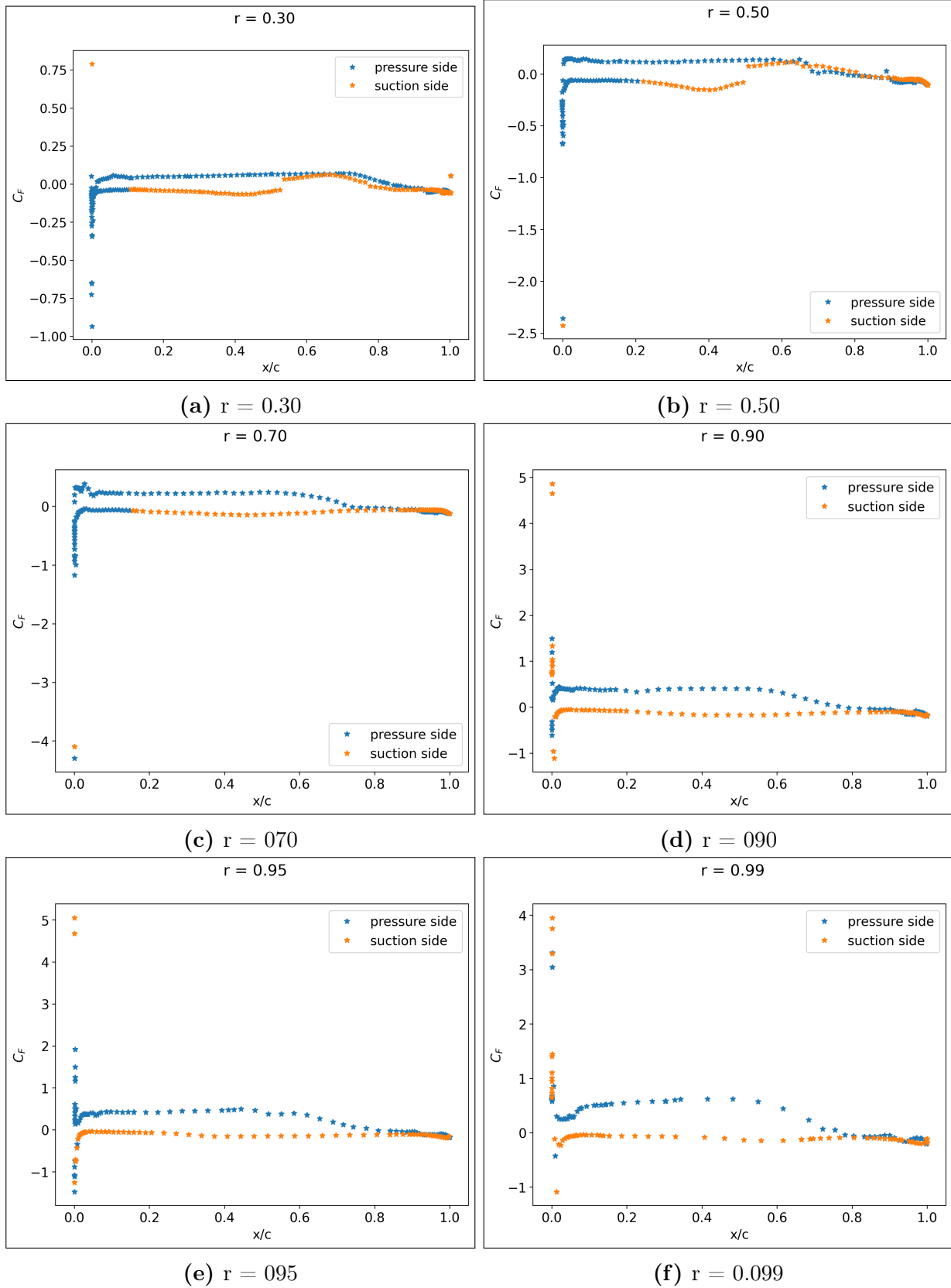
Figure 35: Skin Friction Coefficient(C_P) along blade span
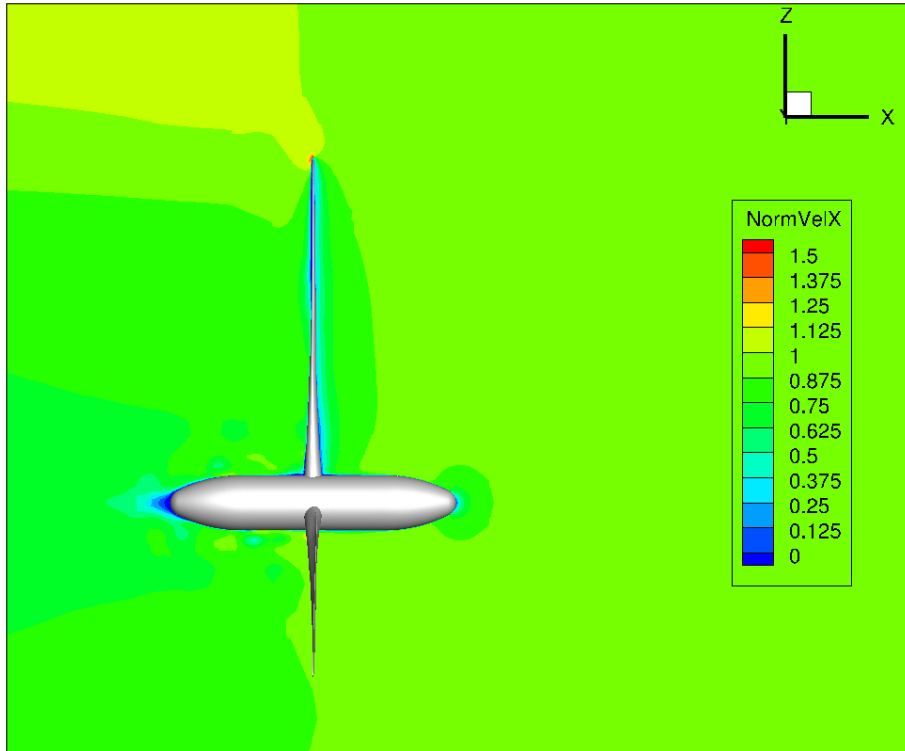
Figure 36: Plot of Axial Velocity
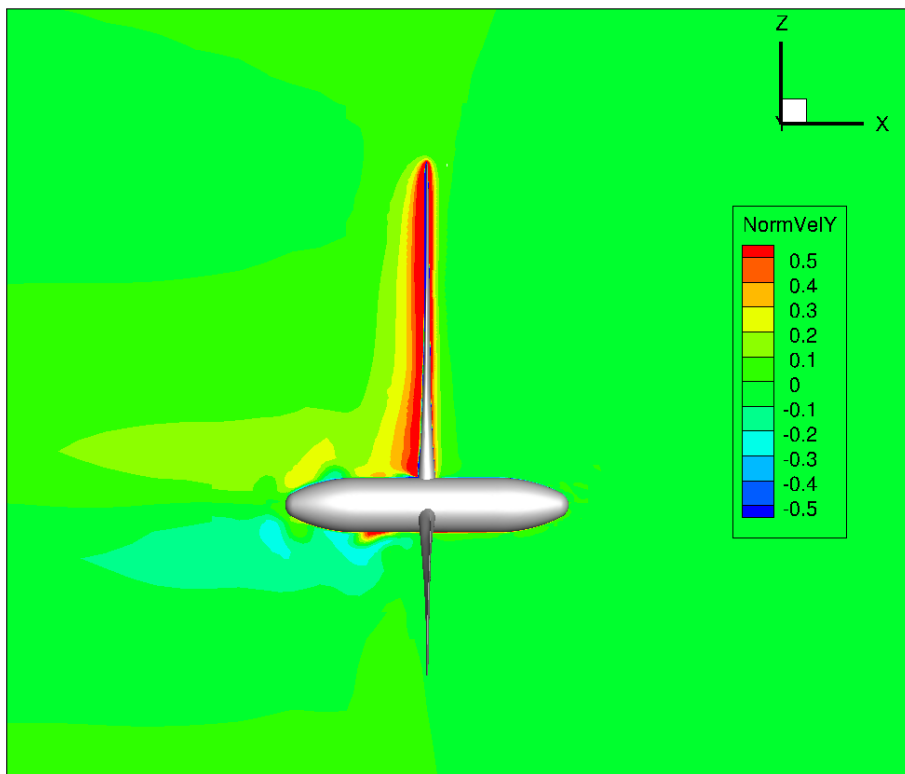
Figure 37: Plot of Radial Velocity

8 Numerical Study on NREL 5MW Wind Turbine at Model-Scale using Sliding Grid Methodology

In this section, the unsteady simulations are performed using the Sliding grid methodology. The present chapter starts with selection of domain size for both sub-grids section 8.1. The error associated with numerical studies is explained in section 8.2. In section 8.1. a sensitivity analysis on time step is discussed due to unsteady computations. In section 8.4 the NREL 5MW Wind Turbine model-scale computations are validated against different numerical approaches. All computations are performed using (U)RANS software *ReFRESCO*.

8.1 Domain Selection

As explained in section 6.2.1, the whole grid is split into two sub-grids, i.e., the outer domain contains a hole(static part) and the inner domain, which includes turbine(dynamic part). One can clearly understand that the final grid, which is obtained by combining subgrids, will have exact dimensions of **Domain C** which we have seen in previous studies. The domain dimensions of the sub-grids are depicted in the table 15 and 16

Table 15: Overview domains used and corresponding dimension of Outer Domain.

Identifier	Upstream Length: nD	Wake Length: nD	Radius: nD
Domain **C**(with hole)	15	60	30

Table 16: Overview domains used and corresponding dimension of Inner Domain.

Identifier	Upstream Length: nD	Wake Length: nD	Radius: nD
Hole	1.5	3.5	2.5

Note: As stated in the numerical setup for sliding interfaces methodology, the inner domain is dynamic in nature since it rotates whereas the outer domain is static in nature and behaves as stationary.

8.2 Numerical Uncertainty Study

A total of 4 grids with a number of cells varying between 36.2M to 51.8M are analyzed to estimate the error associated with the numerical computations. Table 20 shows the properties of the grids. The grids are generated to keep as geometric a similarity as possible. An iteratively converged numerical solution is difficult to obtain because of flow

characteristics in model-scale conditions already discussed in the previous section. All the computations are performed same flow condition, and it is presented in 3.

8.2.1   Iterative Error

The error initiated at each iteration during each time step for all grids is shown in the tables 7 & 8. The L_2-norm and L_∞-norm of the residuals are in the range of 10^{-3} and 10^2 respectively.

Table 17: Maximum L_2 Residuals(Sliding grid)

Grid no	Grid ref. $\frac{h_i}{h_1}$	Total timesteps	Maximum L_2 Residuals (u,v,w,p)
1	1.54	360	$1.5 \cdot 10^{-2}$
2	1.54	360	$1.8 \cdot 10^{-2}$
3	1.39	360	$2.9 \cdot 10^{-3}$
4	**1.00**	**360**	**$2.5 \cdot 10^{-3}$**

Table 18: Maximum L_∞ Residuals(Sliding grid)

Grid no	Grid ref. $\frac{h_i}{h_1}$	Total timesteps	Maximum L_∞ Residuals (u,v,w,p)
1	1.54	360	$1 \cdot 10^2$
2	1.54	360	$0.39 \cdot 10^2$
3	1.39	360	$0.04 \cdot 10^2$
4	**1.00**	**360**	**$0.02 \cdot 10^2$**

Since, there is no experimental data available for this study, a new grid is prepared which is same with this sliding grid interfaces and their properties are explained in the table 19

The figures 38(at each outerloop) and 39(at each timestep) represents the convergence plots for L_2-norms residuals at each outer loop and each time step. Thrust coefficient(C_T) and Pressure coefficient(C_P) for grid no. 6(refined grid). These plots are very much useful for estimating errors against number of iterations(6000 in this case).

Table 19: Residuals study for identical grid

Grid	Total no.of cells	n_{iter}	Maximum L_2 Residuals (u,v,w,p)	Maximum L_∞ Residuals
Flow case $V_{inflow} = 1.61\ m/s$ and TSR = 7.0				
Identical grid	**51345892**	**6000**	**$4.7 \cdot 10^{-3}$**	**$8.1 \cdot 10^{-2}$**
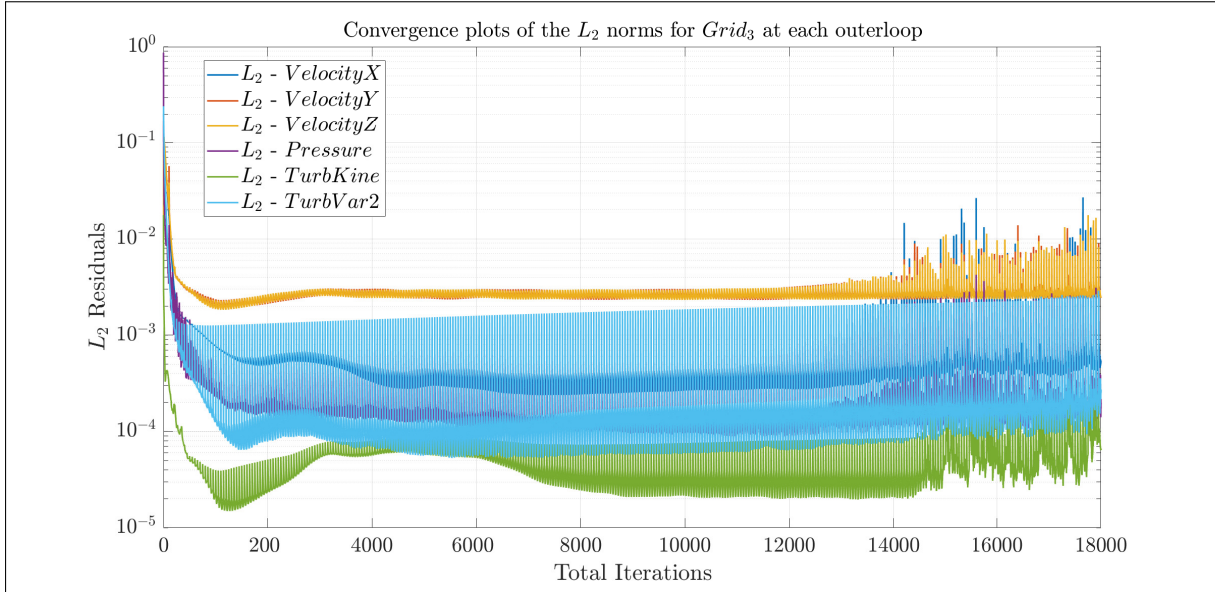
Figure 38: Iterative convergence plots of the L_2-norms of the residuals for finest grid at **each outerloop**.

Table 20: Refinement study for Sliding Interfaces

Grid Refinement	1	2	3	4
Total no.of Cells	36548377	36801857	38354676	50617895
Min Orthogonality	10.32	12.56	14.2	11.2
Avg Orthogonality	77.68	79.126	78.43	78.6
Max Skewness	0.903	0.877	0.874	0.864
Grid ref. ratio	1.54	1.39	1.26	1.00

Since, all the computations are unsteady, an time step is fixed at $\Delta T = 0.005$ for all the simulations in this chapter. Also, an indepth explaination on timestep is explained on section 8.3. In the previous studies, we have performed steady computations for an unsteady flow. And now the computations being unsteady we could see the iso-surfaces in the figure 40 and the same phenomenon could be depicted in figure 22 for steady computations. At this instant, the plots could give an clear idea of the flow. The main reason for the flow to be unsteady is due to the shape of the hub, and the same phenomenon can be found in [25]. Since, the flow being unsteady we could see drastic increase in the order of the residuals. If we compare the L_2-norm residuals of previous study and sliding grid, the residuals increases from 10^{-5} to 10^{-3}. Similarly, the L_∞-norm residuals changes from 10^{-2} to 10^2.
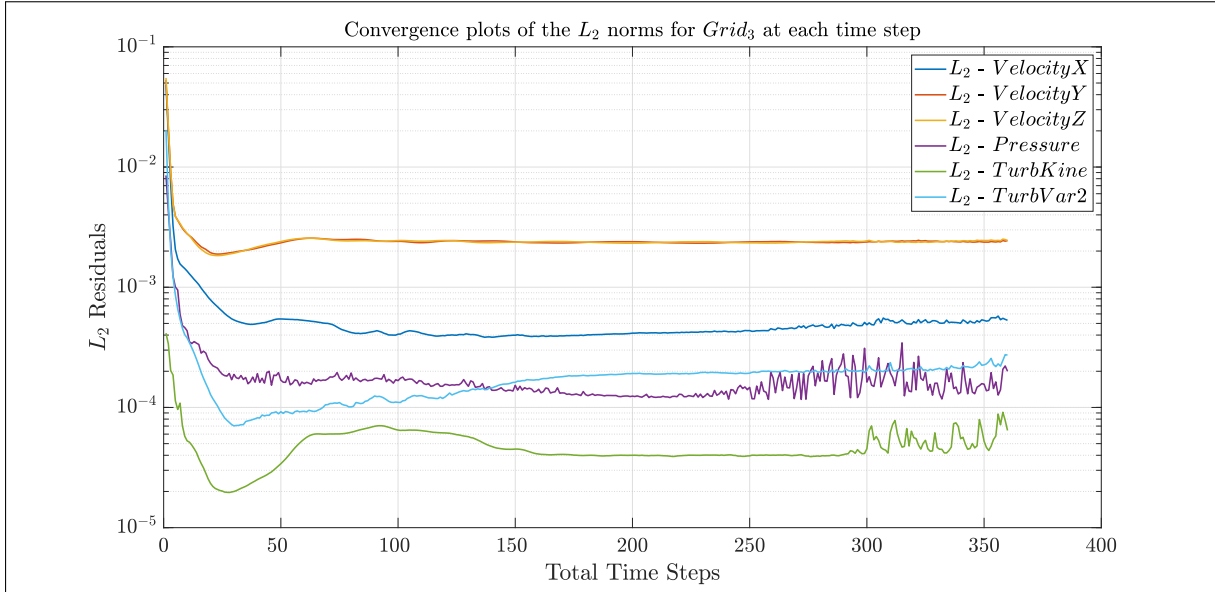
Figure 39: Iterative convergence plots of the L_2-norms of the residuals for finest grid at **each timestep**.

But, the computations are performed at the model scale. Obtaining lower values for the
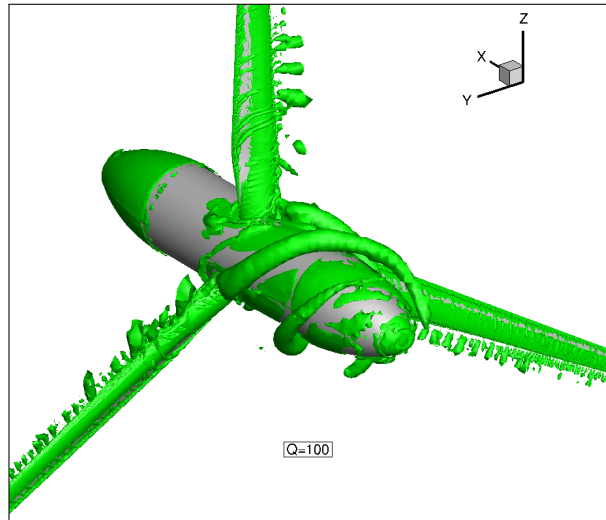
Figure 40: Iso-surface of dimensionless Q factor at the blade root($\bar{Q} = 100$).

residuals is challenging. Also, the flow being unsteady, there will be high blade loading and flow separation. For the identical grid, the order of L_2- and L_∞-norm of the residuals is precisely similar to the sliding grids. The main reason to have the same order is identical meshing and, hence, exact results. The convergence plots of the L_2-norms of the residuals, corresponding to the similar grid are presented in figure 42 and the maximum L_2- and L_∞-norm residuals can be depicted from the table 19. When we look at the change of the integral quantities C_T of the last 100 timesteps, the changes are all below 10 percent for
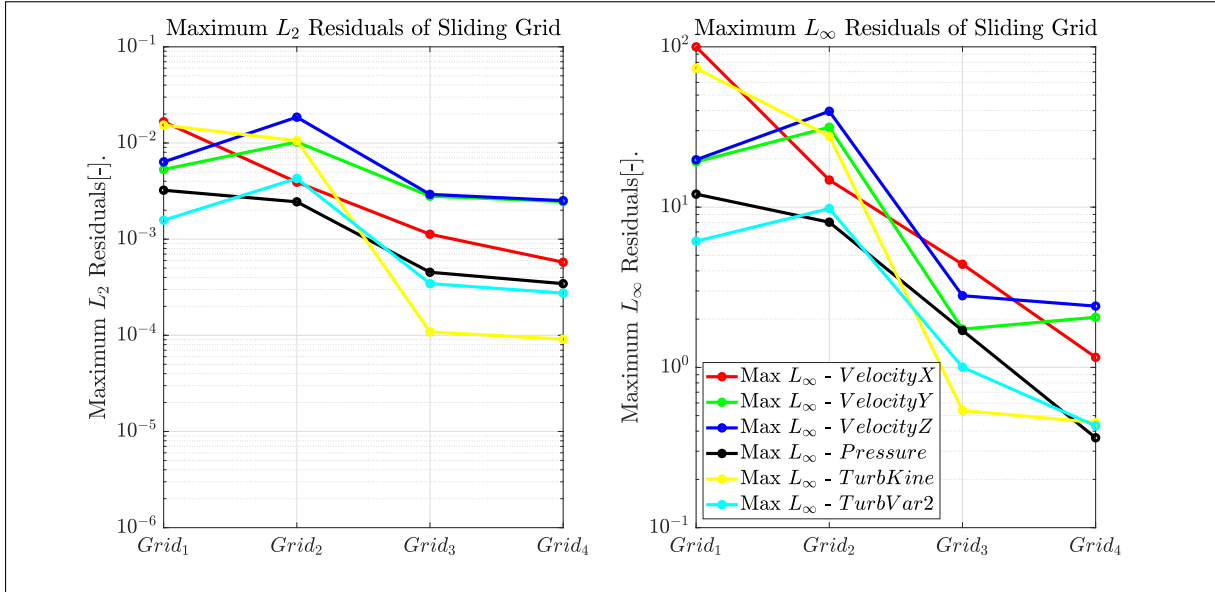
Figure 41: Maximum Residuals of Sliding Grid for finer grid.
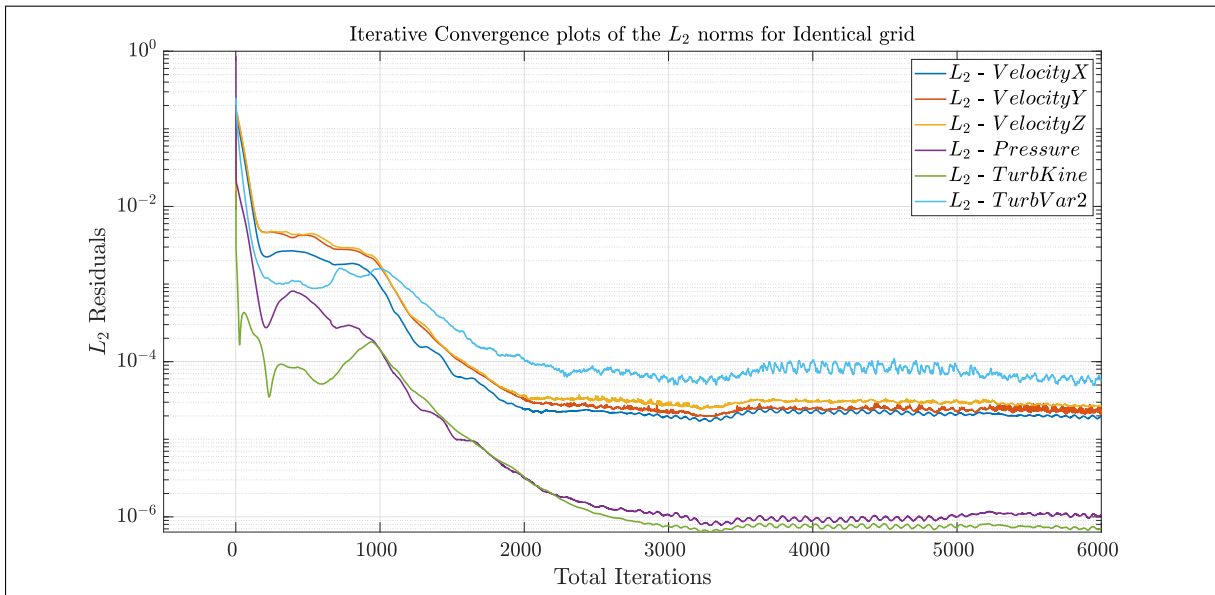
Figure 42: Iterative convergence plots of the L_2-norms of the residuals for Identical grid at **each timestep**.

C_T (when it reaches Grid 4) as shown in the figure 43.

The iterative convergence plots of C_T, corresponding to the most refined grid, can be depicted in the figure 44. From the above plots, it can be seen that the C_T converges to a constant value(a comparison between sliding and identical grids is also plotted at 45). Also, if we look at the maximum difference of C_T between two grids is found to be decreased from 6.4% to 0.18%. Meanwhile, When we look at the change of the integral quantities C_P of the last 100 timesteps, the changes are all below 0.2% percent for C_P
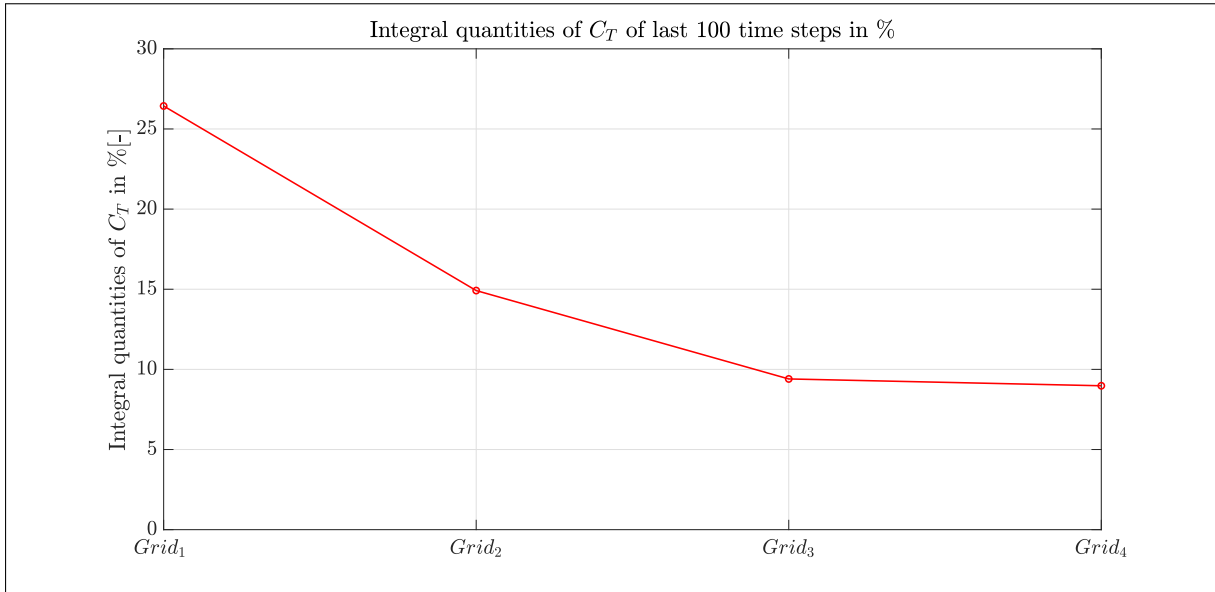
Figure 43: Integral quantities of C_T of last 100 time steps in % for finer grid at **each timestep**.
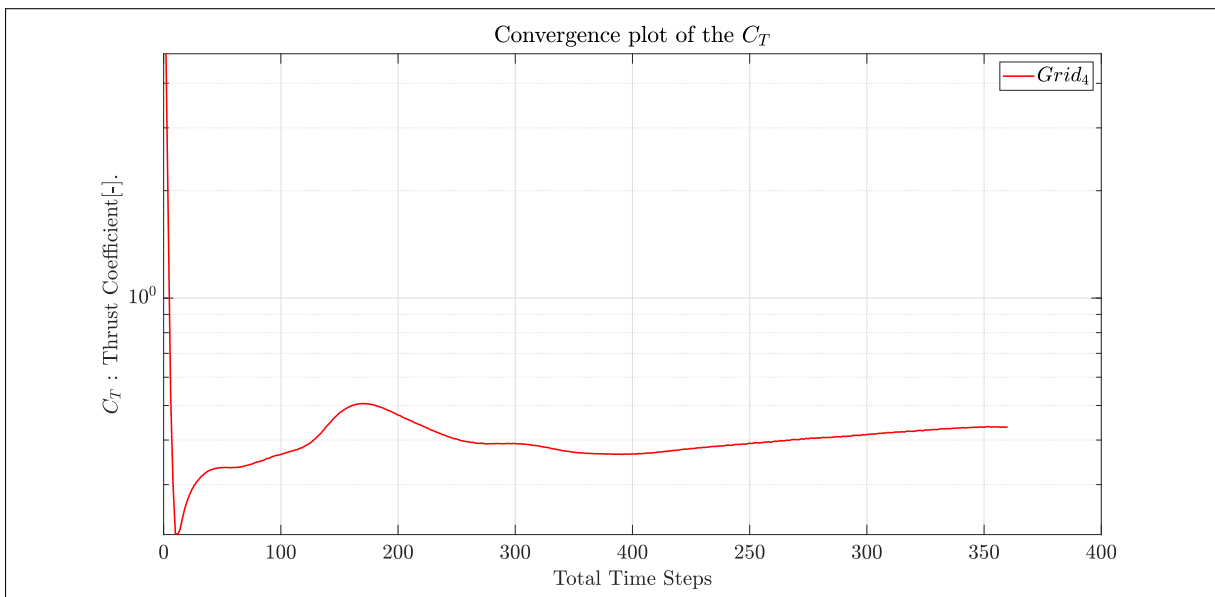
Figure 44: Iterative convergence plots of C_T for finest grid. at **each timestep**.

(when it reaches Grid 4) as shown in the figure 47. The iterative convergence plots of C_P, corresponding to the most refined grid, can be depicted in the figure 48 and comparison between sliding and identical grids is also plotted at 51.

Also, if we look at the maximum difference of C_P between two grids is found to be decreased from 4.19% to 0.24%.
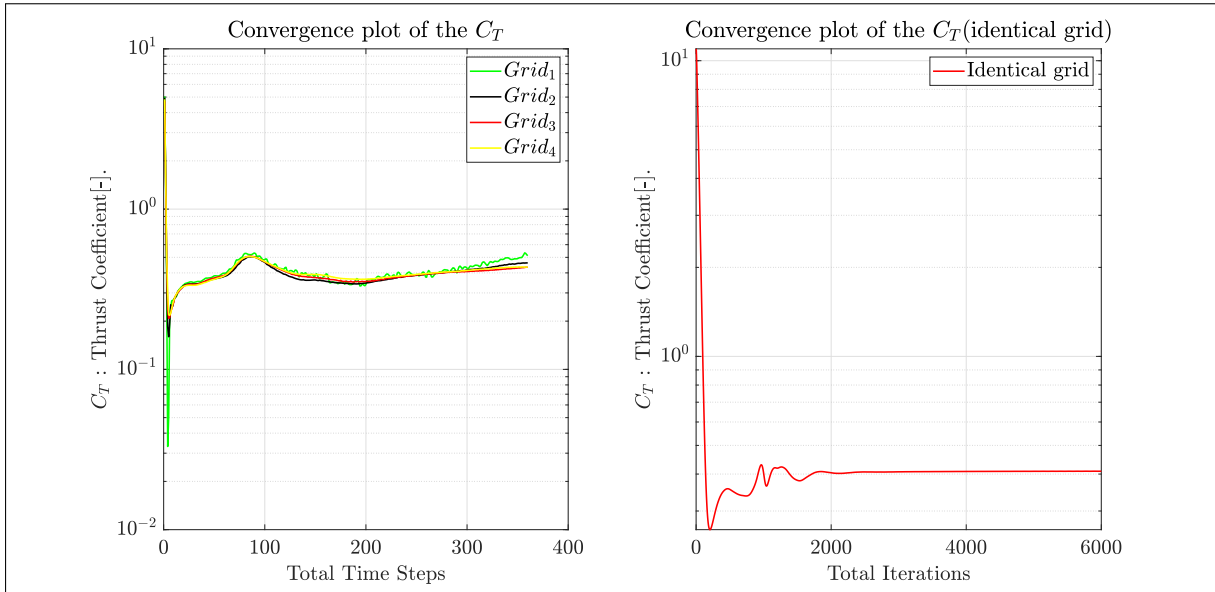
Figure 45: Comparison of iterative convergence plots of C_T for finest & Identical grid. at **each timestep**.
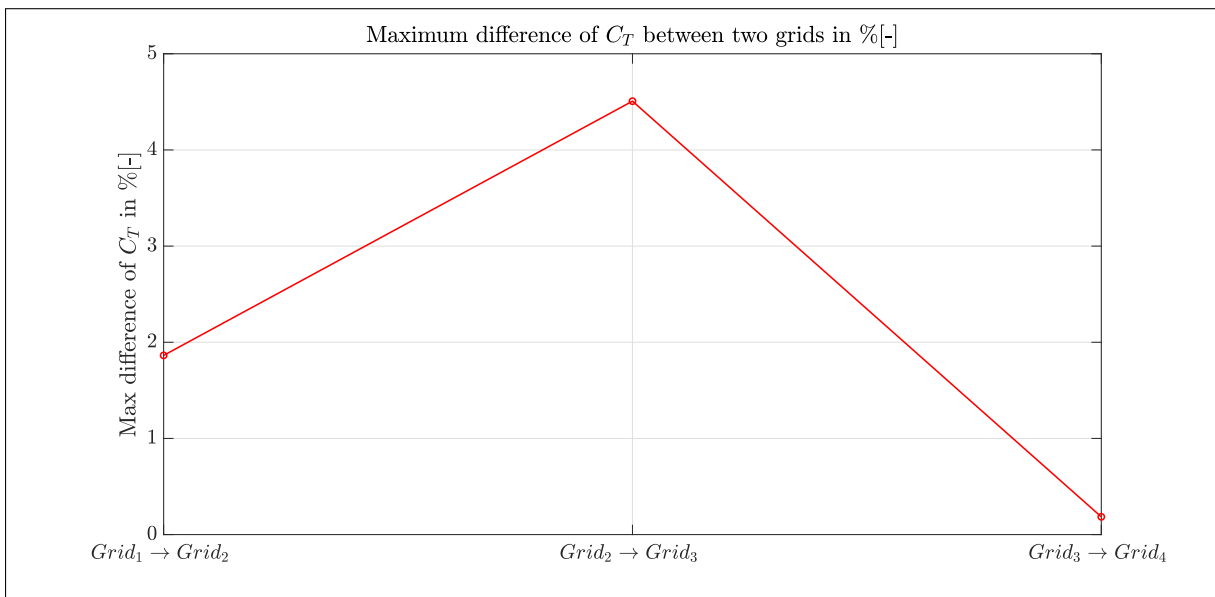
Figure 46: Maximum difference of C_T between sliding grids at **each timestep**.

8.2.2 Discretization Error

The numerical uncertainty estimation is discussed in this section. Many methods are available for estimating uncertainty in CFD. The same strategy[26] used in section 7.2.2 will be used in this study. For this study a wind speed of $V_{inflow} = 1.61\ m/s$ and TSR = 7, is used as explained before.

The resulting numerical uncertainty estimations are presented in table 21 for all sliding grids at the specified flow condition. When looking at the estimated uncertainties pre-
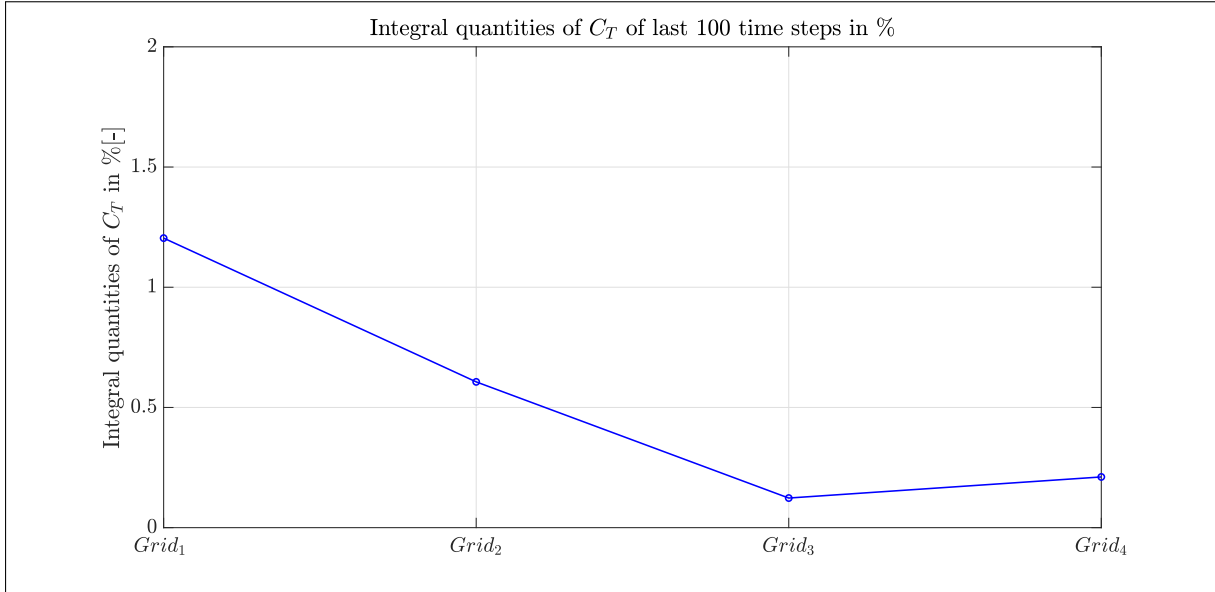
Figure 47: Integral quantities of C_P of last 100 time steps in % for finer grid at **each timestep**.
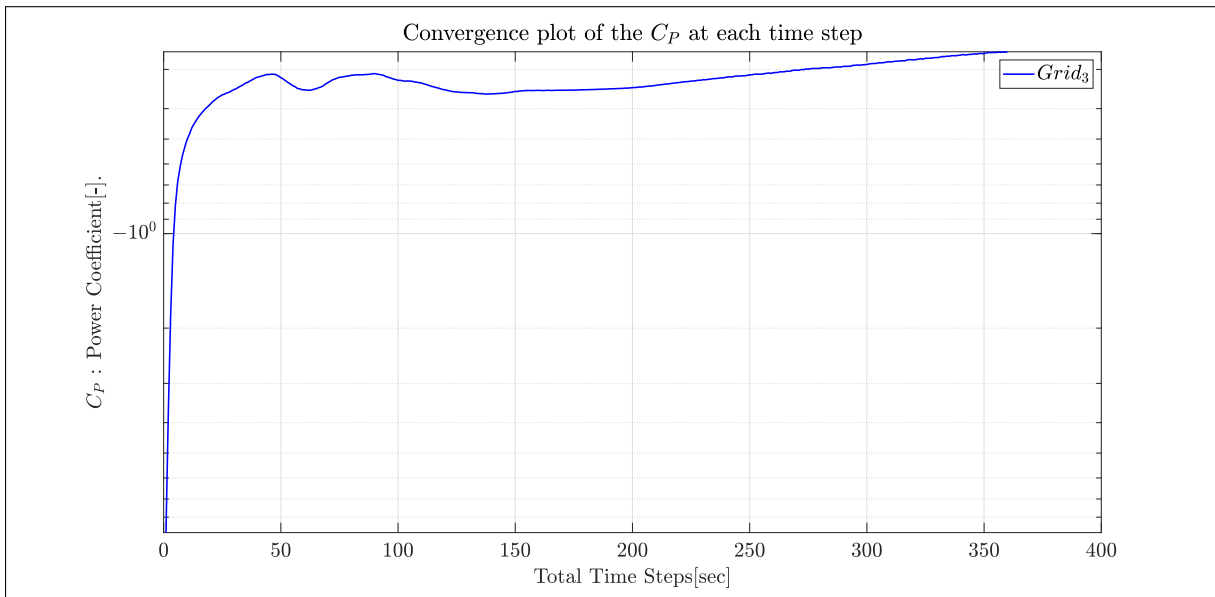
Figure 48: Iterative convergence plots of C_P for finest grid. at **each timestep**.

Table 21: Numerical uncertainty estimation for the NREL 5MW model-scale computations.

Grid no	Grid ref. $\frac{h_i}{h_1}$	C_T $[-]$	$[\%]$	U_ϕ $[-]$	C_P $[-]$	$[\%]$	U_ϕ $[-]$
1	1.09	0.512	17.57	19.7%	0.262	-0.45	48.1%
2	1.08	0.461	6.01	24.7%	0.267	1.56	48.3%
3	1.07	0.434	-0.28	19.3%	0.274	4.12	49.5%
4	**1.00**	**0.435**	**-**	**16.2%**	**0.263**	**-**	**48.15%**
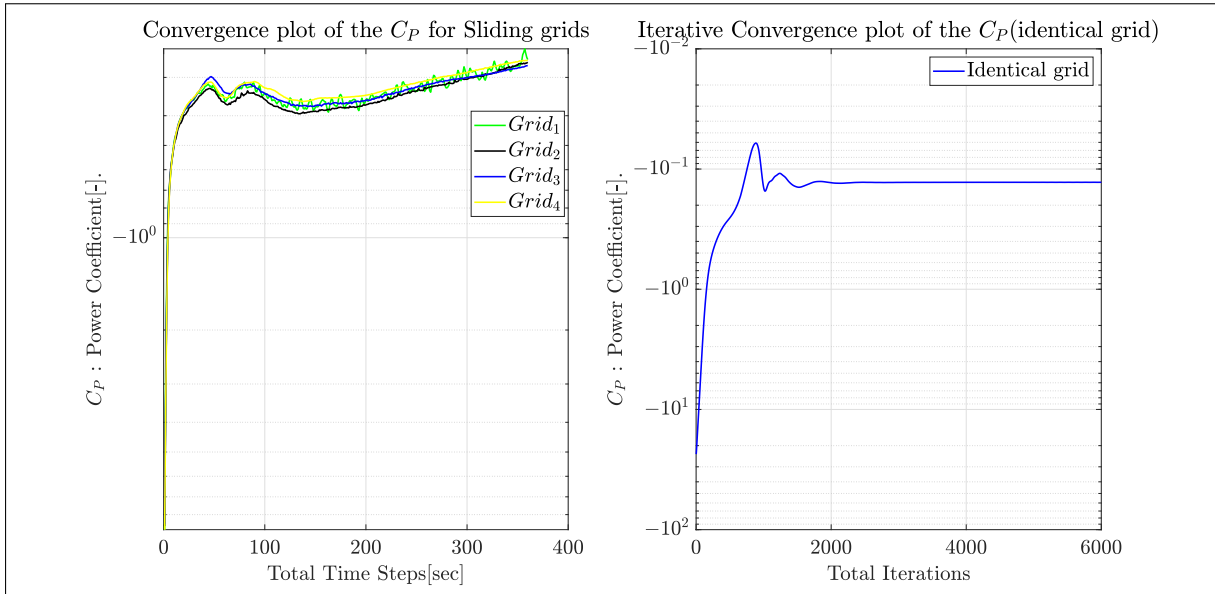
Figure 49: Comparison of iterative convergence plots of C_P for finest & Identical grid. at **each timestep**.
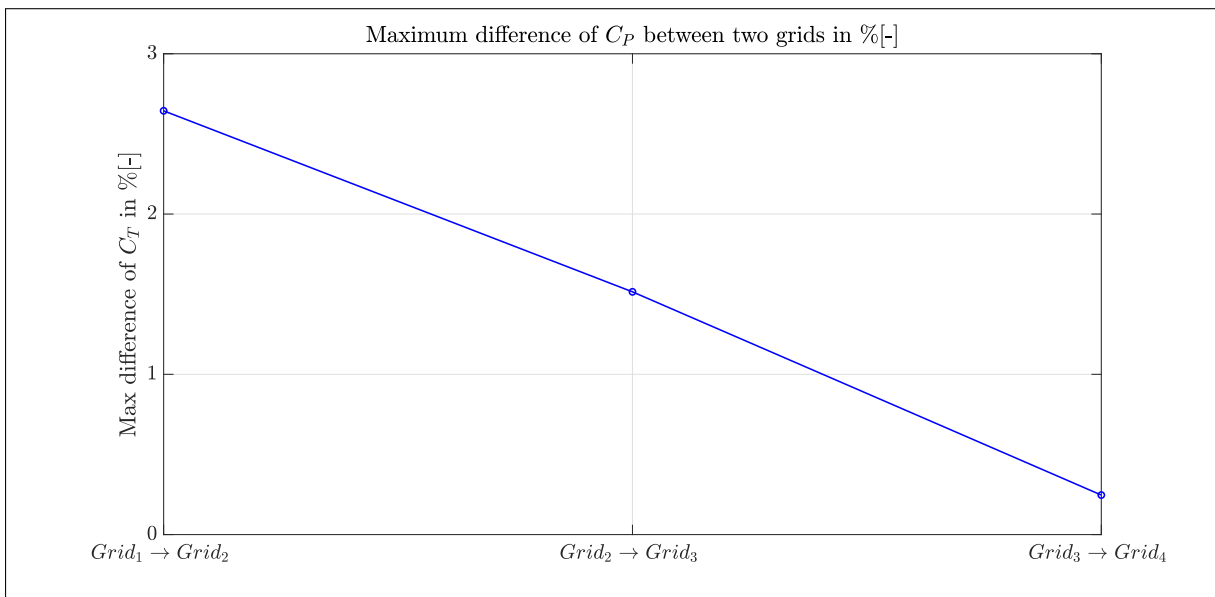
Figure 50: Maximum difference of C_P between sliding grids at **each timestep**.

sented, a large difference is observed between C_T and C_P. For C_T the estimated uncertainty of all grids is below 20 %, while for C_P the finest grid obtained an high uncertainty and in addition to table 21.

Also, in the figure 51, the C_T and CP results obtained from the computations of identical and sliding grids is plotted and from this figure, One can clearly seen that both C_T and C_P obtained for sliding grids are much higher when comparing to C_T and C_P obtained from identical grid.

When only looking at magnitude of C_T and C_P, and the difference of these quantities for various sliding grids, a decreasing trend is observed for C_T and an increasing trend observed for C_P. The differences in C_T and C_P expressed as a percentage of the solution for the finest grid show a maximum difference in C_T of less than one percent, while for C_P a maximum difference of less than 5 percent for the finest grid(for coarse grid it's 0.45 %).

The relative difference in C_T and C_P is also shown in figure 54 and the same can be depicted in figure 52 and 53 . This figure clearly shows that the values of C_P converge to a constant value, while for C_P convergence is also reached.
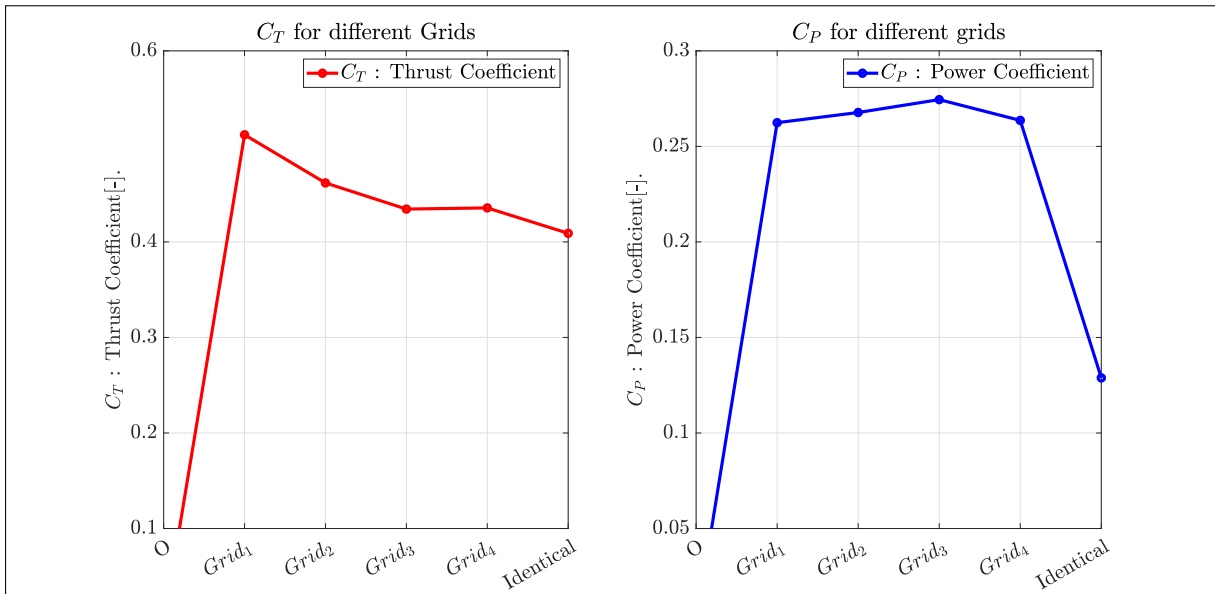
Figure 51: Thrust and Power coefficients for sliding and identical grids.

As explained before, The difference in C_T and C_P for the relative difference can be explained by the fact that C_P is much more sensitive to the change in attached flow region between the computed grids. This is due to the fact that C_P is computed by means of the moment about the rotating axis of the turbine.

The turbine rotates 3 deg for each time step which leads to value of 0.005 sec. As a result of changes in C_l/C_d at the blade tip, C_P is altered significantly due to the incorporated distance from the rotating axis. C_T on the other hand is computed by means of the axial thrust force, hence changes in C_l/C_d along the blade-span contribute equally. The even larger differences in the uncertainties between C_T and C_P are also partially caused by this phenomenon. Additionally the complex highly separated flow, the use of unstructured
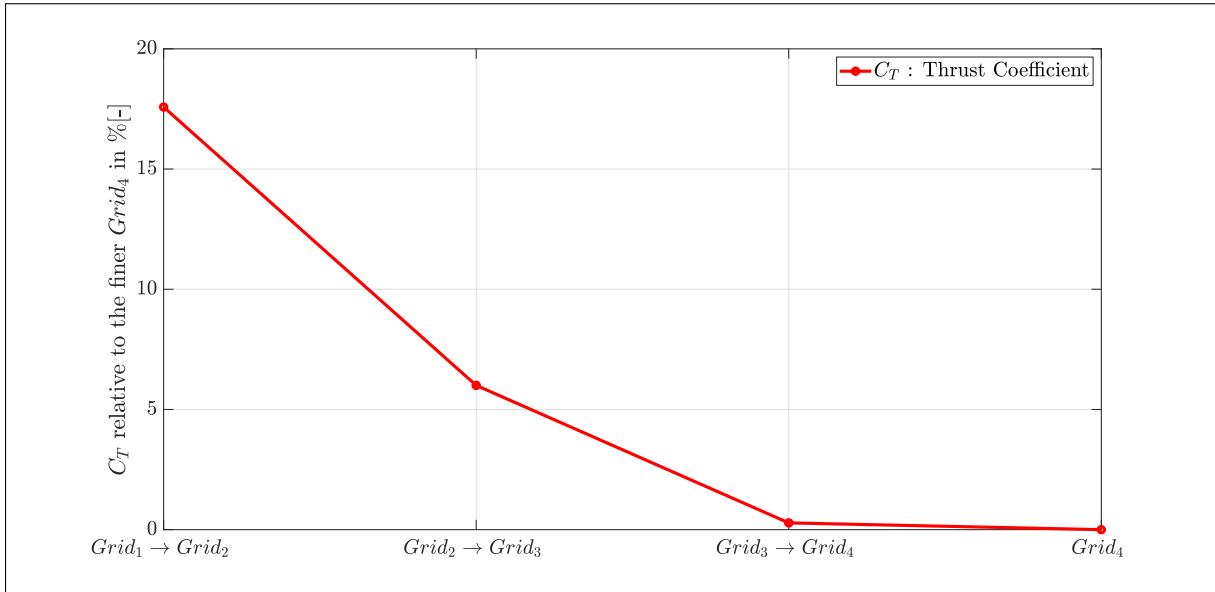
Figure 52: Thrust coefficients for sliding grids.

Figure 53: Power coefficients for sliding grids.

grids, unsteady computations and, to some extend, the iterative error cam also leads to this huge differences.

From the previous and current studies it follows that obtaining a sufficiently iteratively converged solution is challenging when doing steady and unsteady calculations. But, It can be clearly seen that the convergence has improved from steady to unsteady computations. This, in combination with the use of unstructured grids, result in large uncertainties especially for the power coefficient C_P.
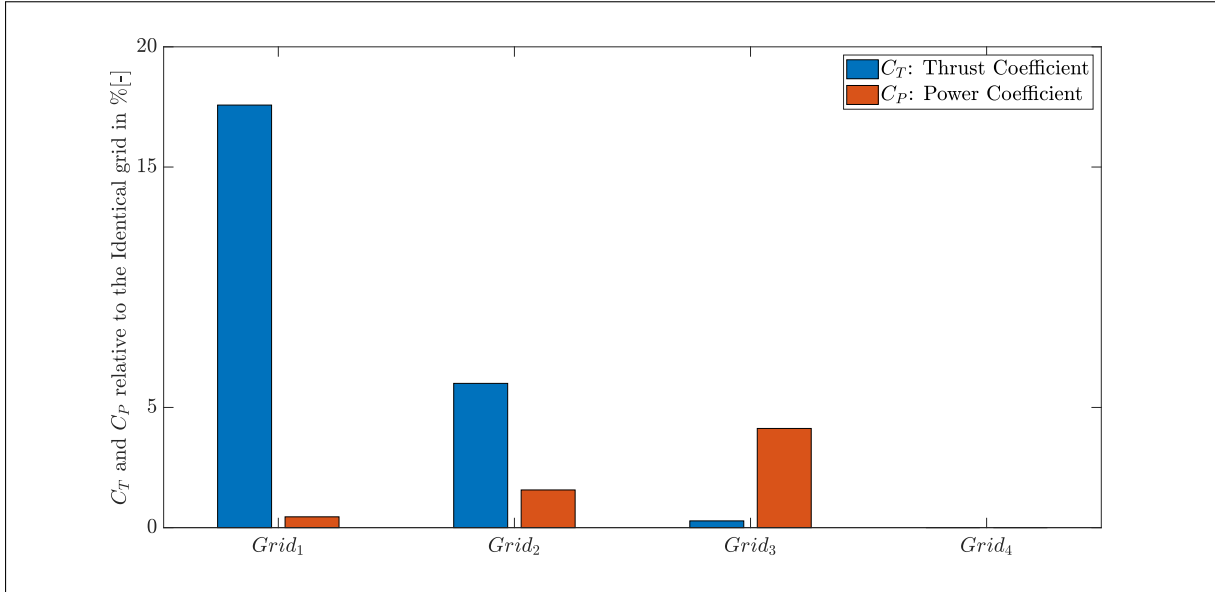
Figure 54: Power and thrust coefficient as percentage of the finest grid solution for sliding grids.

When looking at the differences in C_T and C_P between the grids and the estimated uncertainties, the finest grid(Grid no. 4)is chosen for the remainder of the computations. For this grid an uncertainty of 16.2 and 1.397.23 percent is found for C_T and C_P. While the difference between C_T and C_P for the two finest grids are 0.28 and 4.12 percent respectively. It must be kept in mind however that the iterative error may have an effect on the uncertainty estimation and the obtained solution.

8.3   Numerical convergence test

Due to the imposed rotation motion of the grid, we already know that these simulations are unsteady. For all the simulations performed in this chapter, we use a time step that is equal to an angular displacement of 3^0, i.e., $\delta t = n^{-1}/120$. To reach convergence, we need at least three full revolutions. i.e. $360\delta t$.

But, the computations are unsteady, and sensitivity analysis is essential to fix the time step for further research. So, the angular displacement of 3^0, 4^0, and 5^0 are considered and analyzed. The obtained results are shown in the table 22

The iterative convergence plots of C_T and C_P are plotted in the figure 55 and 57. From the figure 55, the convergence solution is achieved at an angular displacement of 3^0 for C_T and C_P, whereas for angular displacement at 4^0 and 5^0 degrees didn't do well. Also,

one could see fluctuations.

When we look at the magnitude and compare with previous studies, C_T and C_P at $\omega dt = 3^0$ is almost converged with the earlier studies, whereas at $\omega dt = 4^0$ and 5^0 didn't converge to the required value. A decreasing trend is seen in C_T values and an increasing trend for C_P.

Also, The relative difference in C_T and C_P is shown in table 22, and it is found to be very high. It is clear evidence that the time step plays a vital role in numerical convergence.

Table 22: Power and thrust coefficients at different angular displacement

Angular displacement	C_T	[%]	C_P	[%]
$\omega dt = 3^0$	0.4356	53.2	0.2636	75.8
$\omega dt = 4^0$	0.3296	15.9	0.3911	75.4
$\omega dt = 5^0$	0.2843	-	0.4901	-
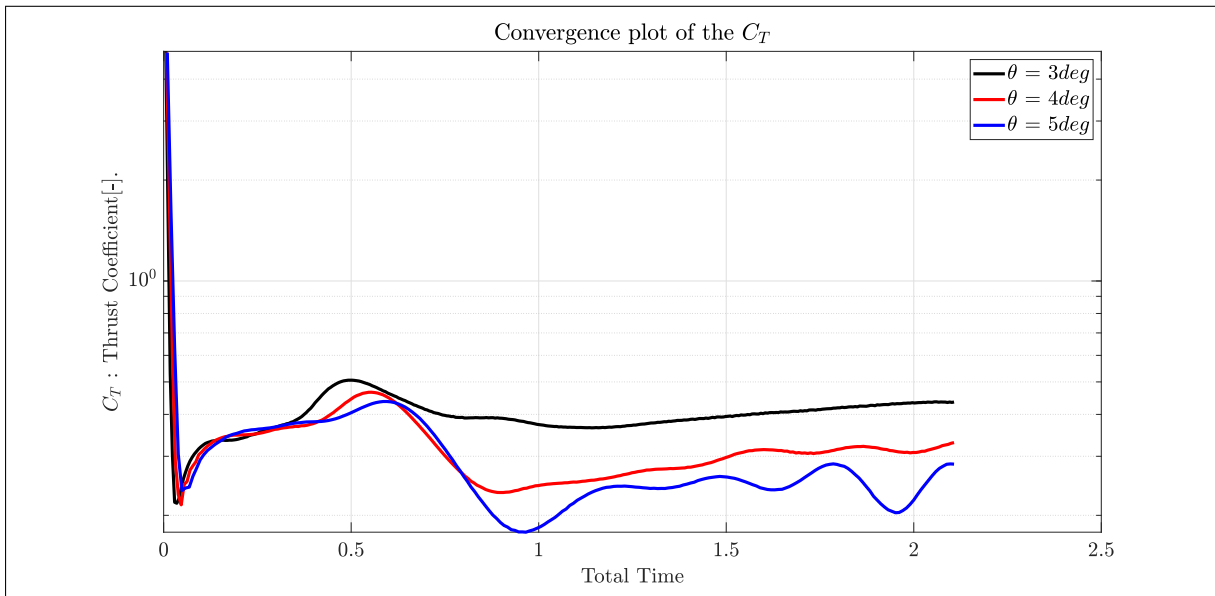
Figure 55: Iterative convergence plot of C_T at $\omega dt = 3^0$, 4^0, and 5^0.

The magnitude changes at each time steps for the quantities quantities C_T and C_P of the last 100 time steps, the maximum fluctuation of C_T is ranging from 8 % to 30 % for $\omega dt = 3^0$, 4^0, and 5^0 and this can be depicted in figure 56. A the same time, the maximum fluctuation of C_P is ranging from 0.2 % to 0.6 % for $\omega dt = 3^0$, 4^0, and 5^0 and this can be depicted in figure 58.

The result indicates that $\omega dt = 3^0$, 4^0, and 5^0 per time-step are small enough to yield
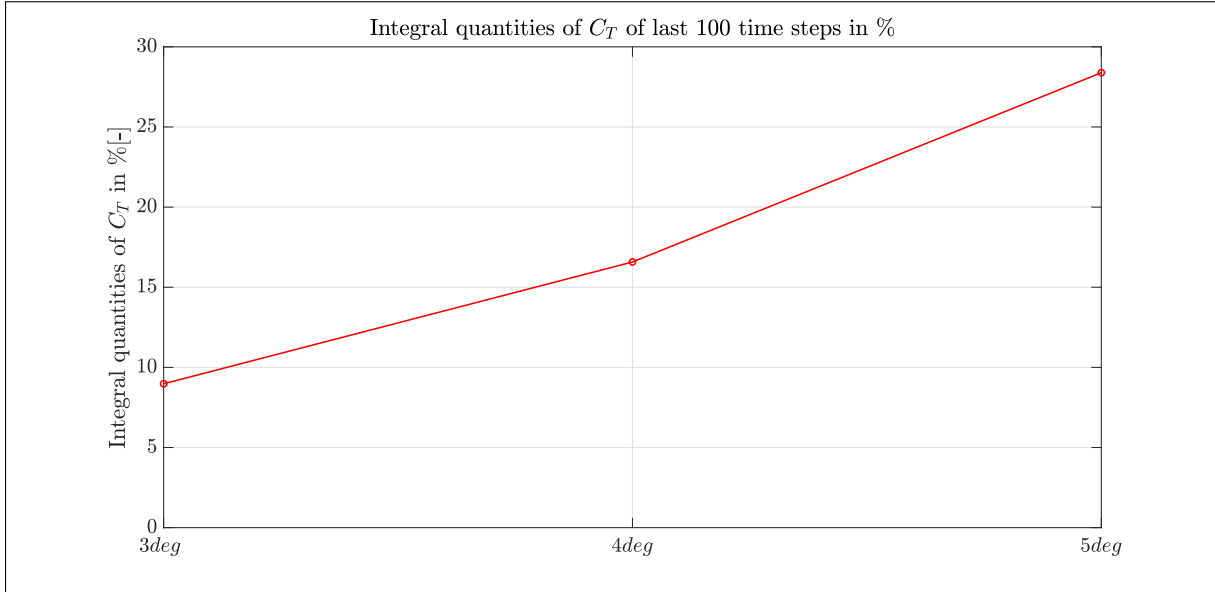
Figure 56: Integral quantities of C_T of last 100 time steps in % at $\omega dt = 3^0$, 4^0, and 5^0.
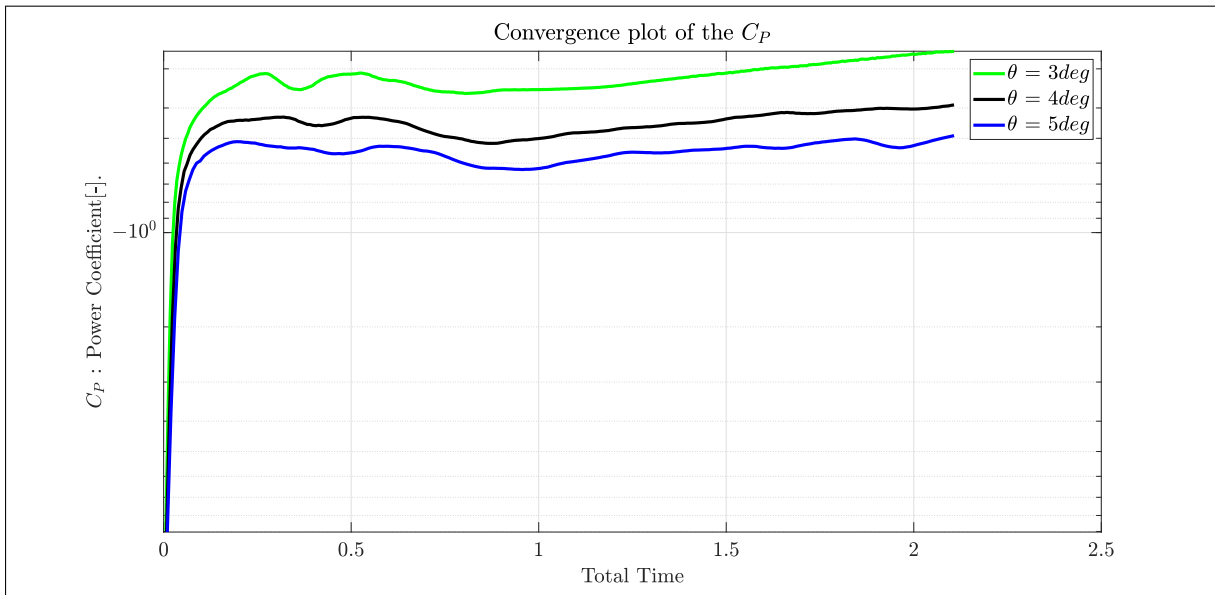
Figure 57: Iterative convergence plot of C_P at $\omega dt = 3^0$, 4^0, and 5^0.

convergent solutions. In the present study, a time-step size corresponding to 3^0 increment of the azimuth angle of the blade per time-step was applied in all the simulations.

The selected time-step size should be small enough to account entirely for the turbine blade-tip-wake interaction. Since the translational(surge, sway and heave degrees of freedom) and rotational(roll, pitch, and yaw degrees of freedom) motion of the FOWT will be investigated for a specific range of angular frequencies and displacement amplitudes in the future.
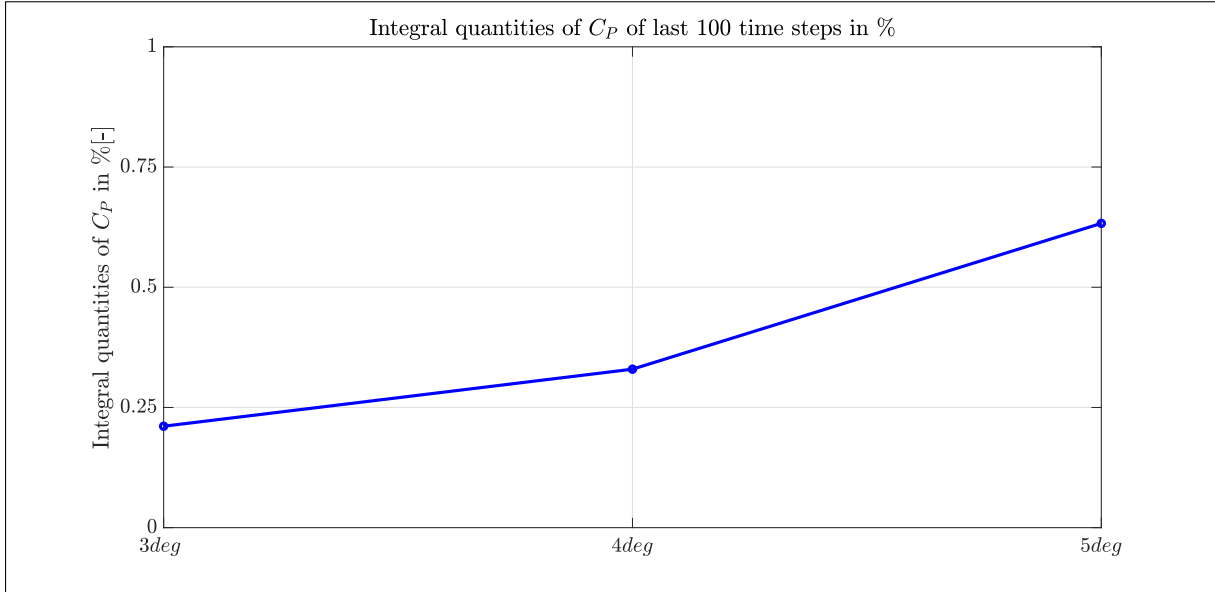
Figure 58: Integral quantities of C_P of last 100 time steps in % at $\omega dt = 3^0$, 4^0, and 5^0.

8.4   Results and Discussion

The C_T and C_P curves of the model-scale URANS computations of sliding grid and identical grid along with results obtained from previous studies are presented in figures 59 and 60.

The differences in percentage are presented in figure 59 show a good agreement between least-squares approach($U_{\phi_{LS}}$) and the relative difference($U_{\phi_{rel}}$) of the finest grids for both sliding and identical grid for C_T at higher TSRs and larger differences are found in the higher TSR range for C_P.

The reasons for these differences are already explained in the previous studies. In the steady computations, one can notice that the results of C_T and C_P at a wider range of TSRs keep on increasing, whereas for the unsteady computations, the increasing trend is not that high, and it can be depicted in the figure 59

Also, previous studies(least-squares approach, relative difference approach for three finest grids) and the current study(identical grid) showed an agreement at a wider range of TSRs for C_T. The power coefficient is highly sensitive and could be seen from the figure 60 resulting in higher difference for both absolute formulation approach and sliding grid methodology.

Moreover, the flow case for this study has wind speed of $V_{inflow} = 1.61 \ m/s$ and TSR =

7 for all the simulations. Here, the V_{inflow} may be increased to 2.47 m/s or 2.94 m/s. So, that the flow would be stable and can achieve better converged solution.

The percentage difference of C_T and C_P between two different approaches for a wide range of TSRs can be seen in the fourth column of tables 23 and 24.

Table 23: Results of C_T at different TSRs obtained by ReFRESCO & Percentage difference of w.r.t Relative Difference based

TSR	Identical grid	Least-Scale Approach	Relative Difference	[%]
3	0.128	0.319	0.0.186	41.8
4	0.173	0.363	0.248	31.78
5	0.234	0.399	0.310	22.24
6	0.327	0.422	0.372	11.85
7	**0.435**	**0.410**	**0.434**	**0.28**
8	0.481	0.440	0.496	-12.6

Table 24: Results of C_P at different TSRs obtained by ReFRESCO & Percentage difference of w.r.t Relative Difference based

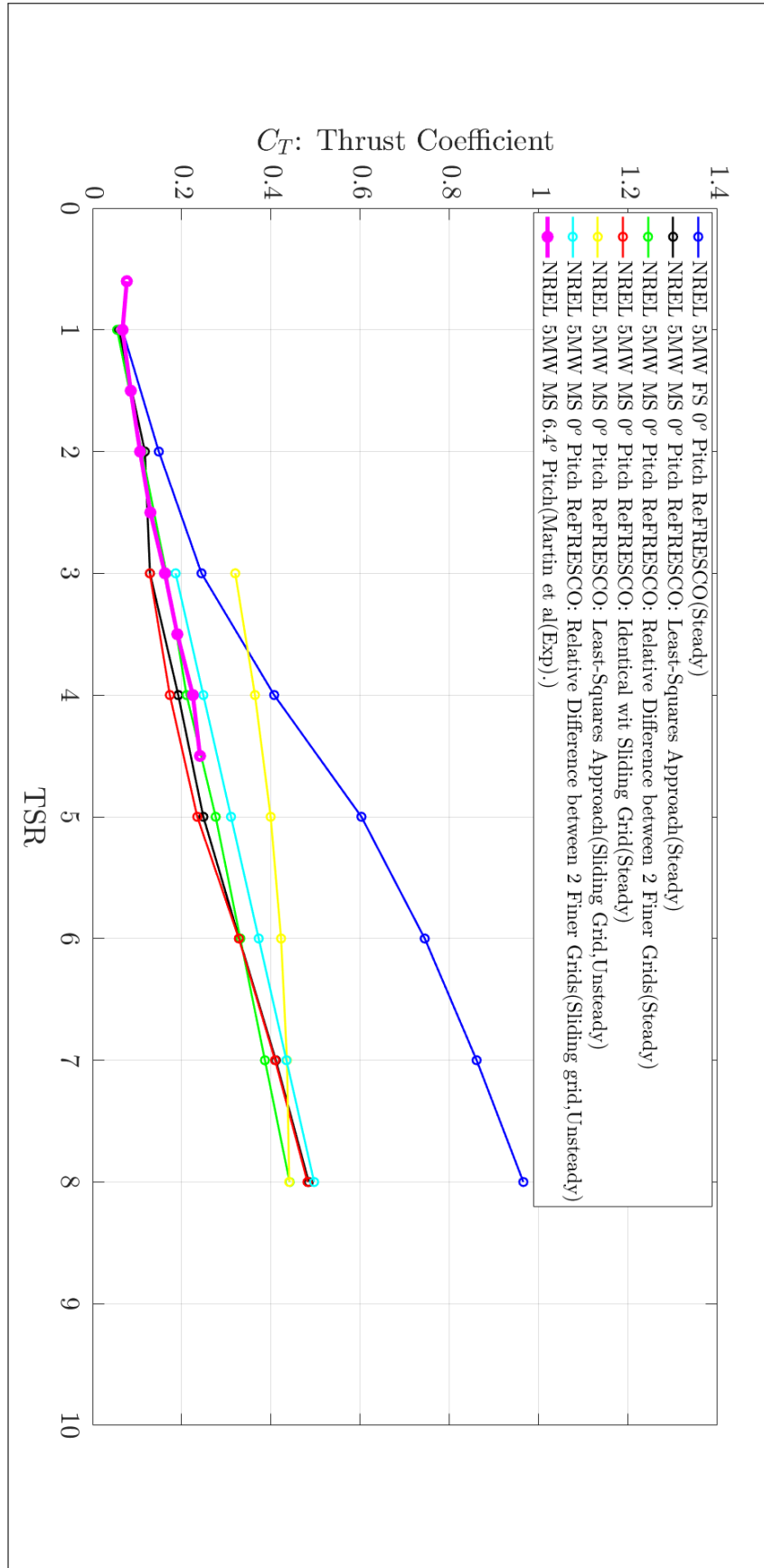| TSR	Identical grid	Least-Scale Approach	Relative Difference	[%]
3	0.035	0.054	0.117	114.8
4	0.063	0.020	0.156	86.7
5	0.087	0.041	0.196	78.9
6	0.088	0.136	0.235	42.16
7	**0.128**	**0.263**	**0.274**	**3.96**
8	0.198	0.425	0.313	-35.7

Figure 59: C_T curves of model-scale NREL including uncertainties
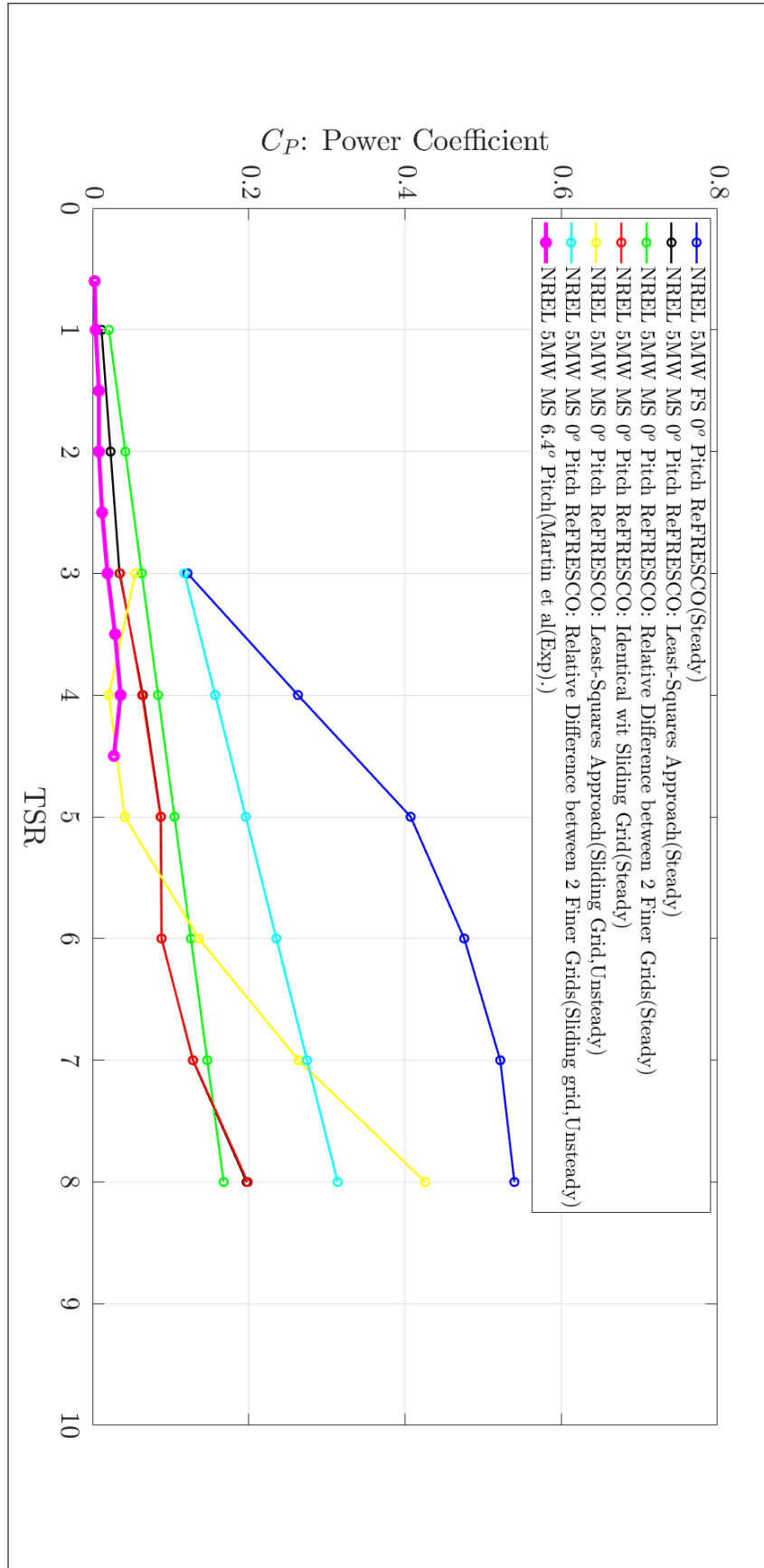
Figure 60: C_P curves of model-scale NREL including uncertainties

9 Conclusions

The final conclusions of the present work are discussed in this section.

9.1 Numerical Analysis using Absolute Formulation Approach

- The impact of a three-dimensional grid is investigated using three domains of varied sizes to examine the flow over the turbine. For the most significant domain of 30 times the turbine diameter, the impact of the boundary conditions is negligible. Also, the relative differences of less than 1%. To further understand the effect of domain size, more computations for lower tip speed ratios have been performed, and it is recommended to use Domain C for further calculations.

- Due to the turbulent character of the flow under model-scale settings, iterative convergence using steady calculations is difficult. But an updating in the flow would be required for further analysis. In the wake-field of the blade root, typical L_{infty} and L_2- norms of residuals in the order of may be detected. The integral values C_T and C_P, on the other hand, converge to a constant value. There is a lot of uncertainty because of the scale of the iterative error and the usage of unstructured grids. Using finer grids resulted in 9.7% and 28.6% uncertainty for C_T and C_P, respectively. For C_T and C_P, the relative difference between the two most refined grids is just 0.31 and 3.39 percent, respectively. Compared to stable RANS calculations, it is preferable to execute many URANS computations due to the modest iterative convergence and highly separated flow. As reported in this research, the uncertainty assessment strategy is based on the least-squares method and the most common approach based on the relative difference between any two grids.

- A sensitivity study is performed between k - ω SST (2003), Spalart-Allmaras model and k - $\sqrt{K}L$ Scale-Adaptive-Simulation Model (SAS). Most of the differences are found in the magnitude of C_P, and those differences can be seen in Normalized turbulence viscosity and velocity fields. It is found that the k - ω SST (2003) model had performed better than the other two models because the latter models over predict C_T and C_P.

- The error associated with numerical computations is estimated using the least-squares approach(LS). The relative difference(RD) between the two most refined

grids for both C_T and C_P and compared between them.

9.2   Numerical Analysis using Sliding Grid Methodology

- The same methodology explained in 9.1 is used for the sliding grid technique. The final domain used in section 7 will be adopted here but containing sliding interfaces. Since, there is no experimental data available, an identical grid is generated for comparison.

- The Iterative convergence utilising unsteady flow computations at model-scale conditions has been achieved. An typical level of L_{infty}- and L_2- norms of residuals are at the level of 10^3 and 10^2, respectively. The magnitude changes in C_T and C_P at each time step size, on the other hand, converge to a near-constant value. The refined grids has an error of result in 16.2 and 48.15 percent for C_T and C_P, respectively. For C_T and C_P, the relative difference between the two finest grids is just 0.28 and 4.12 percent, respectively. As shown in this work, an uncertainty estimate strategy based on the least squares method in conjunction with a more typical approach based on relative difference was used.

- As these computations are said to be unsteady. So, the solution can be influenced by time step. A numerical convergence study is performed at $\omega dt = 3^0$, 4^0 and 5^0. The iterative convergence plots of C_T and C_P are checked at $\omega dt = 3^0$, 4^0 and 5^0 and it is found that the convergence solution is clearly achieved only for $\omega dt = 3^0$, whereas for angular displacement at 4^0 and 5^0 didn't do well. Also, once could see fluctuations which leads to very large differences in C_T and C_P. The integral quantities C_T and C_P of the last 100 time steps, maxmium fluctuation of C_T is found to be 8%, whereas for C_P is found to be 0.2%. So, an time step of $\omega dt = 3^0$ will be used for the rest of the simulations.

- The error associated with numerical computations is estimated using the least-squares approach(LS). The relative difference(RD) between the two most refined grids for both C_T and C_P and compared between them.

- Finally, it is understand that Sliding grids performance is much better.

References

[1]   IREA IRENA. "Future of wind: Deployment, investment, technology, grid integration and socio-economic aspects". In: (2019).

[2]   Michel Make and Guilherme Vaz. "Analyzing scaling effects on offshore wind turbines using CFD". In: *Renewable Energy* 83 (2015), pp. 1326–1340.

[3]   Bjørn Skaare et al. "Analysis of measurements and simulations from the Hywind Demo floating wind turbine". In: *Wind Energy* 18.6 (2015), pp. 1105–1122.

[4]   Tomoaki Utsunomiya et al. "Floating offshore wind turbine demonstration project at Goto Islands, Japan". In: *OCEANS 2014-TAIPEI*. IEEE. 2014, pp. 1–7.

[5]   Christopher Allen et al. *Definition of the UMaine VolturnUS-S Reference Platform Developed for the IEA Wind 15-Megawatt Offshore Reference Wind Turbine*. Tech. rep. National Renewable Energy Lab.(NREL), Golden, CO (United States), 2020.

[6]   Amy Robertson et al. "Offshore code comparison collaboration continuation within IEA wind task 30: Phase II results regarding a floating semisubmersible wind system". In: *International Conference on Offshore Mechanics and Arctic Engineering*. Vol. 45547. American Society of Mechanical Engineers. 2014, V09BT09A012.

[7]   Jason M Jonkman, Marshall L Buhl Jr, et al. "FAST user's guide". In: *Golden, CO: National Renewable Energy Laboratory* 365 (2005), p. 366.

[8]   Simon Burmester, Guilherme Vaz, and Ould el Moctar. "Towards credible CFD simulations for floating offshore wind turbines". In: *Ocean Engineering* 209 (2020), p. 107237.

[9]   Jason Jonkman et al. *Definition of a 5-MW reference wind turbine for offshore system development*. Tech. rep. National Renewable Energy Lab.(NREL), Golden, CO (United States), 2009.

[10] Erik-Jan de Ridder et al. "Development of a scaled-down floating wind turbine for offshore basin testing". In: *ASME 2014 33rd International Conference on Ocean, Offshore and Arctic Engineering*. American Society of Mechanical Engineers Digital Collection. 2014.

[11] Heather Rae Martin. "Development of a scale model wind turbine for testing of offshore floating wind turbine systems". In: (2011).

[12] Heather R Martin et al. "Methodology for wind/wave basin testing of floating offshore wind turbines". In: *Journal of Offshore Mechanics and Arctic Engineering* 136.2 (2014).

[13] Subrata Chakrabarti. "Physical model testing of floating offshore structures". In: *Dynamic positioning conference*. Vol. 1. Citeseer. 1998, pp. 1–33.

[14] John David Anderson Jr. *Fundamentals of aerodynamics*. Tata McGraw-Hill Education, 2010.

[15] Frank M White. "Fluid mechanics". In: (1986).

[16] RS Cant. "Sb pope, turbulent flows, cambridge university press, cambridge, uk". In: *Combustion and Flame* 125 (2001), pp. 1361–1362.

[17] Franciscus Theodorus Marie Nieuwstadt. *Turbulentie: inleiding in de theorie en toepassingen van turbulente stromingen*. Epsilon Uitgaven, 1998.

[18] David C Wilcox et al. *Turbulence modeling for CFD*. Vol. 2. DCW industries La Canada, CA, 1998.

[19] "N. International, "HEXPRESS Unstructured Full-Hexahedral Meshing."" In: ().

[20] "NUMECA Inernational, Numeca International, Brussels, User Manual Hexpress". In: (2012).

[21] Guilherme Vaz, Frederick Jaouen, and Martin Hoekstra. "Free-surface viscous flow computations: validation of URANS code FRESCO". In: *International Conference on Offshore Mechanics and Arctic Engineering*. Vol. 43451. 2009, pp. 425–437.

[22] James Ahrens, Berk Geveci, and Charles Law. "Paraview: An end-user tool for large data visualization". In: *The visualization handbook* 717.8 (2005).

[23] KATHY E MITCHELL. "Tecplot 8.0". In: *Science* 290.5499 (2000), pp. 2097–2097.

[24] G. Vaz and D. Rijpkema. "Non-Conformal and Sliding Interfaces in ReFRESCO," in: *MARIN Report 70015-13-RD* (January 2013).

[25] William Otto, Douwe Rijpkema, and Guilherme Vaz. "Viscous-flow calculations on an axial marine current turbine". In: *International Conference on Offshore Mechanics and Arctic Engineering*. Vol. 44946. American Society of Mechanical Engineers. 2012, pp. 369–382.

[26]   L Eça, GNVB Vaz, and M Hoekstra. "A verification and validation exercise for the flow over a backward facing step". In: *Fifth European Conference on Computational Fluid Dynamics*. 2010, pp. 14–17.

[27]   Lui's Ec a, Guilherme Vaz, and Martin Hoekstra. "Code verification, solution verification and validation in RANS solvers". In: *International Conference on Offshore Mechanics and Arctic Engineering*. Vol. 49149. 2010, pp. 597–605.